DISSERTATION

PLASMA CHEMICAL DRIVEN BIOMEDICAL APPLICATIONS WITH A RADIO FREQUENCY DRIVEN ATMOSPHERIC PRESSURE PLASMA JET

Submitted by

Myeong Yeol Choi

Department of Electrical and Computer Engineering

In partial fulfillment of the requirements

For the Degree of Doctor of Philosophy

Colorado State University

Fort Collins, Colorado

Fall 2012

Doctoral Committee:

Advisor: George J. Collins

Dean A. Hendrickson
Branislav Notaros
Masahiro Watanabe

ABSTRACT

PLASMA CHEMICAL DRIVEN BIOMEDICAL APPLICATIONS WITH A RADIO FREQUENCY DRIVEN ATMOSPHERIC PRESSURE PLASMA JET

We present radio frequency driven atmospheric pressure plasma jet for various biomedical applications such as tissue removal, bacterial sterilization, and tooth whitening. Two different types of plasma assisted electrosurgery, remote electrode plasma jet and plasma jet surrounding monopolar electrosurgical electrode, were employed to enhance tissue removal in terms of less heat damage on contiguous tissue and fast removal rate. Chlorine based chemical (CH_XCl_X) additives in argon plasma jet enhanced tissue removal rate, proportional to the Cl radical density in the plasma jet. Pulsed RF provided another knob to control the removal profile, heat damage, and removal rate. Hydrogen peroxide (H_2O_2) additive provided abundant OH generation in the helium plasma jet. It not only enhanced tissue removal rate but also reduced heat damage on the contiguous tissue. The tissue removal mechanism of helium-H_2O_2 plasma is explained based on the FTIR measurement of the tissue samples, and optical emission and absorption spectra. Hydrogen peroxide addition to argon plasma jet was employed for bacterial inactivation. Observed OH density by optical emission and absorption was proportional to the number of deactivated microorganism. Argon plasma jet in DI water also provided abundant OH on the interface of water and gas plasma. The OH radicals applied on porcine tooth sample selectively removed the stain without damaging the underlying enamel.

ACKNOWLEDGEMENTS

I would like to thank all who supported and helped me to study toward Ph.D. degree. I appreciate so much my advisor, Prof. George J. Collins, for his teaching classes and his guidance to many opportunities to learn and explore the challenging plasma biomedical application research. I also appreciate Dr. Il Gyo Koo not only for his advices and guidance on research projects but also his kind help to my life.

I would like to express my gratitude to Dr. Dean A. Hendrickson, Dr. Branislav M. Notaros, and Dr. Masahiro Watanabe who served as committee members for my degree. I really want to thank all my colleagues of Post-doctors of Dr. Jae-Chul Jung, Prof. Paul Y. Kim, Dr. Yoonsun Kim, Dr. Jinhoon Cho, Dr. Gonjun Kim and Dr. Saburo Uchida, and exchange students from POSTECH, Myoung Soo Kim and Sung Kil Kang, assistants of Eugene, Hiroki and Victor Brouk. Dr. Denis Shaw and Dr. Masahiro Watanabe gave me a chance to have important industrial experience.

I'm so grateful to my wife Natsuki Kobayashi for her love and sacrifice for my sake. I'm thankful to her parent, Yu, my parents, my brother, and sisters for all of the support.

Chapter 2, 3, 4, 5, 6, and 7 reused papers that are published or under review to publish. The work for chapter 3, 4, and 5 were funded by Covidien Ltd. and partially supported by the National Research Foundation of Korea Grant funded by the Korean Government (D00052). The entire work of chapter 6 was supported by the Korea Science and Engineering Foundation (KOSEF) grant funded by the Korean government (MOST) (Grant No. R01-2007-000-10730-0) and the Korea Ministry of Education, Science, and Technology through its Brain Korea 21 program. Work conducted at Colorado State University was partially funded by the State of

Colorado. The work of chapter 7 was supported by Mid–career Researcher Program through NRF grant funded by the Korea MEST (2011-0015395) and Bioscience Discovery Evaluation Grant Program of the Colorado State Government (10BGF-25). The grant funded by the Korean government and Korea Ministry of Education, Science and Technology was through its Brain Korea 21 program. All authors are thankful for the contributions of Dr. Hyun Woo Lee at the Pohang University of Science and Technology who developed the simulation programs.

TABLE OF CONTENTS

LIST OF FIGURES

CHAPTER 1. INTRODUCTION TO ATMOSPHERIC PRESSURE PLASMA

Polar aurorae, lightning, the sun and stars are all examples of naturally generated plasma. One can also generate artificial plasma such as in fluorescent light by capacitive or inductive coupling of electrical energy. Non-thermal equilibrium plasma (Te >> Tg) has large number of applications such as surface treatment of heat sensitive materials due to the relatively low plasma gas temperature compared to thermal equilibrium plasma (Te ≈ Tg >> 1,000 K) and reactive chemical species. Low pressure plasma is characterized by non-thermal equilibrium. However, it requires expensive and complicated vacuum equipment, and provides low partial pressure of reactive species. Various types of electrode with small gap and noble gases enabled us to create non-thermal atmospheric pressure plasma, that do not require a vacuum. In this chapter, atmospheric pressure plasma is introduced and compared to low pressure plasma regarding their advantages and disadvantages.

1.1. Plasma Definition and Generation

Plasma is the fourth state of matter consists of electrons, positive and negative ions, molecules in ground or excited states. Plasma is electrically neutral and electrically conductive. Plasma can be generated by applying energy to gas (solid – liquid – gas – plasma). In this dissertation, electrical energy is employed to generate plasma. Electrical energy is applied to gas in the form of electromagnetic field. In general, the electrical energy to generate and sustain the plasma is capacitively or inductively coupled. Capacitively coupled plasmas (CCP) employ E field to accelerate electrons while inductively coupled plasmas (ICP) employ time varying B field that generate E field (by faraday's law). Typical capacitively and inductively coupled

plasmas are illustrated in Figure 1-1 (a) and (b). The charge acceleration forces (Lorentz force) of capacitively and inductively coupled plasmas are $\boldsymbol{F} = q \cdot \boldsymbol{E}$ and $\boldsymbol{F} = q(\boldsymbol{v} \times \boldsymbol{B})$, respectively.

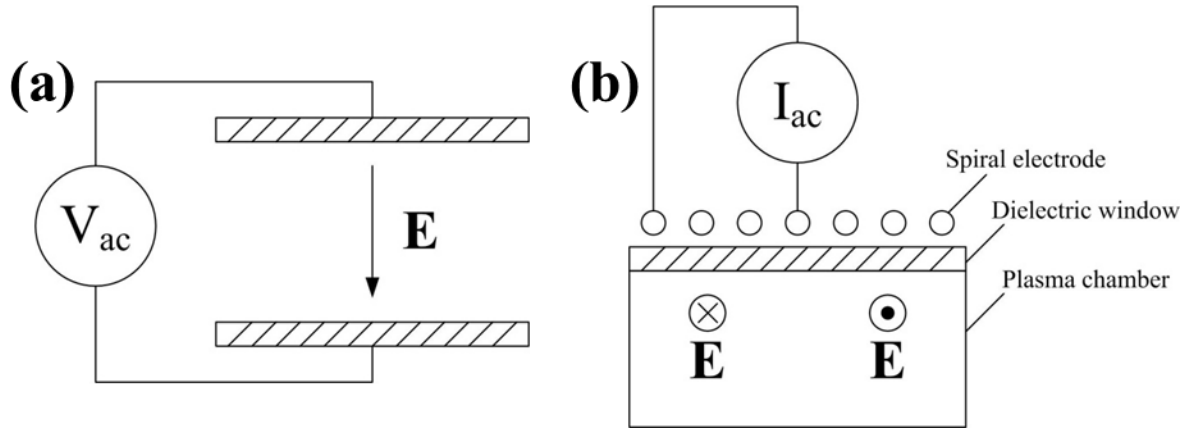

Figure 1-1 Typical illustration of (a) capacitively coupled plasma and (b) inductively coupled plasma

Plasma is ignited through the transition process from insulating neutral gas to conducting ionized gas. This process is known as plasma breakdown. In 1909, Townsend proposed a theory that could explain the breakdown phenomena including electron avalanches and secondary electron emission by ion collision to cathode. When E field is applied, seed electrons, the most mobile charged species, gain energy and drift. The electrons collide with neutral gas molecules and ionize them by generating positive and negative ions, and electrons. This results in multiplication of the charged particles. The charged particles are exponentially increased by the chain reaction of the multiplication. This process is called electron avalanche. Photograph of the electron avalanche has been taken by Raether as shown in Figure 1-2.[1] Particles with the more energy than electrode material's work function, the minimum energy required to removing an electron from a metal or solid material, can release electrons by colliding on the electrode surface. This process is called secondary emission. It can be caused by positive ions, excited atoms,

electrons and photons. Ion-impact electron emission is the dominant secondary emission mechanism.[2]

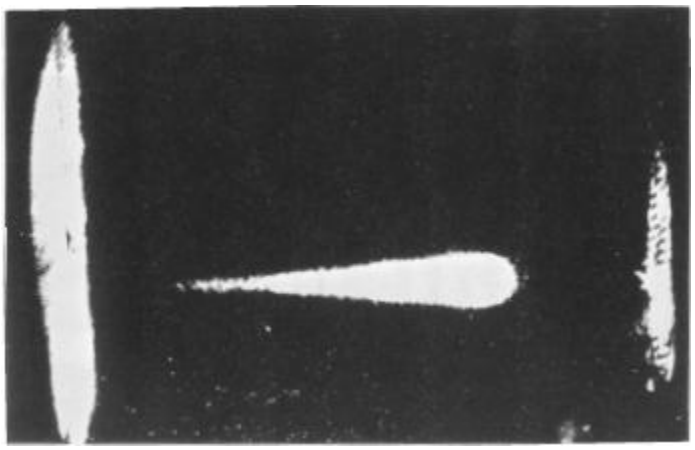

Figure 1-2 Cloud track photograph visualizing an electron avalanche. The cathode is located on the left, the anode on the right.[1]

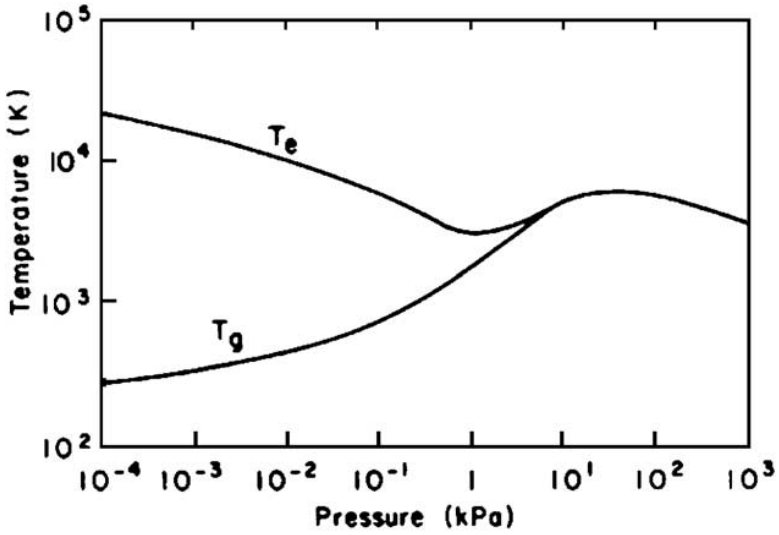

Figure 1-3 Evolution of the plasma temperature (electrons and heavy particles) with the pressure in a mercury plasma arc.[3]

1.2. Low Pressure Plasma

In low pressure plasmas, electrons are accelerated enough by external electromagnetic field due to long mean free path. The inelastic collisions between electrons and heavy particles excite or ionize the heavy particles. Therefore, electron temperature is much higher than plasma gas temperature (Te >> Tg). This type of plasma is called non-thermal equilibrium plasma. Low pressure plasmas are in non-thermal equilibrium (Te >> Tg) as shown in Figure 1-3.

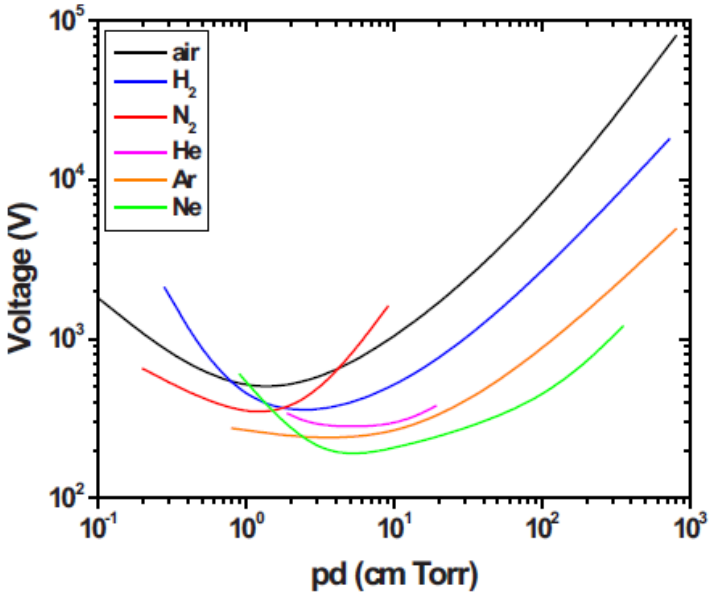

Figure 1-4 Color online Breakdown voltage of parallel plates in a gas as a function of pressure and gap distance for various gases.[4]

Non-thermal equilibrium plasma has low plasma gas temperature but energetic electrons to create reactive species instead of heating the entire gas stream. These characteristics provide the possibility to use non-thermal plasma for low temperature plasma chemistry such as treatment of heat sensitive materials. However, low pressure plasma equipment requires air tight enclosures such as massive vacuum reactors. Air tight equipment of reactors, gas lines, MFCs, vacuum pumps are very expensive and complicated. In addition, the operation is time consuming. In addition, it has low partial pressure of reactive species due to the limit of the low total pressure.

Therefore low pressure plasma is not suitable for fast plasma chemical reaction with large device but suitable for nano-structure treatment such as thin film etching. To avoid the drawback associated with vacuum (1-100 mTorr) and low partial pressure of reactive species, many researchers and scientists have developed atmospheric pressure plasmas (750 Torr).

1.3. Atmospheric Pressure Plasmas

Atmospheric pressure plasma has disadvantages of relatively high breakdown voltage compared to low pressure plasma as shown in the Paschen curve (Figure 1-4). High pressure like atmosphere has short mean free path ($\lambda_i = 1/(n_g \cdot \sigma_i)$) for electron motion, the average distance travelled between successive collisions that particles lose energies when in motion. To generate plasma, electrons and charged particles in high pressure require high electric field to accelerate them by Lorentz force compared to low pressure environment. Electric field can be increased by increasing voltage or decreasing gap ($E = -\Delta V/\Delta d$) between electrodes. Increasing voltage is not desired and easy due to the cost and hazard, atmospheric pressure plasmas normally have small gap between electrodes. In addition to the small gap, noble gases are often employed as carrier gas to reduce the breakdown voltage as seen in Figure 1-4. Helium and argon are the most frequently used noble gases due to the cost and abundance compared to Neon, Krypton, and Xenon. The breakdown voltage is expressed as the equation below.

$$V_b = \frac{B(p \cdot d)}{ln\left[\left(A(p \cdot d)\right)\right] - ln\left[ln\left(1 + \frac{1}{\gamma_{se}}\right)\right]}$$

Breakdown voltage, Vb, is a function of pressure (p), gap between electrodes (d), A and B (gas-specific constants derived from experiment), and secondary emission coefficient, γse (the number of secondary electrons created per incident ion, gas and substrate specific).[5]

Once plasma is ignited, atmospheric pressure plasma tends to be at thermal equilibrium as we have seen in Figure 1-3. Many researchers and scientists have found various types of non-thermal plasma, for example, corona discharge, dielectric barrier discharge (DBD) and atmospheric pressure plasma jet (APPJ). These non-thermal plasmas have low plasma gas temperature as well as high partial pressure of reactive chemical species. Therefore they have found large number of applications of fast plasma chemical reaction (fast processing) with simple and cost effective equipment. Those non-thermal plasma types and their applications are detailed in the following paragraphs to set the stage for our own work on non-thermal atmospheric plasma jets.

1.3.1. Corona

Corona discharge is the characterized by an asymmetric electrode pair and inhomogeneous electric field. The high electric field near the point electrode exceeds the breakdown strength of the gas and creates plasma near the sharp point. Then the plasma spreads out toward the planar electrode. Figure 1-5 shows a schematic of a typical corona discharge.

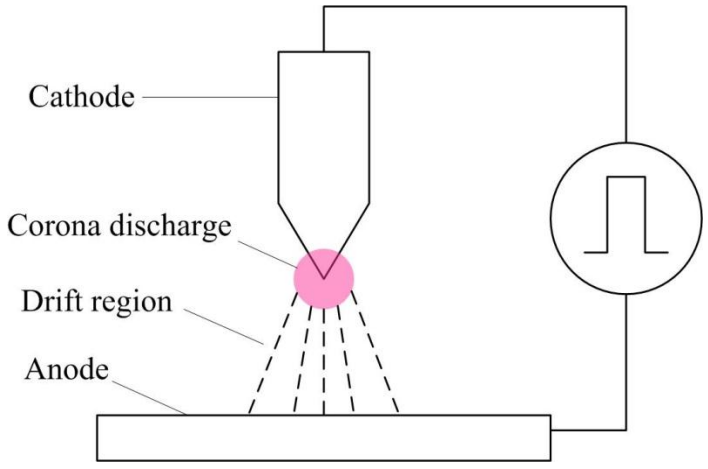

Figure 1-5 Schematic of a typical corona discharge (pin to plate).

It is a positive corona when the sharp point electrode is connected to the positive output of the power and negative corona with the negative output polarity. The application fields of the corona discharge are dust collection, water purification, electrophotography, copying machine, printers, and powder coating. [6]

1.3.2. Dielectric Barrier Discharge

Dielectric barrier discharge (DBD) is non-thermal equilibrium plasma with moderate gas temperature at atmospheric pressure. At least one of the electrodes is covered with a dielectric layer. Alternating voltages are applied on the electrodes to accumulate charge on the dielectric required to drive plasma. DBD is often composed of many filament-like microdischarges that are randomly distributed over the electrode surface.[7,8] DBD have a large number of applications such as ozone production for water purification, generation of excimer radiation in the UV/VUV spectral regions, thin film deposition processes, plasma display panel due to due to the non-thermal equilibrium plasma and large dimensions.[9-14]

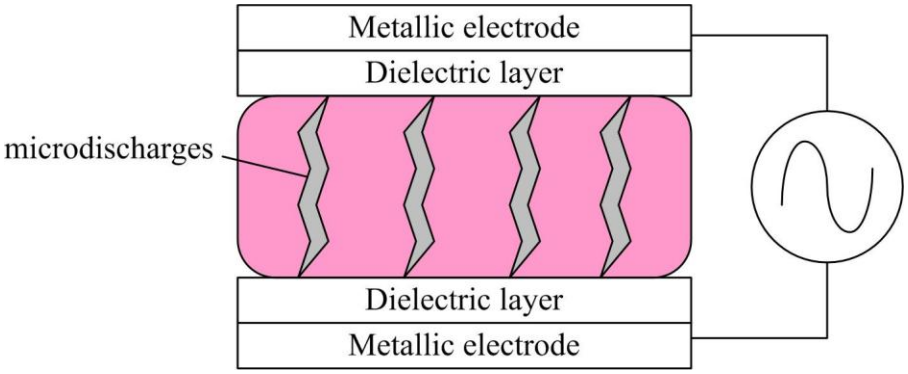

Figure 1-6 Schematic of a typical dielectric barrier discharge.

1.3.3. Atmospheric Pressure Plasma Jet Research Prior to CSU studies

Atmospheric pressure plasma jet (APPJ) has a variety of electrode types. One example of the APPJs is shown in figure 1-7. The inner electrode is coupled to radio frequency power and the outer electrode is grounded. By applying RF power, the discharge is ignited between the electrodes. Plasma jet with highly reactive chemical species is blown out of the nozzle. The energetic electrons generated in the discharge region produce charged ions, excited state molecules, and radicals. In the effluent region, ions and electrons are rapidly lost by recombination. However, the metastable species and neutral radicals are still remained in the jet. In addition, the plasma gas temperature can be cooled by cooling the outer ground electrode. This allows APPJ to treat delicate surfaces without damaging as well as robust surfaces. Major utilizations of APPJ are etching or deposition of silicon dioxide film, and decontamination and sterilization of medical devices and industrial equipment.

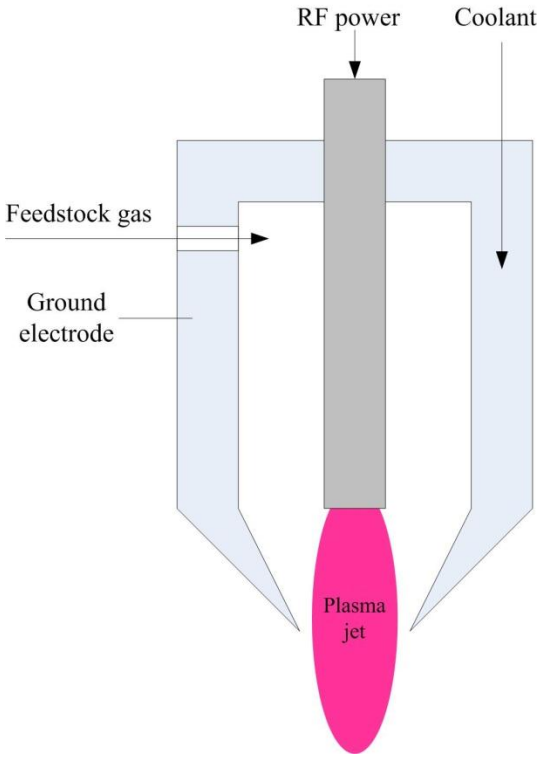

Figure 1-7 Schematic of a typical atmospheric pressure plasma jet.

1.4. Conclusion

Atmospheric pressure plasma has great feature to provide abundant reactive chemical species with simple and cost efficient equipment compared to low pressure plasma. Biomedical application is one of the promising fields of these characteristics. However, atmospheric plasma application to biomedical has not been well studied nor understood due to its requirement of interdisciplinary studies (plasma physics, plasma chemistry, electrical engineering, biology, and etc.). The chapters later on are to find atmospheric plasma chemistry applications to biomedical and understand the mechanisms of plasma chemical reaction with biomaterials, dominant reactive chemical species in the plasma, and control knobs to regulate the chemical species and the process.

REFERENCES

[1] H. Raether. *Z. Phys.* **1939**, 112, 464.
[2] Yu.P. Raizer. *Gas Discharge Physics.* Berlin: Springer, **1991**.
[3] M.I. Boulos, P. Fauchais, E. Pfender, *Thermal Plasmas: Fundamental and Applications.* Volume I, Plenum Press, New York, ISBN: 0-306-44607-3, **1994**, 452.
[4] 12E. M. Bazelyan and Y. P. Raizer, *Spark Discharge,* CRC, Boca Raton, **1998**.
[5] Michael A. Lieberman and Allan J. Lichtenberg, *Principles of Plasma Discharges and Materials Processing*, 2nd Edition, A John wiley & Sons.
[6] A. Schütze, J.Y. Jeong, S.E. Babayan, J. Park, G.S. Selwyn, R.F. Hicks, *IEEE Trans. Plasma Sci.* **1998**, 26, 1685.
[7] U. Kogelschatz, *IEEE Trans.Plasma Sci.* **2002**, 30, 1401.
[8] T. Nozaki, Y. Unno, Y. Miyazaki and K.Okazaki. *15th International Symposium on Plasma Chemistry* **2001**.
[9] X. Xu. *Thin Solid Films* **2001**, 390, 237.
[10] U. Kogelschatz, B. Eliasson and E. Walter, *Pure Appl. Chem.* **1999**, 71, 1819.
[11] U. Kogelschatz, M. Hirth and B. Eliasson, *J. Phys. D: Appl. Phys.* **1987**, 20, 1421.
[12] U. Kogelschatz, *Pure Appl. Chem*. **1990**, 62, 1667.
[13] El Dakrouri, J. Yan, M. C. Gupta, M. Laroussi and Y. Badr, *J Phys D: Appl Phys* **2002**, 35, 109.
[14] H. E. Wagner, R. Brandenburg, K. V. Kozlov, A. Sonnenfeld, P. Michel, J. F. Behnke, *Vacuum* **2003**, 71, 417.

CHAPTER 2. REVIEW OF RF DRIVEN ATMOSPHERIC PRESSURE PLASMAS FOR BIOMEDICAL APPLICATIONS

Due to the lower breakdown voltages and large amount radical generations compared to low frequency (< 1 MHz) plasmas, many researchers have studied RF (> 1 MHz) driven atmospheric pressure plasmas for various biomedical applications such as sterilization, wound healing, tissue removal, surface modification of biomaterials. Large amount reactive chemicals generated in RF plasmas enable sterilization without toxic chemicals, normally used in conventional sterilization method. Plasma-assisted electrosurgery helps to reduce the direct current through body used for pure electrosurgical process. RF Plasma can be tailored for modification of biomaterials to hydrophilic or hydrophobic depending on its application. RF plasma spray can make a film of nanoparticles or nanostructures on the surface of biomaterials. This work has been previously published in "Atmospheric-pressure plasma sources for biomedical applications" [1].

2.1. Sterilization

A low-pressure and low-temperature RF plasma has gained recognition for its efficacy and low cost [2–5] since RF glow discharge sterilizations operating below 1 Torr were successfully achieved in the early 1960s [6]. Usually, a low pressure plasma is employed in combination with a working gas, such as hydrogen peroxide or peracetic acid vapor, which generates microbiocidal active species when it reacts with the plasma [7, 8]. Plasma sterilization methods function near room temperature, in much less time than autoclaving and ethylene oxide exposure. They are used to sterilize workpieces in volumes of a few tens of liters near room temperature, and require from 1 to 2 h to complete a cycle [7]. A combination of working gases is effective in removing and killing microorganisms by generating oxygen, hydroxyl free radicals, presumably other

reactive species, and UV photons. Although the inactivation mechanism is not fully understood, a number of studies have been made to understand it. It has been shown that in the plasma inactivation treatment the major role is played by the neutral species [9, 10], which has led to attention being focused on the post-discharge region, where active radicals and excited species, rather than charged particles, are present [11–13]. The post-discharge region has the advantages of much lower temperature and an absence of charged species, as compared with the discharge zone, which could damage the materials to be sterilized.

Recently, APP has attracted interest in the field of sterilization research since it requires only a small space for inherent miniaturized systems, and uses an inexpensive and simple process, while low-pressure plasma requires a larger space for a complicated system and more expensive vacuum equipment.

It has been reported by Ohkawa et al [14] that an RF-driven DBD can sterilize various kinds of bacteria including spore-forming bacteria: Bacillus atrophaeus, G. stearothermophilus, and mold and yeast-like fungus: Salmonella enteritidis, S. aureus, C. albicans and Aspergillus niger. The DBD electrode was made of an aluminum block 150 mm in length and 50 mm in width. The electrodes were cooled by circulation of a coolant, and were covered with quartz plates. A mixture of helium (1500 sccm) and oxygen (1 sccm), which showed the maximum emission intensity of excitation of oxygen atoms via energy transfer from metastable helium atoms, at 777 nm, was supplied from an array of apertures; 670 W RF power at 27.12 MHz was used to sustain the plasma. The RF pulse width and interval were fixed at 10 μs.

The disinfection times of plasma treatment and dry heat treatment were compared at 90 ^{o}C. A control group of biological indicators were exposed in dry-heat treatment at an equivalent gas temperature. C. albicans, S. enteritidis and E. coli were sterilized after a 1 min plasma treatment,

while they remained alive after a 1 min high-temperature treatment. S. aureus was sterilized after a 5 min plasma treatment.

Studies to understand the RF plasma sterilization mechanism at atmospheric pressure have been reported by several groups. Sharma et al reported that UV plays a primary role in the bacteria inactivation process, whereas plasma radicals play a secondary role when using 60 MHz slot plasma [15]. The plasma consisted of an external open-slot electrically grounded hollow electrode and an opposing internal 60 MHz RF-powered wedge-shaped electrode. The open-slot width was fixed at 200 μm and interelectrode spacing was fixed at 500 μm. The length of the electrode was approximately 75 mm. The sample was kept 2.5 mm to 1 cm below the open reactor slots. The surfaces were processed in open air. A matching network optimized power transmission to the plasma reactor from the power supply. Mixtures of rare gas (argon or helium) and oxygen were tested at flow rates of 5–20 L min^{-1} and 6–20 sccm, respectively. The experimental results showed that there was no significant change in the relative inactivation of E. coli as the distance of the sample from the electrode was varied. This indicates that heat does not play a significant role in inactivation, considering that the temperature was less than 40 ^{o}C.

A comparison of 60 MHz RF power with 13.56 MHz showed that the higher fluxes produced by the 60 MHz plasma resulted in a higher level of inactivation. The inactivation rate was not significantly affected by oxygen addition since it made the discharge slightly unstable and hence had a net negative influence on the flux of active species. The inactivation in the sample covered with MgF_2 was much higher than in the sample covered with a polystyrene lid. This suggested that UV played the major role in the inactivation process. A helium plasma was not as effective as an argon plasma in inactivating the bacteria. Increasing power yielded increased inactivation. This can be attributed to greater dissociation of radicals and higher photon fluxes at higher power

levels. In addition, a synergetic effect was also observed in the combination of UV radiation and radicals, which caused a higher rate of inactivation than using the two treatments in isolation. Gas temperature had a negligible effect on inactivation.

However, Brandenburg et al demonstrated that the direct interaction of the plasma with the microorganisms is the key to the lethal effect when using an RF-driven argon plasma jet [16]. A non-thermal 27.12 MHz RF-driven plasma jet was used for antimicrobial treatment of samples made on heat-sensitive materials. The plasma jet consisted of an outer nozzle made of ceramic (diameter 7 mm) and a needle electrode mounted at the center. The RF voltage was applied to the inner electrode and the argon gas flowed through the nozzle. The surrounding air and the substrate acted as the grounded electrode. The plasma was generated in the nozzle starting from the point of the needle electrode and expanded into the surrounding air outside the nozzle. Strips inoculated for microbiological tests were made of polyethylene (PE) since most medical products to be treated in the future will contain this or similar plastics. The plasma jet was operated at 20 W and the gas flow was 20 slm. Direct interaction of plasma was investigated by three different tests on both B. atrophaeus spores and E. coli samples on PE strips.

Treatment by plasma jet, shielding the sample from the plasma using a quartz glass plate to investigate the UV radiation effect, and flowing a hot air stream with temperature as well as air flow conditions corresponding to the plasma treatment to exclude a heat effect, were compared by means of the reduction factor on each sample. These tests demonstrated that the lethal effect of the plasma is based on a direct interaction of the plasma with the microorganisms. UV radiation or heat alone resulted in lower reduction factors. Thus, the separate effects of these components could not explain the antimicrobial effect of the plasma.

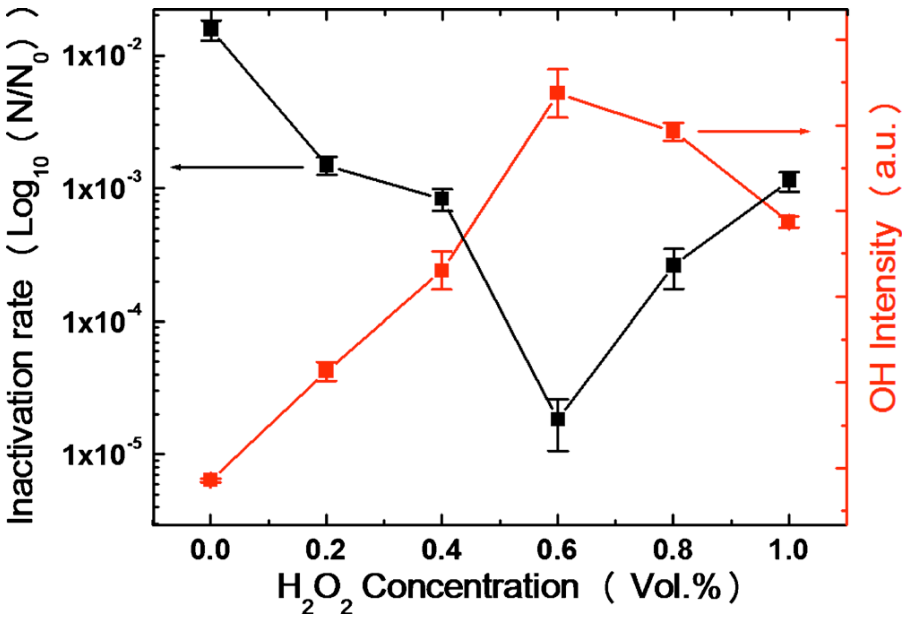

Figure 2-1 Inactivation rate of S. mutans (black squares) and corresponding integrated OH intensity (red squares) as a function of H_2O_2 vapor concentration [17].

Kang et al [17] investigated the effect of H_2O_2 entrained in feedstock argon gas on the inactivation of Streptococcus mutans by means of an RF-driven plasma torch that consisted of a ceramic tube surrounded by a 13.56 MHz powered electrode and a grounded electrode. Hydrogen peroxide vapor was included in the feed gas with a concentration of 0 – 1 % (v/v) by flowing argon gas through a bubbler containing 30 % H_2O_2. The bacterial inactivation reached maximum reduction at 0.6 % H_2O_2 vapor and the maximum intensity of optical OH emission (308 nm) coincided with that concentration (figure 2-1).

2.2. Tissue Removal and Purposeful Coagulation

RF plasma applications for tissue removal and coagulation during surgery has an advantage as a safe energy source in human or animal bodies, since nerve and muscle stimulation by current through the body ceases at 100,000 cycles/second (100 kHz). Traditional electrosurgeries used this RF to cut and coagulate tissue with minimal heat damage. Plasmas had significantly

faster incision times and less incisional blood loss than a scalpel or laser, with no significant difference in subjective or objective patient pain [18]. RF ablation procedures can be performed in open surgery, percutaneously, or laparoscopically, at the physician's discretion. RF plasmas have been used as a coagulator to stop bleeding (valleylab, argon-enhanced coagulator) [19]. This type of plasma used a monopolar electrode to generate the plasma and a ground pad to complete the circuit loop. Inadequate use of the ground pad may cause a pad site burn [20].

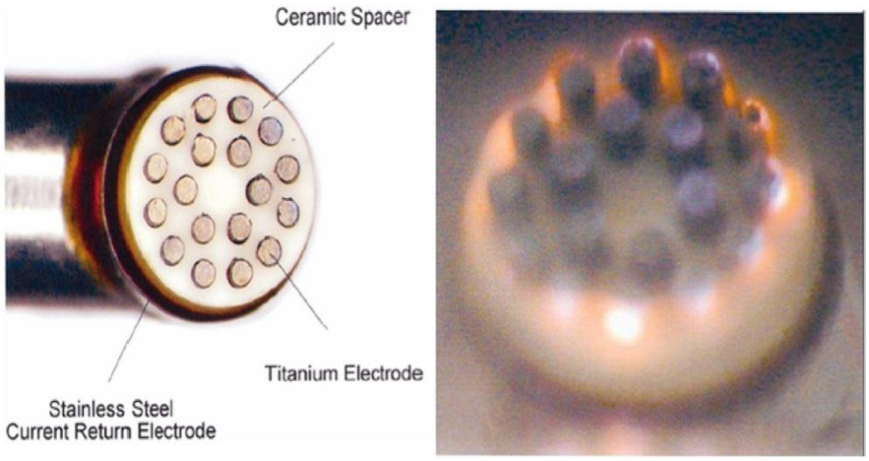

Figure 2-2 Photographs of (a) the tip of an ArthroCare (3.5 mm diameter, 90 ° oriented) surgical probe, (b) the plasma formed on the probe when energized in saline solution [22].

Recently, RF plasmas at atmospheric pressure have been developed for less lateral heat damage, shorter treatment time, elimination of direct current flowing through the body to prevent pad site burn, and shorter post-operative healing time. ArthroCare manufactured a bipolar plasma device for tissue removal and coagulation in a wide variety of designs (figure 2-2). Their coblation-based devices operated at relatively low temperatures (40 – 70 ^{o}C) compared with traditional surgical tools (more than 400 ^{o}C), thereby minimizing the damage to surrounding healthy tissue [21]. This can be achieved by operating in a conductive aqueous environment such as normal saline (0.9 % NaCl in H_2O). The operation voltage was 100 – 300 V at a frequency of

100 – 500 kHz, and each individual electrode was powered from an individual power supply. Application of high voltage to electrodes led to a stream of bubbles generated in their vicinity. Details of vapor formation were not fully understood, but it was expected that a very thin layer of vapor was formed near the electrode, leading to a larger electric field within the layer and a lower number density of molecules in the vapor with respect to the liquid. As a result, large reduced electric field values, E/N, were produced. Therefore, electrical breakdown of the vapor occurred and a plasma formed near the electrode [22].

These bipolar devices have the advantage of preventing current through the body, which may lead to pad site burn and temperature increase in the body [20]. Since the electrode did not touch the tissue, charring deposited on the electrode was relatively low compared with existing conventional electrosurgery technologies. These commercialized plasma surgical devices use plasma as a heat source to remove or coagulate cells.

Below we give a brief description of CSU devices and tissue removal results to allow the reader to see where this thesis is going to provide a new pathway for surgery that has lower temperature and is more selective to different tissue types which matches or exceed prior art electrosurgery tools.

Even though the plasma chemical reaction with cells was unclear, there were some efforts to improve and control tissue removal ability in terms of etch depth and etch profile by a plasma chemical reaction using a simple RF argon plasma jet [23] (figure 2-3). Chemical additives containing chlorine in the argon carrier gas increased the tissue removal rate (figure 2-4). The material removal rate using different CHxClx additives increased with both (1) the molecular chlorine content (x = 2, 3, 4) of the selected additive, and (2) the concentration of haloalkane vapor in the gas stream. This was attributed to the generation and delivery of chemically reactive

radicals from the plasma to the tissue, followed by the formation of volatile products (i.e. a chemical, rather than physical or thermal, tissue removal process).

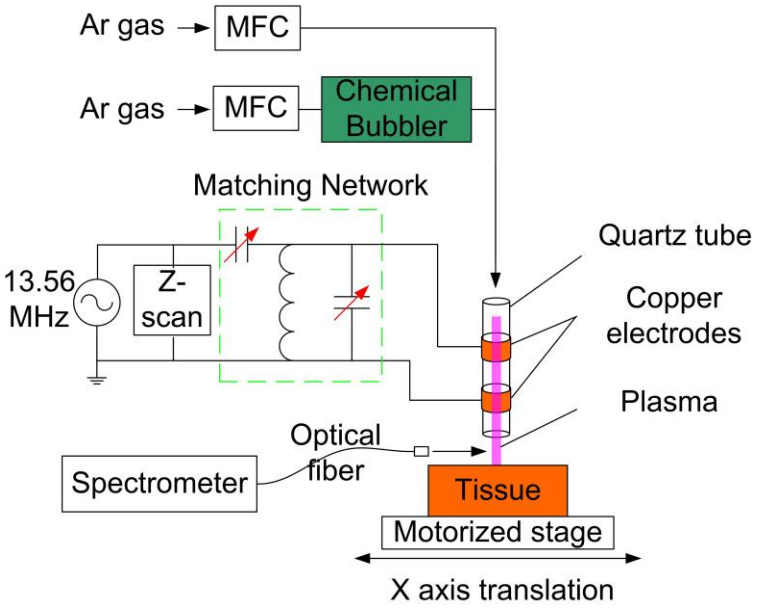

Figure 2-3 CSU experimental set-up employed for achieving both directional and selective tissue removal via thermal plasma chemistry [23].

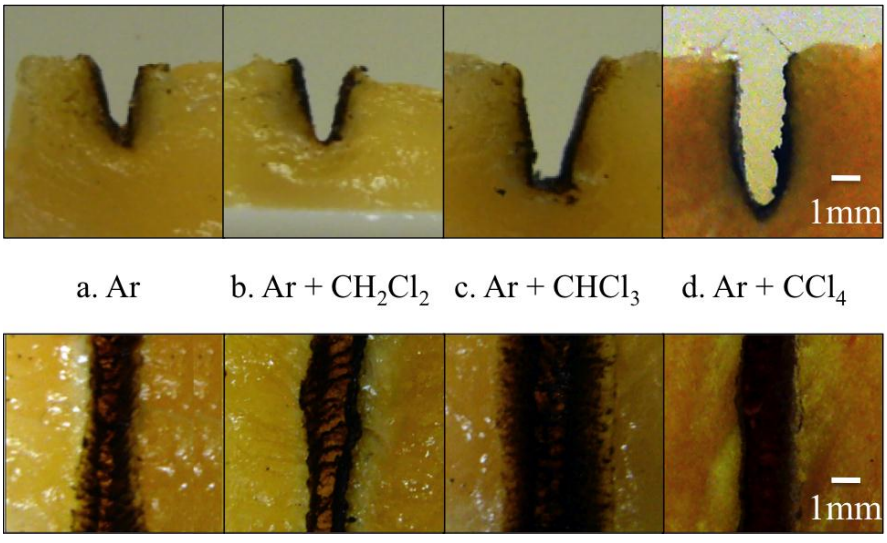

Figure 2-4 Cross-section and plan view comparisons of plasma tissue cutting in (a) Ar and Ar with the addition of haloalkanes (b) CH_2Cl_2, (c) $CHCl_3$ and (d) CCl_4; 13.56 MHz RF power: 30 W, tissue treatment speed: 10 mm $\cdot s^{-1}$ [23].

2.3. Surface Modification

2.3.1. Surface Modification.

Barker et al discovered that plasma surface treatment could support the growth of cells [24]. Such surface modification has a number of applications, including selective culturing of bacteria and cells, increasing the biocompatibility of implants, and making surgery tools more resistant to bacteria.

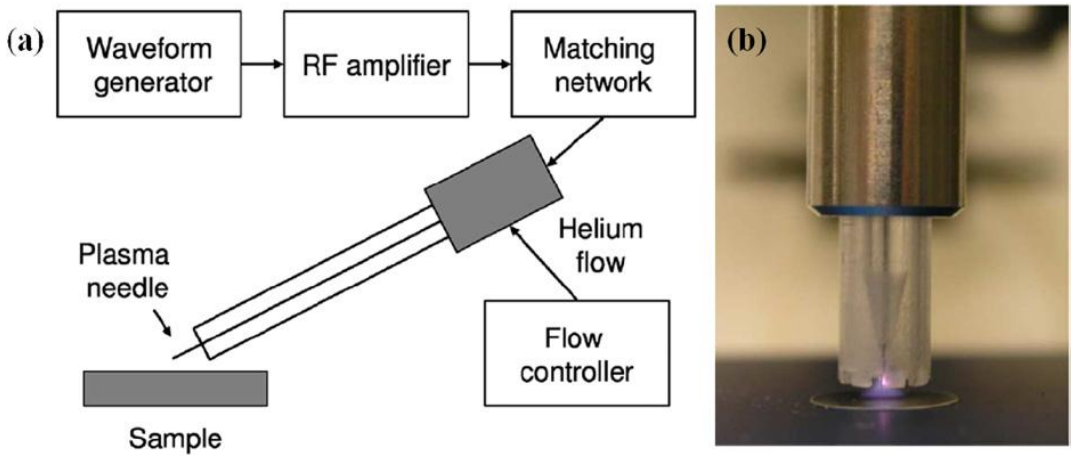

Figure 2-5 (a) Schematic of the experimental set-up; (b) when an RF voltage was applied to the tungsten electrode, a microplasma was generated [25].

Non-thermal RF needle plasma was developed to study the plasma treatment effect on the growth of E. coli and S. mutans on a substrate at the Eindhoven University of Technology [25]. The plasma needle consisted of a metal wire and a surrounding Perspex tube. The helium gas flowed through the Perspex tube (figure 2-5). A 13.05 MHz RF voltage was applied to the tip of the needle. The waveform generated at the signal generator was amplified to provide enough power to generate plasma, and a matching network was used to maximize the delivered power.

The RF needle plasma treated polystyrene and Perspex surfaces, and polystyrene showed the most localized effect, whereas Perspex had the largest area of reach. The wettability increase was

temporary for Perspex, while polystyrene could be made long-lastingly hydrophilic. Efficient bacterial deactivation was found under low-power conditions. Plasma treatment accelerated the growth of aerobic E. coli and inhibited the growth of anaerobic S. mutans.

Control of surface properties in microfluidic systems was an indispensable prerequisite for the success of bioanalytical applications. Poly (dimethylsiloxane) (PDMS) microfluidic devices were hampered by unwanted adsorption of biomolecules and the lack of methods to control electro-osmotic flow (EOF). Among the various methods of hydrophilic treatment, a new cleaner technology is available to treat PDMS. An atmospheric RF plasma can be used to create hydrophilic surfaces. Constructing hydrophilic surfaces without changing the true character of that surface has previously been costly and time consuming. Using APPs significantly reduced both cost and time [26].

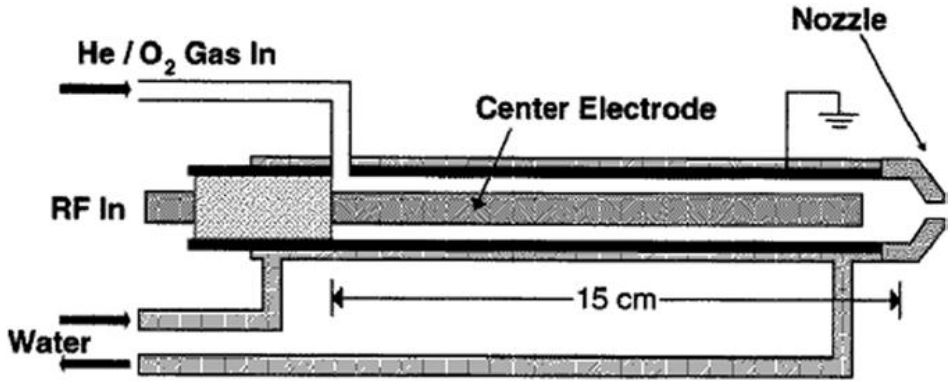

Figure 2-6 Schematic of the prior art atmospheric-pressure plasma jet [27].

Gao et al reported polyamide 6 film treatment with He/CH_4 RF plasma at atmospheric pressure. The plasma treatment was carried out using an APPJ (Atomflo-R, Surfx Company, USA) [27]. The carrier gas, helium (20 l · min^{-1}), was mixed with reactive gas, CF_4 (0.2 l · min^{-1}). The APPJ employed a capacitively coupled electrode design, as shown in figure 2-6 [28].

Water contact angle on the surface increased with treatment time after 30 s of treatment. This indicates the introduction of hydrophobic fluorinated groups onto the PA 6 film surface. The XPS elemental analysis revealed that the plasma etching and oxidation processes on the PA 6 surface were more dominant at the early stage of plasma treatment, while the fluorination reaction by CF_4 plasma was probably more dominant for longer treatment durations, consistent with the literature [29].

2.3.2. Surface Coating by Plasma Spraying.

Plasma spraying is widely used to prepare ceramic coatings. During plasma spraying, the temperature in the plasma is relatively constant at ~12,000 K and almost all materials can be melted. This thermal plasma has proven to be an effective tool for the fabrication of nanoparticles and nanostructured films and coatings. Nanoparticles synthesized by thermal plasmas are directly deposited onto a substrate to fabricate a nanostructured film [30]. The incorporation of bioinert ceramics, such as yttria-stabilized zirconia (YSZ), alumina and titania into a hydroxyapatite (HA) matrix has demonstrated significant improvement in mechanical properties [31–33] without substantial compromise in biocompatibility [34]. Furthermore, an in vitro study has shown that nanoparticles such as Al_2O_3 andTiO_2 have a significant capability to enhance osteoblast adhesion on the surface [35]. Zirconia is one of the most promising ceramics because of its good adhesion to metal substrates, its biocompatibility, and its superior mechanical properties with respect to other ceramics such as alumina [36].

One example of these plasma sprayings is hydroxyapatite/nano-zirconia composite coatings prepared by a high-velocity oxy-fuel (HVOF) spray process of RF plasma [37]. Li et al showed that nanostructured powder coating could be prepared in this way for biomaterials due to the

homogeneity of the coating for improved mechanical strength, no obvious phase change from the primary powder's phase composition, and limited reaction between HA and zirconia mainly because of thermal decomposition of HA in the HVOF flame, which is beneficial for the biological performance of the coatings.

Heat treatment of the HA/nano-zirconia coating at 750 ^{o}C and 30 min improved the homogeneity of the coating by equalizing the phase compositions and achieved uniform Young's modulus throughout the nanostructured coating. Young's modulus of the coating was found to attain a maximum value of ~130 GPa. An in vitro test of incubation in simulated body fluid (SBF) solution showed that a bone-like apatite layer precipitated on the HA/nano-zirconia coating surface. This suggested satisfactory bioactivity of the coatings [38].

REFERENCES

[1] G Y Park, S J Park, M Y Choi, I G Koo, J H Byun, J W Hong, J Y Sim, G J Collins and J K Lee, *Plasma Sources Sci. Technol.* **2012**, 21, 043001.
[2] Adler S, Scherrer M and Daschner F, *J. Hosp. Infect.* **1998**, 40, 125.
[3] Lerouge S, Wertheimer M, Marchand R, Tabrizian M and Yahia L H, *J. Biomed. Mater. Res.* **2000**, 51, 128.
[4] Moisan M, Barbeau J, Moreau S, Pelletier J, Tabrizian M and Yahia L H, *Int. J. Pharm.* **2001**, 226, 1.
[5] Mogul R, Bol'shakov A A, Chan S L, Stevens R M, Khare B N, Meyyappan M and Trent J D, *Biotechnol. Prog.* **2003**, 19, 776.
[6] D'Agostino R, *Plasma Deposition, Treatment, and Etching of Polymers*, New York: Academic **1990**.
[7] Rutala W A, Gergen M F and Weber D J, *Am. J. Infect.* **1998**, 26, 393.
[8] Vassal S, Favennec L, Ballet J J and Brasseur P, *Am. J. Infect.* **1998**, 26, 136.
[9] Moreau S, Moisan M, Tabrizian M, Barbeau J, Pelletier J, Ricard A and Yahia L H, *J. Appl. Phys.* **2000**, 88, 1166.
[10] Lim H R, Baek H S, Lee M H, Woo Y I, Han D W, Han M H, Baik H K, Choi W S, Park K D and Chung K H, *Surf. Coatings Tech.* **2008**, 202, 5768.
[11] Ricard A, *J. Phys. D: Appl. Phys.* **1997**, 30, 2261.
[12] Belmonte T, Thiebaut J and Mezerette D, *J. Phys. D: Appl. Phys.* **2002**, 35, 1919.
[13] Pintassilgo C, Loureiro J and Guerra V, *J. Phys. D: Appl. Phys.* **2005**, 38, 417.
[14] Ohkawa H, Akitsu T, Tsuji M, Kimura H, Kogoma M and Fukushima K, *Surf. Coat. Technol.* **2006**, 200, 5829.
[15] Sharma A, Pruden A, Stan O and Collins G J, *IEEE Trans. Plasma Sci.* **2006**, 34, 1290.
[16] Brandenburg R, Ehlbeck J and Stieber M, *Contrib. Plasma Phys.* **2007**, 47, 72.
[17] Kang S K, Choi M Y, Koo I G, Kim P Y, Kim Y, Kim G J, Mohamed A A H, Collins G J and Lee J K, *Appl. Phys. Lett.* **2011**, 98, 143702.
[18] Pearlman N, Stiegmann G, Vance V, Norton L, Bell R, Staerkel R, Van Way C III and Bartle E, *Arch. Surg.* **1991**, 126, 1018.
[19] Vilos G, Latendresse K and Gan B S, *Am. J. Surg.* **2001**, 182, 222.
[20] Massarweh N N, Cosgriff N and Slakey D P, J. *Am Coll. Surg.* **2006**, 202, 520.
[21] Chinpairoj S, Feldman M D, Saunders J C and Thaler E R, *Laryngoscope* **2001**, 111, 213.
[22] Graham W and Stalder K, *J. Phys.: Conf. Ser.* **2007**, 71, 012013.
[23] Koo I G, Moore C A, Choi M Y, Kim G J, Kim P Y, Kim Y S, Yu Z and Collins G J, *Plasma Process. Polym.* **2011**, 8, 1103.
[24] Barker S L and LaRocca P J, *Methods Cell Sci.* **1994**, 16, 151.
[25] Sladek R E J, Baede T A and Stoffels E, *IEEE Trans. Plasma Sci.* **2006**, 34, 1325.
[26] Hong S M and Kim S H, *J. Phys.: Conf. Ser.* **2006**, 34, 656.
[27] Gao Z, Sun J, Peng S, Yao L and Qiu Y, *Appl. Surf. Sci.* **2009**, 256, 1496.
[28] Jeong J, Babayan S, Tu V, Park J, Henins I, Hicks R and Selwyn G, *Plasma Sources Sci. Technol.* **1998**, 7, 282.
[29] Dreux F, Marais S, Poncin-Epaillard F, Metayer M and Labbe M, *Langmuir* **2002**, 18, 10411.
[30] Shigeta M and Murphy A B, *J. Phys. D: Appl. Phys.* **2011**, 44, 174025.
[31] Chang E, Chang W, Wang B and Yang C, *J. Mater. Sci.* **1997**, 8, 193.

[32] Fu L, Khor K A and Lim J P, *J. Am. Ceram. Soc.* **2002**, 85, 800.
[33] Kurzweg H, Heimann R, Troczynski T and Wayman M, *Biomaterials* **1998**, 19, 1507.
[34] Chang E, Chang W J, Wang B C and Yang C Y, *J. Mater. Sci.* **1997**, 8, 201.
[35] Webster T J, Siegel R W and Bizios R, *Biomaterials* **1999**, 20, 1221.
[36] Piconi C and Maccauro G, *Biomaterials* **1999**, 20, 1.
[37] Li H, Khor K, Kumar R and Cheang P, *Surf. Coat. Technol.* **2004**, 182, 227.
[38] Khor K, Li H, Cheang P and Boey S, *Biomaterials* **2003**, 24, 723.

CHAPTER 3. TISSUE REMOVAL AND REMOVAL PROFILES BY ATMOSPHERIC PLASMA JET

3.1. Chemical-Driven Tissue Removal

To our knowledge our tissue removal studies are the first reported. Moreover, we obtain less thermal damage as compared to conventional electrosurgery to contiguous tissue regions. We demonstrate the application of RF-excited plasma to remove localized regions of ex vivo tissue. While some limited tissue removal occurs, when using discharges in rare gases alone, the addition of chemical precursors resulted in an enhancement of etch depth and etch profile under essentially identical plasma conditions of delivered power, applied voltage, and gas flow. Specifically, the material removal rate in our experiments using different CHxClx additives increased with both (1) the molecular chlorine content (x=2,3,4) of the selected additive, and (2) the concentration of haloalkane vapor in the gas stream. We attribute this enhancement to the generation and delivery of chemically reactive radicals from the plasma to the tissue, followed by formation of volatile products (i.e., a chemical, rather than physical or thermal, tissue removal process). In addition we observed that cross-sectional etch profiles differed with the chosen haloalkane additive chemistries, indicative of corresponding differences in chemistries on profile side-walls versus bottom walls [1].

3.1.1. Introduction

Atmospheric pressure discharges have received considerable research interest over the past decade [2]. By virtue of their open-air operation at low gas temperatures, these plasmas show promise for easy access to and unique interactions with biological materials as described below.

Electrosurgery (ES) is a widespread technology used to divide tissues and control blood loss during a surgical procedure. As first described by Wyeth [3] in 1924, the current density is the dominant cutting mechanism. ES methods to date use metallic electrodes to deliver electrical energy into tissues to induce localized heating and tissue removal [4]. The choice of applied voltage magnitude, duty cycle, or waveform shape allows emphasis on cutting or coagulation as a result of localized resistant heating [5].

The potential role of chemical reactions as the driving mechanism in ES has been suggested [6], but has never been demonstrated to be a dominant process to the extent demonstrated herein. Exploration of plasma-driven chemical reactions with tissues represents a new pathway in surgical medicine. Clearly the very complex nature of tissue together with variety of potential chemical reaction pathways suggests many possibilities for tissue selective surgery with minimal thermal effects. For perspective, it is noted that plasma-based etching of simple inorganic and organic thin films at low pressure is a key enabling technology for integrated circuitry, optoelectronics, and nanostructured materials due to the ability to achieve a material-selective and spatially directional etch [7].

Biological materials, however, are best treated in open air [8, 9] as demonstrated in studies of bacterial inactivation and biofilm remediation [10]. Electrically driven atmospheric plasma discharges can generate and deliver fluxes of long-lived plasma species to tissue surfaces to induce reactions. These non-equilibrium plasmas typically possess electron temperatures of 0.5-5 eV [11] that are capable of breaking many chemical bonds, while T_{gas} and T_{ion} are relatively cool at 20 - 200 meV and thus impart limited thermal energy to the tissue surface. For this reason non-equilibrium plasmas present a potentially advantageous means to provide specific

chemical radicals, such as O_2 (a^1D_g), at ~10 mmole per hour rates [12-13], corresponding to ~10^{18} species per minute for a 1 mm diameter plasma plume.

3.1.2. Methods

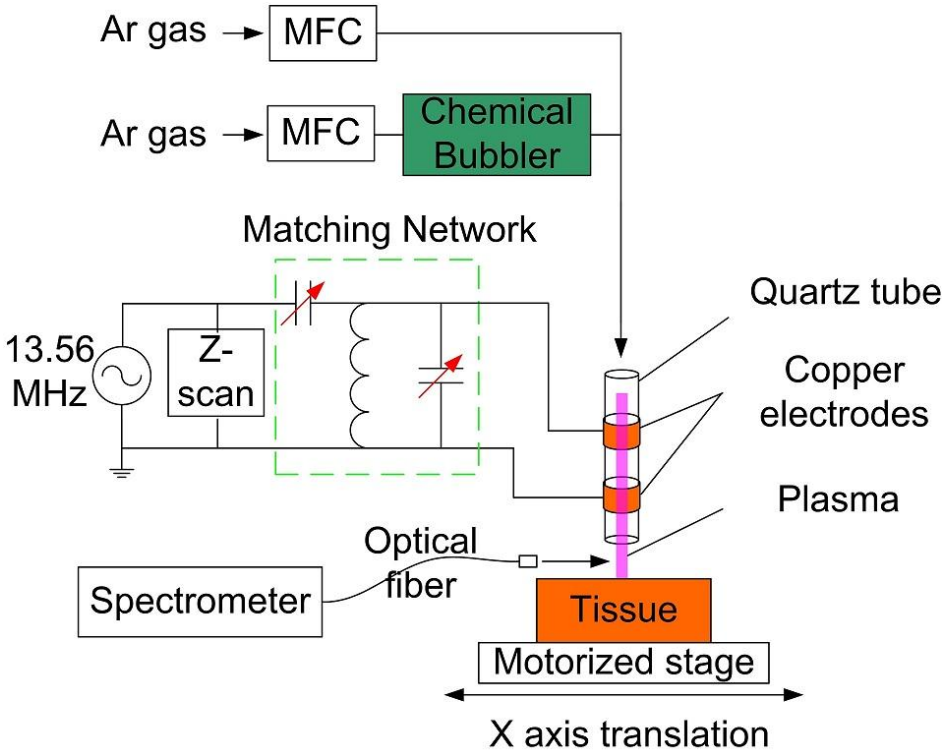

Figure 3-1 CSU experimental set-up employed for achieving both directional and selective tissue removal via thermal plasma chemistry. Quartz tube: 1 mm O.D., 0.8 mm I.D. The total Ar flow rate was 470 sccm and 20 µl/min of each chemical (CH_2Cl_2, $CHCl_3$ and CCl_4) was added using chemical bubbler.

The experimental system employed is shown in Figure 3-1. It consists of a 30 mm length of quartz tubing (1.0 mm o.d., 0.8 mm i.d.) connected to independent sources of rare gas and chemical precursor. The powered and grounded electrodes employed 0.5 mm thick and 2 mm wide copper strap. The gap between the two electrodes were 10 mm, long enough to prevent the outside arc between the electrodes. The ground electrode was located at 3 mm above the bottom of the quartz tubing. The chemical feedstock was contained in a 10 ml cylinder sealed with a

rubber stopper. Stainless steel tubing of 1.6 mm outer diameter went through the stopper and delivered argon flow to entrain the chemical feedstocks. The flow rate of the chemical feedstock was calibrated with the argon flow rate through the bubbler. The other argon flow was combined with the argon entraining the feedstock gas to keep the constant total flow rate.

We delivered 13.56 MHz RF electrical power of 30 watts via capacitive dielectric coupling. Argon (Ar) gas flow and a glass bubbler (Ace Glass) achieved CCl_4 (Sigma-Aldrich) liquid-equivalent flow rates of 20 µl/min and 470sccm of argon flow rate. To verify the tissue removal results with different chemicals, optical emission spectra were taken for 200-800 nm ranges using Ocean optics model HR4000CG-UV-NIR (300 lines/mm grating, 0.75 nm FWHM resolution). The plasma effluent was delivered at controlled distances above tissue samples that were moved laterally on a three-axis translation stage with motorized (x-axis) and manual (y and z axes) actuation as shown in Figure 3-1. We demonstrate below that our CSU plasma-chemical jet is capable of extending material removal (etching) to biomaterials such as tissue, specifically to achieve a tissue removal rate with a mixture of both physical and chemical mechanisms acting in concert that exceeds etching rates with rare gases (physical mechanisms) alone. The presence of chemical species is demonstrated in Figure 3-2 which shows typical optical spectra emitted from Ar both without and with an entrained CCl_4 vapor. Figure 3-2 clearly shows the presence of Cl, Cl_2, and C_2 species in addition to the excited Ar neutral species [14-16], when haloalkane chemistry is added to the plasma jet. Cl_2 emission at 258 nm [17, 19] from Ar, Ar/ CH_2Cl_2, Ar/$CHCl_3$, and Ar/CCl_4 is shown in Figure 3-3 to compare the relative amount of Cl_2 generated in the plasma, which contribute to the tissue removal rate.

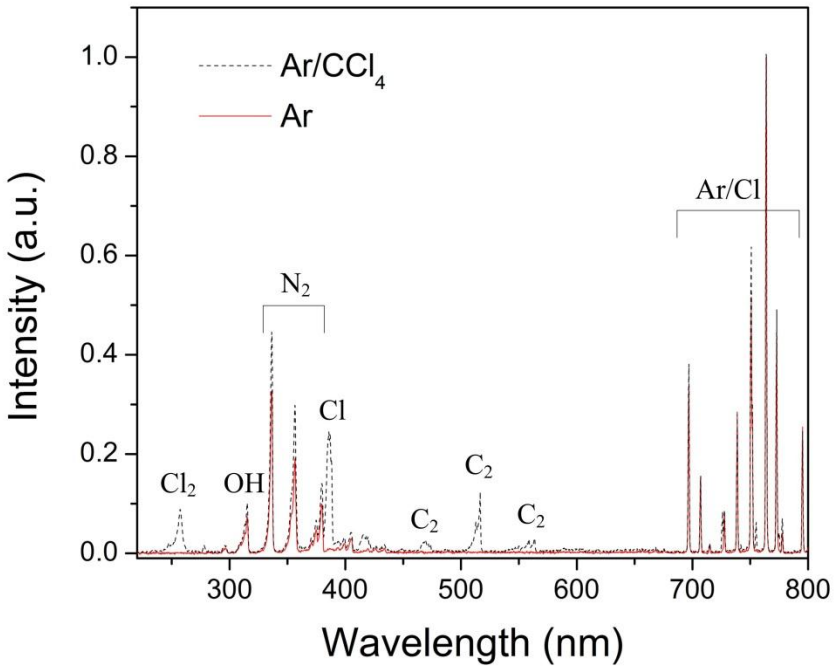

Figure 3-2 Optical emission spectra from species present in atmospheric plasmas. Spectra emitted from (a) pure Ar and Ar/CCl_4 are both presented. Optical emission integration time: 100 milliseconds, scans to average: 1, boxcar width: 0. Each spectrum underwent baseline subtraction and each was individually normalized. Cl_2 and C_2 are most abundant radicals, and we judge that the latter leads to carbon deposits observed on the tissue surface.

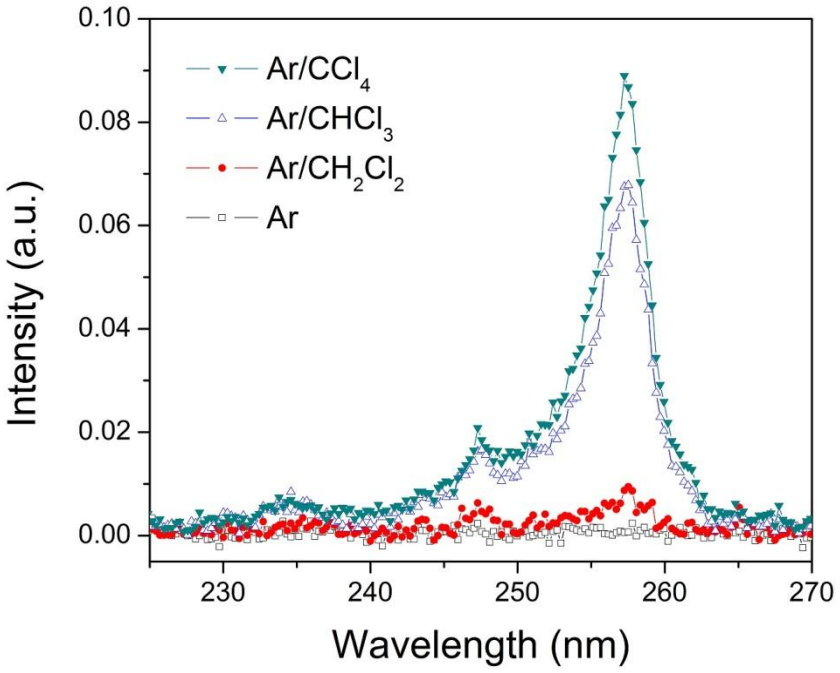

Figure 3-3 Optical emission spectra from atmospheric plasmas emitted from Cl_2 emission band at 258 nm[16,18] from pure Ar, Ar/CH_2Cl_2, $Ar/CHCl_3$ and Ar/CCl_4. Cl_2 intensity is Ar < Ar/CH_2Cl_2 < $Ar/CHCl_3$ < Ar/CCl_4. Optical emission integration time: 100 milliseconds, scans to average: 1, boxcar width: 0.

3.1.3. Results and Discussion

To examine plasma tissue removal capability, skinless chicken breast tissue was divided into ~20 mm square samples approximately 10 ± 2 mm thick. Samples were placed on the platen of the x-y stage and moved in the x direction at speeds of 10 mm/sec through the plasma effluent at distances of 3 mm from the end of the quartz tube. We emphasize that there was no physical contact between plasma tube and tissue during the removal process. Consistent with conventional ES, we observed that tissue removal employing plasmas with Ar alone results in a thermal removal process coupled with tissue charring, desiccation, and limited tissue removal rates. With the addition of chemical additives to the plasma volume we observed changes in both rates of removal and removal profiles. Figure 3-4 shows cross-sectional and plan views of

tissue samples treated under pure rare gas and rare gas plus chemistry conditions and 13.56 MHz RF electrical power 30 W. In Ar alone (Figure 3-4a), a purely thermal tissue removal process occurs and collateral blanching (whitening of contiguous tissue) can be visually observed due to desiccation and/or denaturation of proteins [18]. The tissue remained intact with little or no removal unless exposure times of several minutes were used. In contrast, Figure 3-4b displays the same views of a second sample treated with plasma with an additional vapor flow of CH_2Cl_2. The exposure time was several seconds, yet a comparable removal rate was observed. Care was exercised to maintain consistency in tissue exposure method and duration, translation speed, gas flow rate, and delivered power. We attribute the difference in tissue removal rate to non-thermal chemical-assisted tissue removal processes.

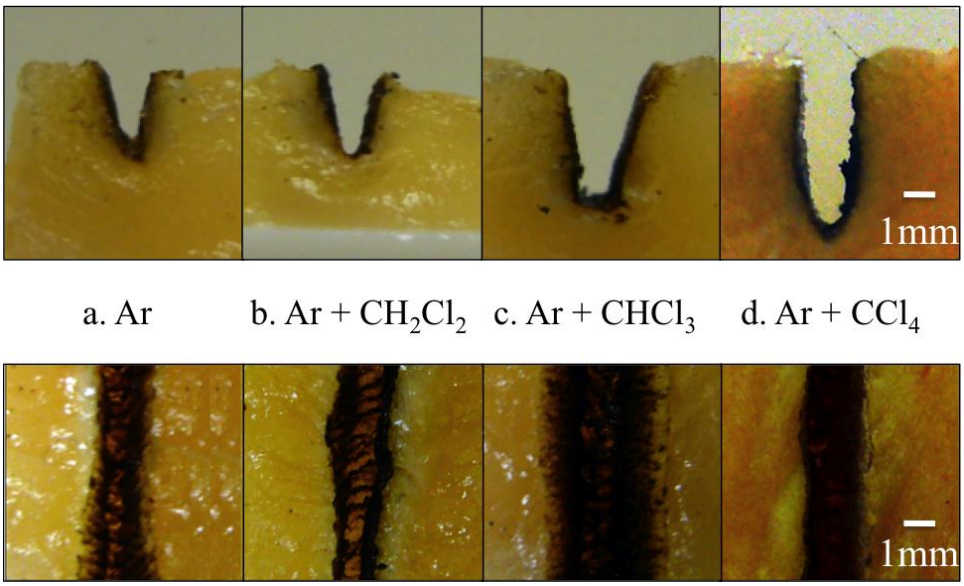

Figure 3-4 Cross-section or end views and plane view comparisons of plasma tissue cutting in (a) Ar and Ar with the addition of haloalkanes (b) CH_2Cl_2, (c) $CHCl_3$, and (d) CCl_4. 13.56 MHz RF power: 30 W, tissue treatment speed: 10 mm/sec.

To further understand the observed tissue removal we compared changes in tissue removal profiles while replacing the CH_2Cl_2 with the haloalkanes $CHCl_3$, and CCl_4 as the chemical

feedstock, as shown in Figures 3-4c and 3-4d. The increasing molecular chlorine content in the etchant source liquid was observed to increase both etching depth and width, with typically a stronger effect in the former case. Figure 3-3 also shows that the Cl_2 emission [17, 19] intensity increases as the molecular chlorine content increases. The presence of blackened material on the side and bottom walls of the tissue removal profiles of Figure 3 was estimated to be a combination of both tissue charring and carbon deposition based on two observations: (1) the strong Swan band emission observed in Ar/CCl_4 curve of Figure 3-2 indicates gas-phase reactions that form C_2 [19] molecules, an expected observation in a reaction path that results in formation of graphitic carbon depositions, and (2) the limited extent of thermal damage under the blackened material, also evidenced in histology below, argues against this material resulting from a burning or charring effect. This deposited carbon, may aid the directional nature of the tissue cut profiles, together with the directional radical and photon fluxes from plasma jets. Carbon deposits on tissue surfaces are readily removed by exposure to a rare gas-oxygen plasma treatment. Moreover, we note that with plasma jet tissue removal there was no build-up of tissue on the electrode, in contrast to typical ES cutting, where eschar deposits on the electrode occurs and increases series resistance, in turn contributing to arcing and loss of control of energy delivery to the tissue. That is, the plasma jet acts as a virtual non-stick electrode that is char free.

Further studies of the plasma-based tissue removal process are the histological sections shown in Figure 3-5. The samples were prepared by first sectioning the tissue into thin slices perpendicular to the plasma cutting direction and then fixing, embedding, and staining with Hematoxylin and Eosin (H&E), a common histological stain for tissues. A principal advantage of the H&E stain is that it accentuates cellular detail by taking advantage of acidophilic and basophilic qualities of the cytoplasm and nuclei of cells. Tissue irradiation by the plasma with Ar

alone (Figure 3-4a) was contrasted with tissue irradiation with a mixture Ar/CCl_4, (Figure 3-4b). Although an unambiguous histological assessment generally cannot be extracted from muscle tissue, these data reveal that the addition of CCl_4 to the plasma had little effect on the lateral removal rate but appears to enhance the vertical etch rate into the tissue by a factor of $> \approx 5$. This extent of directionality in tissue removal is unique to the plasma cutting method described herein as similar phenomena are not observed in our studies based on purely ES methods.

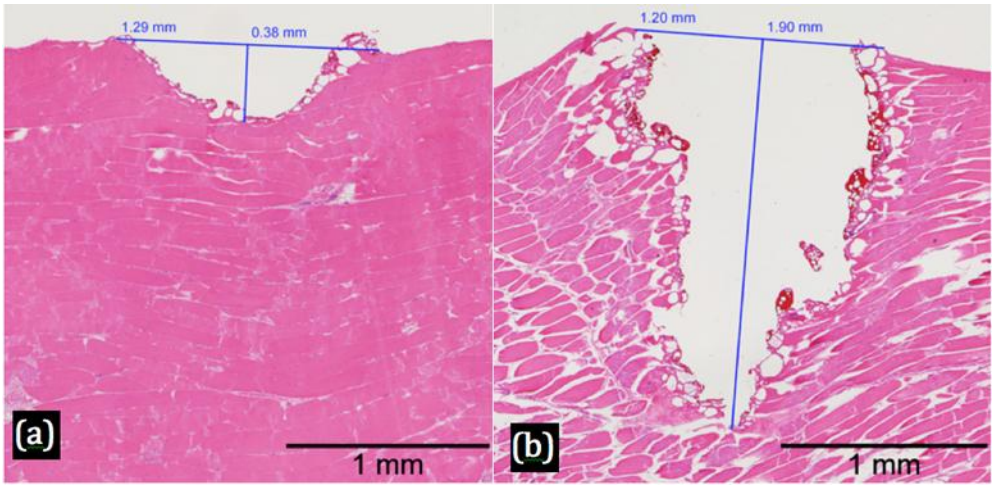

Figure 3-5 Histological section of tissue cut using (a) Ar and (b) Ar and CCl_4 plasmas, demonstrating tissue removal enhancement from the chosen reactive plasma chemistry.

3.1.4. Conclusion

In conclusion, we have demonstrated directional tissue removal using atmospheric pressure plasma. Tissue removal is assisted by chemical energy in addition to thermal energy present as demonstrated by our comparison of plasmas using rare gas alone versus rare gas plus chemical additives. An improved plasma chemical tissue removal process, with different chemistries, may offer an improved pathway to tissue-selective surgical procedures, as well as modification of chemical states and species on tissue surfaces. Clearly, alternative chemistries to haloalkanes are

more compatible with biological materials, but this work demonstrates the proof-of-principle of employing chemistry to achieve directed and selective tissue removal.

3.2. Pulsed RF Plasma Tissue Removal

Argon plasma jet was investigated for Plasma-assisted non-contact ES using both plasma and ES. In our previous study, chlorine radicals in the plasma jet were employed to improve tissue removal rate. In this study, we investigate tissue removal of pulsed RF plasma irradiation. Parameter study of pulse duty ratio and frequency are shown in terms of removal profile and heat damage. Removal profiles and heat damage are taken from the cross-section and histology of plasma irradiated tissue samples. Pulsed RF plasma shows that pulsed RF plasma can be tailored by those two parameters for high removal rate and minimal heat damage.

3.2.1. Introduction

For the last two decades, several researchers have demonstrated that pulse frequency and duty ratio of pulsed RF plasma can be used to control ion/electron densities, electron temperature, ion/neutral flux ratio, and plasma potential. It might occur transitions from electron–ion plasma to ion–ion plasma during the after-glow phase (power off period) for electronegative plasmas [20-23]. The pulsed plasma also exhibits highly selective, highly anisotropic, and charge build up damage free polycrystalline silicon etching [24-32]. Furthermore, in electrosurgery, the choice of pulsing conditions such as duty ratio and pulsing frequencies gives us a knob to control between pure cut and coagulation.

In this chapter, we demonstrate tissue removal by pulsed RF driven atmospheric pressure plasma irradiation. Pulsing conditions of duty ratio and frequency were controlled to investigate the effect on tissue removal rate, cut profile, and heat damage.

3.2.2. Method

Identical Experimental setup of our previous work with chlorine feedstock was employed. Pure argon of 500 sccm was used as a carrier gas for the experiment. Signal generator (N9310A, Agilent) generated 13.56 MHz RF pulse and continuous wave (CW). It was amplified with an amplifier (SMZ-100, IFI). Tissue surface temperature was measured with an IR thermometer. Bovine muscle was used to study tissue removal rate with various plasma condition. Porcine uterine tissue was employed for histology due to its sensitivity with a thin sheet of smooth muscle.

3.2.3. Result and Discussion

Figure 3-6 shows the forward and reflected powers of Pulsed RF waveform for the argon plasma jet (Delivered power = Forward power - Reflected power). Duty ratio of on and off time, and pulsing frequencies are the two parameters of pulsed RF. The power level of pulsed RF is higher than CW at the same total power operation (Level of delivered power x Duty ratio = Total power).

ES has only one source of heating tissue sample, ohmic heating ($P = I^2R$) by the current through tissue sample. Unlike ES, our plasma jet has additional source of heating, the hot plasma temperature. Pulsed RF periodically heat up and cool down the plasma as well as the tissue sample while CW continuously heat them up. During the on time of pulsed RF operation,

compared to the same power of CW operation larger power consumption of plasma generation leads to higher plasma density and larger number of reactive species in addition to higher removal rate of ES process. During the off time of pulsed RF operation, the plasma is killed, the number of reactive species is decreased, and ES process stops.

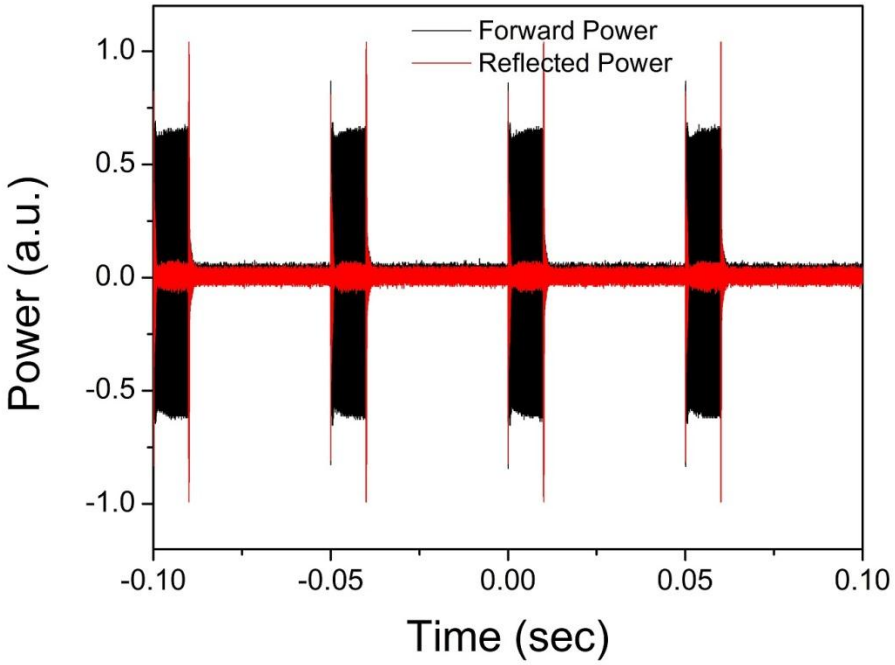

Figure 3-6 Forward and Reflected powers of 20 Hz and 20 % duty ratio pulsing of 13.56 MHz

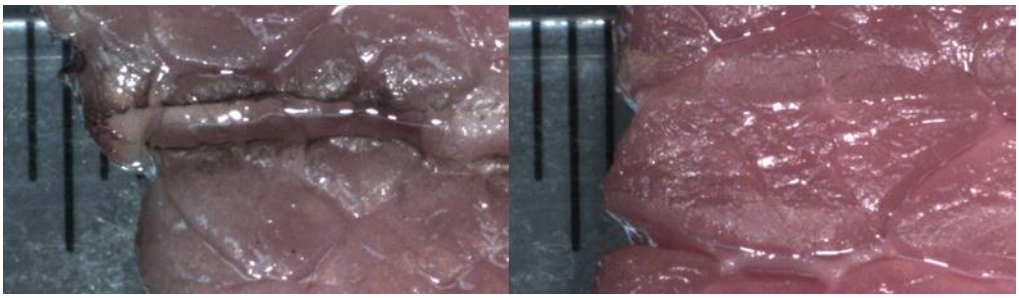

Figure 3-7 Top or plane view of tissue removal with a plasma jet under CW RF excitation (23 W) and pulsed RF (150 W, 30 Hz, and 15 %) conditions with constant average RF power. (Ruler is metric size with a 1 mm scale located behind tissue).

Tissue removal by Pulsed RF driven plasma-assisted non-contact ES was compared with CW. Power of CW and pulsed RF mode were 23 W and 150 W (30 Hz and 15 % duty ratio). Samples were scanned 25 mm long using a motorized linear stage at a rate of 10 mm $\cdot$ sec^{-1}. Interestingly, pulsed RF did not leave char or carbonized tissue on the remaining tissue while CW showed significant char formation. It is explained that heat damage on contiguous tissue is controllable with pulsing frequency and duty ratio. Note that pure ES use pulsed RF for coagulation mode that makes large heat damage on remaining tissue on purpose to stop bleeding. Pulsed RF also results in change of tissue removal rate or removal profile as seen in figure 3-7.

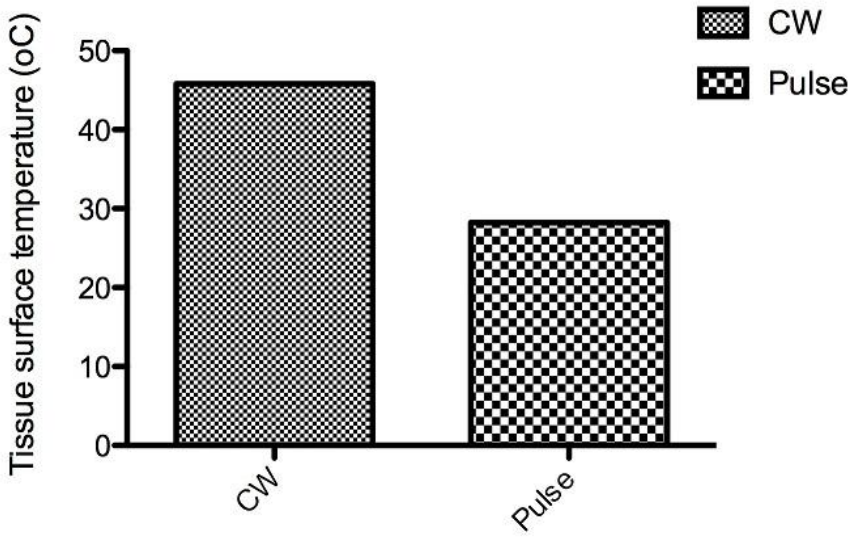

Figure 3-8 Tissue Surface temperatures during the experiment of figure 3-7.

Following to the observation of the char on the remaining tissue in figure 3-7, tissue surface temperature of CW and Pulsed RF was measured during tissue removal process. The tissue surface temperature of CW RF (45 ^{o}C) was higher than pulsed RF (28 ^{o}C). This result indicates that heat damage on remaining tissue may be larger with CW RF. It is supported by the observation of figure 3-7.

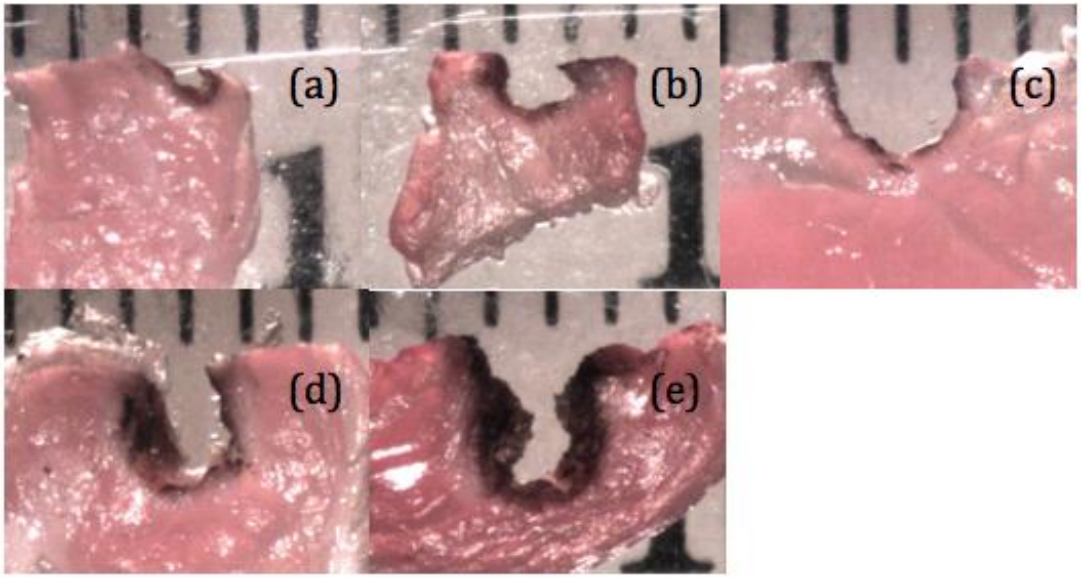

Figure 3-9 End view tissue removal profiles of pulsed RF 150 W, 30 Hz, and (a) 5 % (7.5 W) (b) 10 % (15 W) (c) 15 % (22.5 W) (d) 20 % (30.0 W) (e) 30 % (45.0 W) duty ratio.

Control of heat damage and removal rate by pulsing parameters was studied in figure 3-9 and 3-10. Figure 3-9 shows tissue removal profiles of pulsed RF mode with 5, 10, 15, 20, and 30 % of duty ratio. As duty ratio increase, total power increase by total power = set power (150 W) x duty ratio. The tissue removal rate (area) was proportional to the duty ratio of pulsed RF. However, heat damage on the remaining tissue significantly increased as duty ratio increased from 20 to 30 % while no noticeable change was observed with 5, 10, and 15 %. 15 % duty ratio is considered as the optimized duty ratio for high removal rate and minimal heat damage. It tells us that tissue removal mechanism changes to more thermal process at a certain duty ratio. Under our given condition (150 W and 30 Hz of pulsed 13.56 MHz RF), higher duty ratios may be useful for tissue coagulation. It is interesting because pure ES use lower duty ratios for better coagulation [5].

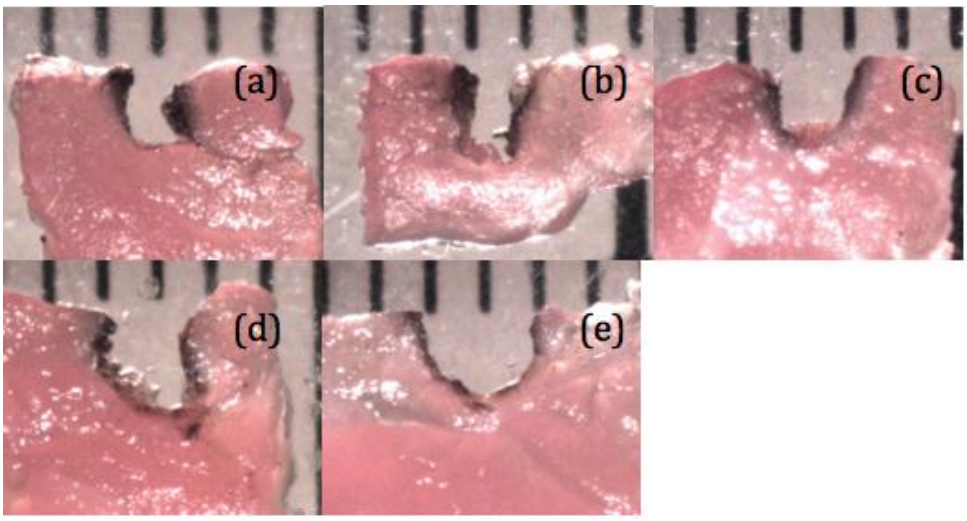

Figure 3-10 End view cuts obtained by Pulsed RF plasma at 150 W peak and fixed 15 % duty cycle for various repetition rates (a) 5 Hz, (b) 10 Hz, (c) 15 Hz, (d) 20 Hz and (e) 30 Hz.

In figure 3-10, increasing pulsing frequency from 5 to 30 Hz under given condition of pulsed RF (13.56 MHz, 150 W and 15 % duty ratio) resulted in higher tissue removal rate (larger removal area) but reduced heat damage on the remaining tissue. This data suggest that pulsing frequency is another parameter of simultaneous control for tissue removal rate and the heat damage.

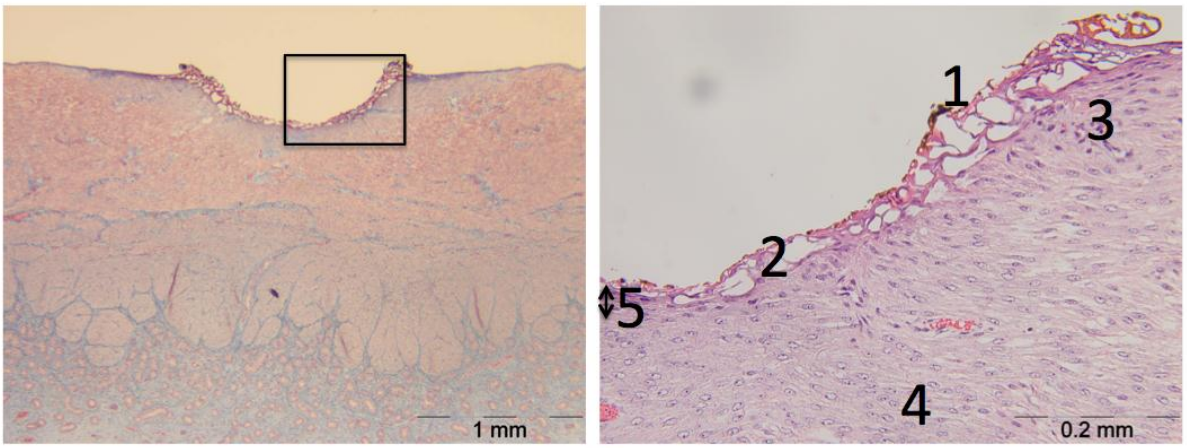

Figure 3-11 Histology slides displaying reduced collateral damage to contiguous uterine tissue irradiated by CW plasma jet.

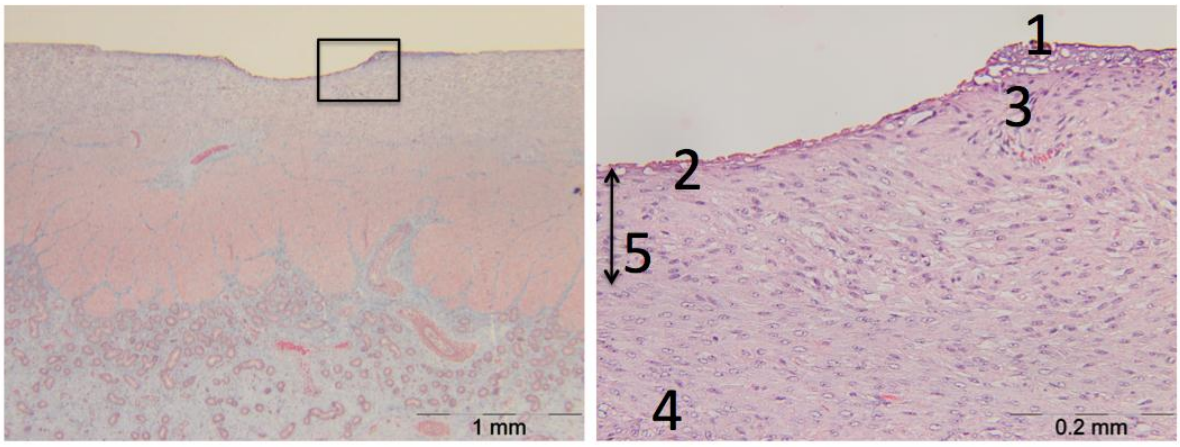

Figure 3-12 Histology slides of uterine tissue irradiated by pulsed RF plasma jet to further reduce thermal damage

Histology was employed to study tissue denaturation and cell damage. Figure 3-11 and 3-12 shows the histology samples irradiated by CW RF and pulsed RF plasma jet. Figure 3-11 (1) and 3-12 (1) are masson's trichrome stained tissue samples irradiated by CW RF plasma and pulsed RF plasma, respectively. And Figure 3-11 (2) and 3-12 (2) are H&E stained tissue samples irradiated by CW RF plasma and pulsed RF plasma, respectively. Masson's trichrome stained muscle fibers (cells) to red, cartilage to blue/green, heat damaged muscle fibers to dark brown. Hematoxylin in hematoxylin and eosin (H&E) colors nuclei of cells blue. The cytoplasm is a substance that consists of all of the contents outside of the nucleus of a membrane bound cell. It is stained by eosin in hematoxylin and eosin (H&E) in various shades of red, pink, and orange.

CW RF plasma showed different feature in those histology samples compared with pulsed RF plasma irradiation. It showed higher tissue removal rate as seen in figure 3-11 (1) (depth of 0.29 mm and width of 1.13 mm) compared with pulsed RF in figure 3-12 (1) (depth of 0.16 mm and width of 0.80 mm). Tissue denaturing was deeper as marked by arrow in figure 3-11 (1) (~0.25 mm) compared with pulsed RF in figure 3-12 (1) (~0.10 mm). More char formation

(dark/brown in masson's trichrome stained tissue) was observed on the remaining tissue in figure 3-11 (1). Spongy like necrotic layer of CW histology sample in figure 3-11 was thicker than pulsed RF. However, the dead nuclei of pulsed RF histology sample were observed in deeper location. Dead nuclei of muscle fibers or cells are elongated in comparison with round nuclei in unaffected healthy cells in H&E stained tissue (area 4 in figure 3-12 (2)). Yet it is not understood that the dead nuclei penetrated in the deeper area than denaturation. In short, CW RF plasma irradiation showed more tissue damage of denaturation, carbonization (charring), and thicker necrotic layer compared to pulsed RF plasma irradiation.

3.2.4. Conclusion

In this study, tissue removal in terms of removal profiles and heat damage was explored with pulse duty ratio and pulsing frequency of pulsed RF plasma irradiation. Higher tissue surface temperature of CW RF (45 ^{o}C) than pulsed RF (28 ^{o}C) supported larger heat damage on remaining tissue after CW RF plasma irradiation as seen in figure 2. Significantly increased char formation with 20 and 30 % duty ratio explains that tissue removal mechanism changes to more thermal process at a certain duty ratio. Increasing pulsing frequency from 5 to 30 Hz under given condition of pulsed RF resulted in higher tissue removal rate but reduced heat damage on the remaining tissue. Histology sample showed that pulsed RF plasma irradiation decreased removal rate but also reduced heat damage compared to CW. Therefore, plasma can be tailored by electrical parameters of pulsed RF as well as plasma chemistry for high removal rate and minimal heat damage.

In addition to the understanding above, more work to support the result in this chapter is required. For example, OES of plasma jet at various pulsed RF conditions will provide

information of the plasma temperature that may affect tissue removal and heat damage, reactive species that chemically affect tissue removal rate. Pulsed RF mode with chemical feedstocks such as CCl_4 may provide more control knob of tissue removal rate and heat damage on the remaining tissue.

REFERENCES

[1] I. G. Koo, C. A. Moore, M. Y. Choi, G. J. Kim, P. Y. Kim, Y. Kim, Z. Yu, and G. J. Collins, *Plasma Processes and polymers,* **2011**, 8, 1103.
[2] L. Bárdos, H. Baránková, *Thin Solid Films* **2010**, 518, 6705.
[3] G .A. Wyeth, *The endotherm. Am. J. Electrother. Radiol.* **1924**, 42, 186.
[4] D. J. Zinder, *Otolaryngol Head Neck Surg.* **2000**, 123,450.
[5] N. N. Massarweh, N. Cosgriff, D. P. Slakey, *J. Am. Coll. Surg.* **2006**, 202, 520.
[6] K. R. Stalder, J. Woloszko, *Contrib. Plasm. Phys.* **2007**, 47, 64.
[7] Michael A. Lieberman and Alan J. Lichtenberg, *Principles of Plasma Discharges and Materials Processing,* 2nd Edition, Wiley, New York **2005**.
[8] C. Tendero, C. Tixier, P. Tristant, J. Desmaison, P. Leprince, *Spectrochim. Acta B* **2006**, 61, 2.
[9] F. Iza, G. J. Kim, S. M. Lee, J. K. Lee, J. L. Walsh, Y. T. Zhang, M. G. Kong, *Plasma Process. Polym.* **2008**, 5, 322.
[10] A. Fridman, *Plasma Chemistry,* Cambridge Univ. Press, New York **2008**.
[11] F. Iza, G.J. Kim, S.M. Lee, J.K. Lee, J. L. Walsh, Y. T. Zhang and M.G. Kong, *Plasma Process. Polym.* **2008**, 5, 322.
[12] J. S. Sousa, G. Bauville, B. Lacour, V. Puech, M. Touzeau, *Eur. Phys. J. Appl. Phys.* **2009**, 47, 22807.
[13] J. S. Sousa, G. Bauville, B. Lacour, V. Puech, M. Touzeau, L. C. Pitchford, *Appl. Phys. Lett.* **2008**, 93, 011502.
[14] H. H. Chen, C. C. Weng, J. D. Liao, K. M. Chen, B. W. Hsu, *J. Phys. D: Appl. Phys.* **2009**, 42, 135201.
[15] Y. Yamagata, A. Sharma, J. Narayan, R. M. Mayo, J. W. Newman, K. Ebihara, *J. Appl. Phys.* **1999**, 86, 4154.
[16] Abhilasha and R. K. Thareja, *Phys. Lett. A*, **1993**, 184, 99-103.
[17] V. M. Donnelly, *J. Vac. Sci. Technol. A* **1996**, 14(3), 1076
[18] J. W. Milsom, B. Böhm, and K. Nakajima, *Laparoscopic Colorectal Surgery,* 2nd Edition, Springer, New York **2006**.
[19] R. W. B. Pearse, A. G. Gaydon, *The Identification of Molecular Spectra*, 2nd Edition, John Wiley & Sons INC., New York **1950**.
[20] J. T. Verdeyen, J. Beberman, and L. Overzet, *J. Vac. Sci. Technol. A, Vac. Surf. Films* **1990**, 8, 1851.
[21] C. Grabowski and J. M. Gahl, *J. Appl. Phys*. **1991**, 70, 1039.
[22] L. J. Overzet, Y. Lin, and L. Luo, *J. Appl. Phys*. **1992**, 72, 5579.
[23] S. K. Kanakasabapathy, L. J. Overzet, V. Midha, and D. Economou, *Appl. Phys. Lett*. **2001**, 78, 22.
[24] S. Samukawa and S. Furuoya, *Appl. Phys. Lett*. **1993**, 63, 2044.
[25] S. Samukawa and K. Terada, *J. Vac. Sci. Technol. B, Microelectron. Process. Phenom.* **1994**, 12, 3300.
[26] H. Ohtake and S. Samukawa, *Appl. Phys. Lett.* **1996**, 68, 2416.
[27] T. H. Ahn, K. Nakamura, and H. Sugai, *Plasma Sources Sci. Technol.* **1996**, 5, 139.
[28] S. Samukawa and T. Mieno, *Plasma Sources Sci. Technol.* **1996**, 5, 132.
[29] A. Yokozawa, H. Ohtake, and S. Samukawa, *Jpn. J. Appl. Phys.* **1996**, 35, 2433.
[30] S. Samukawa, *Appl. Phys. Lett.* **1996**, 68, 316.

[31] T. Mukai, H. Hada, S. Tahara, H. Yoda, and S. Samukawa, *Jpn. J. Appl. Phys.* **2006**, 45, 5542.
[32] T. Mukai, N. Ohshima, H. Hada, and S. Samukawa, *J. Vac. Sci. Technol. A, Vac. Surf. Films* **2007**, 25, 432.

CHAPTER 4. HELIUM/H_2O_2 ATMOSPHERIC PRESSURE PLASMA-ASSISTED ELECTROSURGERY

Electrosurgery (ES) is widely used by surgeons to dissect tissue and control bleeding. Electrosurgical devices achieve these effects through resistive heating of tissue that vaporizes cellular fluid to rupture cells and denatures proteins to produce a hemostatic coagulum. We demonstrate RF driven plasma assisted ES. OH rich helium plasma jet was generated with H_2O_2 entrained in the feedstock gas. The powered electrode of a 13.56 MHz atmospheric pressure plasma jet was employed in contact with tissue samples to vaporize or ablate tissue. In effect, monopolar ES was combined with plasma. We report both significantly higher tissue removal rate and lower electrical current flow through the tissue sample with plasma-assisted ablation compared to conventional electrosurgical ablation at the same generator output power [1].

4.1. Introduction

Electricity has been used by surgeons to cut and coagulate tissues since the 1920s. Today, electrosurgery (ES) is one of the most common surgical techniques because the incisions can be performed faster with less blood loss compared to incisions made with a scalpel. A variety of surgical procedures employ ES including laparascopy [2], arthroscopy [3], otolaryngology [4], and spine and cosmetic surgery [5-7]. In monopolar ES, high frequency electrical current is delivered to the tissue through an active electrode and returned to the generator through a dispersive electrode or pad to complete the circuit. The concentrated current density at the active electrode tip generates Joule heat, vaporizing intracellular water and rupturing cells, resulting in dissection.

Complications have been reported in ES, particularly with monopolar delivery. If the current is not sufficiently dispersed at the return pad, the energy may become focused in one area causing a burn. If the patient is improperly grounded, the current may follow an alternate ground path potentially leading to alternate-site burns to the patient or the surgeon [8]. The surgical effects of ES are based on heat hence there is inherent risk of thermal tissue injury. Thermal spread may damage vasculature, nerves, and other vital structures leading to delayed wound healing and increased postoperative pain [9]. Therefore, ES devices are faced with the challenge of hemostatic cutting with minimal tissue injury.

Monopolar ES can be augmented by adding argon gas flow in line with the active electrode. The resulting conductive plasma stream allows the current to arc from the electrode to the tissue without contact for hemostasis and tissue removal by vaporization, i.e., ablation. Recently we reported enhancement of non-contact tissue ablation by an RF-excited argon plasma jet through addition of chemical precursors to the argon stream [10]. Our current work was driven by the hypothesis that plasma chemical reactions could act synergistically with ES processes during monopolar, contact mode tissue ablation. A synergistic effect would mean that less power and therefore less Joule heat may be required for tissue ablation, eventually leading to less thermal injury. In this chapter, we report tissue ablation with a coaxial type helium/H_2O_2 plasma using a 13.56 MHz-powered electrode to deliver both plasma chemistry and electrical energy to the tissue sample.

4.2. Experimental Section

4.2.1. Atmospheric Pressure Plasma Generation

Figure 4-1 shows the coaxial plasma setup. The inner powered electrode consisted of an aluminum rod with a diameter of 3.1 mm. The outer grounded electrode consisted of an

aluminum cylinder with inner and outer diameters of 5.6 and 6.3 mm, respectively. The powered electrode protruded 3 mm from the end of the grounded electrode. The powered electrode and inside wall of the grounded electrode were anodized with 16 and 40 μm thick nanoporous Al_2O_3, respectively.

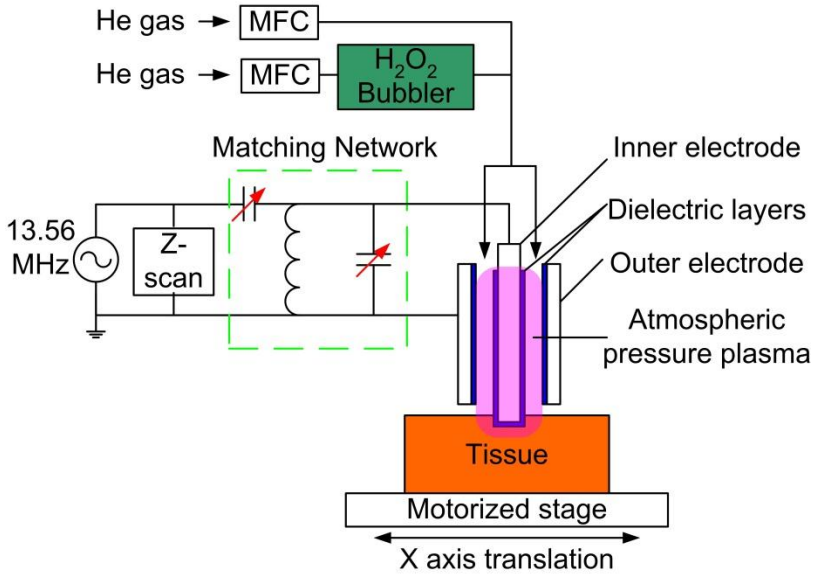

Figure 4-1 Schematic of CSU designed coaxial plasma experimental setup

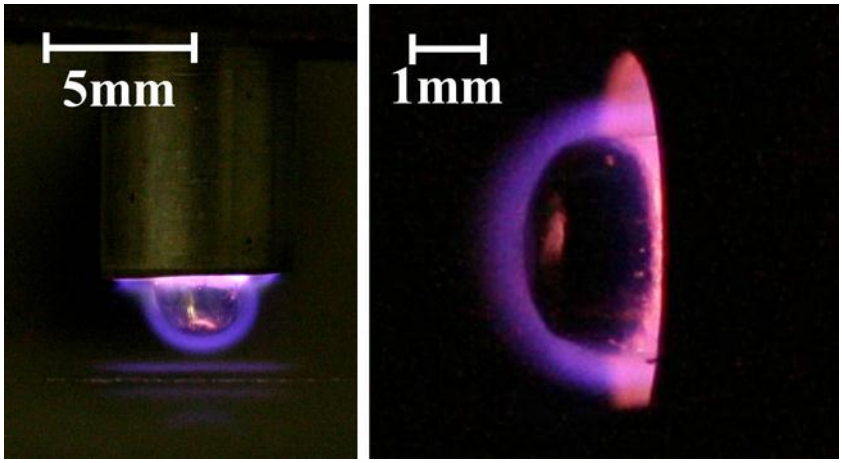

Figure 4-2 Images of the CSU plasma discharge (47 W, 1000 sccm helium, 16 μl · min^{-1} H_2O_2).

Plasma was generated in the annulus as shown in Figure 4-2, driven by 13.56 MHz RF power provided by a signal generator (N9310A, Agilent) and amplifier (SMZ-100, IFI). Helium was used as the discharge gas and the concentration of H_2O_2 in the plasma volume was controlled by adjusting helium gas flow through the H_2O_2 bubbler. The total helium flow rate was fixed at 600 sccm for optical emission spectroscopy and 1000 sccm for all other studies by adding bypass flow to the flow through the bubbler.

4.2.2. Mechanical and Electrochemical Process for Electrodes Preparation

The aluminum electrodes were first polished with sandpaper. To achieve further polishing, electrochemical process were used. Then the electrode was anodized, oxidizing the aluminum surface, to build nonoporous dielectric layer also by the similar electrochemical process. The schematic of the electro-polishing and anodization is shown in figure 4-3.

Perchloric acid ($HClO_4$) and ethanol (C_2H_5OH) of 1:7 volume % mixtures were employed as electrolyte to dissolve the aluminum on the surface. Since the electrochemical reaction rate is higher at sharp edges due to the more intensive electric field to attract charged ions in the electrolyte, the surface become smooth in nanometer dimension. The voltage applied was 20 V and the resulting current was 1.62 A at that condition. All of the electrodes were electro-polished for 3 minutes. Magnetic stirrer rotated the stirring bar to prevent local concentration difference of electrolytes caused by the byproduct of the electrochemical reaction.

Anodizing employed 0.3 M of $H_2C_2O_4$, oxalic acid, as the electrolyte. In both of electro-polishing and anodization process, the electrolyte temperature was kept at 4 ^oC by cooling the double jacket beaker. 10 V was applied and resulting current was 8~10 mA depending on the operation time. This process naturally built 4 μm nanoporous alumina (Al_2O_3) dielectric in an

hour. SEM image of the nanoporous dielectric layer is shown in figure 4-4. Therefore, the inner powered electrode was anodized for 4 hours to build 16 µm dielectric layer, and the outer grounded electrode for 10 hours to build 40 µm dielectric layers.

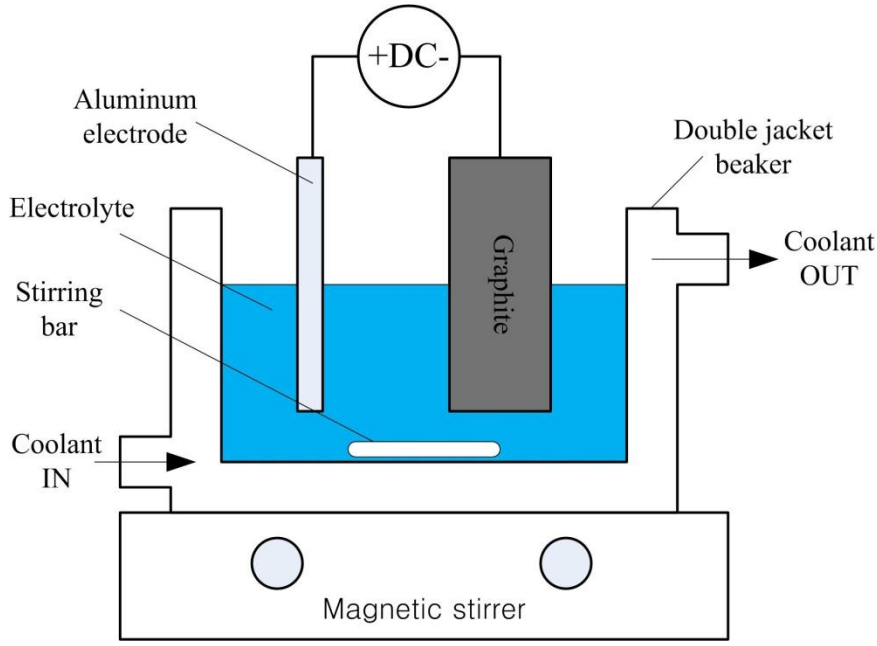

Figure 4-3 Experimental setup of electrochemical process for electro-polishing and anodization of electrodes employed in CSU plasma designs

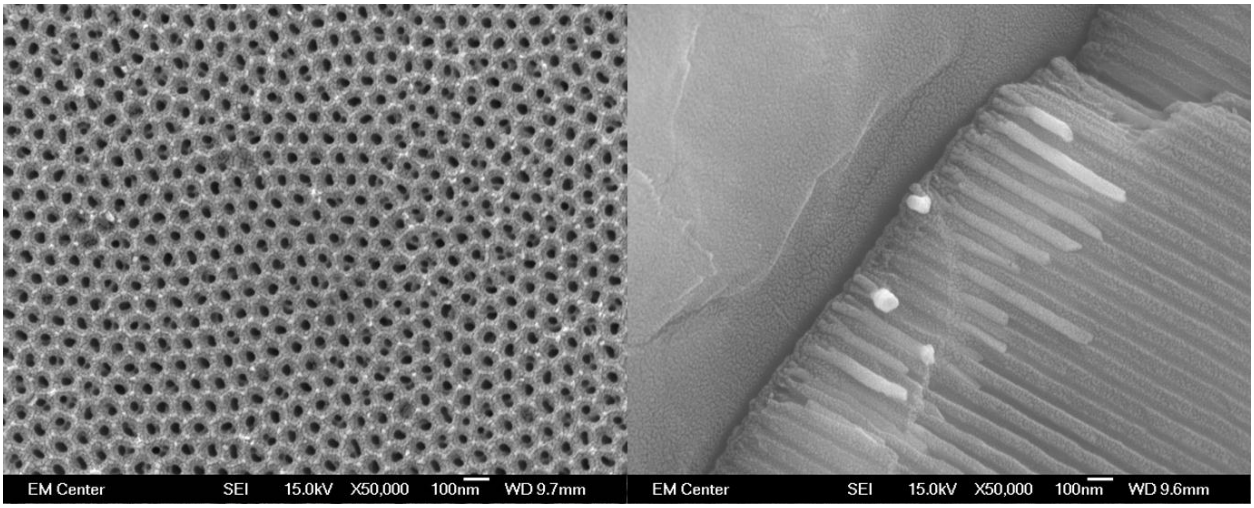

Figure 4-4 Illustrative nanoporous structure of Al_2O_3 dielectric layer built by electrochemical anodization.

4.2.3. Spectroscopic Diagnosis

The light emitted from the whole discharge region was delivered to a monochromator (SpectroPro® -2750, Princeton Instruments) coupled to a CCD camera (PIXIS-2K, Princeton Instruments) through a UV grade quartz focusing lens and an optical fiber. Absolute calibrations of the spectra were made using radiance standards including a calibrated mercury-argon lamp (HG-1, Ocean Optics). The spectra were normalized to the emission intensity of helium at 706 nm.

4.2.4. Electrical Characteristics Analysis

The plasma generating electrical system was controlled with careful measurement of forward, reflected, and delivered power, impedance, voltage, and current using a Z-scan (Advanced Energy) between the power supply and matching network. The voltages across the ES and plasma electrodes were measured with a high voltage probe (PPE6KV, Lecroy). The currents through the electrodes and the tissue samples were measured using a current transformer (CT-B2.5, Bergoz). The sample holder for measuring current through the tissue was made of copper metal and connected to the grounded electrode.

4.2.5. Tissue Preparation, Ablation, and Characterization

Prepackaged retail chicken breast muscle portions were used to prepare samples approximately 2 cm × 2.5 cm in area, 1 cm in thickness, weighing 5 ± 1 g. Samples were placed on a stage at a fixed distance to form a 1 mm gap between the tissue and the grounded electrode when the protruding powered electrode was pressed into the tissue. Samples were scanned 25 mm long at 47 W RF power using a motorized linear stage at a rate of 10 mm $\cdot$ sec^{-1}. A Force

FXTM Electrosurgical Generator (Valleylab, Covidien) was employed for comparison with plasma. The ES electrode (E1550, Valleylab, Covidien) was selected on the basis of similar shape and tissue contact area to the plasma electrode. Samples were scanned by the ES electrode at 47 W similarly as described above for plasma. In both cases, the samples were weighed immediately before and after treatment using an analytical balance to determine the mass of removed tissue. Data are expressed as the mean ± SEM of 10 samples. Statistical analysis was performed using Student's t-test.

Following ablation by plasma or ES, samples were fixed in formalin, embedded in paraffin, serially sectioned, and stained with hematoxylin and eosin. The histological sections were examined with an Olympus BX52 light microscope and images were obtained with an Olympus DP70 digital camera.

Changes in the chemical composition of the tissue surface were determined by Fourier transform infrared (FTIR) spectroscopy. The samples were scanned 25 times at 4 cm^{-1} resolution using a single bounce Smart ITR for ATR (Attenuated Total Reflectance) with the FTIR system (Nicolet 6700, Thermofisher).

4.3. Results and Discussion

4.3.1. Generation and Characterization of Atmospheric Pressure Helium/H_2O_2

Below 20 W, plasma discharge appeared to be homogeneous over the annular space between the electrodes. Discharge intensity increased with increasing power. Above 20 W, the discharge began to transition from α to γ mode producing strong emission in a semicircular region in addition to uniform and weak emission throughout the annulus. This transition from α to γ mode at 20 W was confirmed by measuring voltage and current as shown in Figure 4-5. In α mode,

voltage and current increase as power increases. At 20 W, the voltage dropped and the discharge volume shrank resulting in γ mode, characterized by constant voltage and increasing current as power increases [11]. In addition, the glow plasma extended out around the protruding powered electrode with power over 20 W.

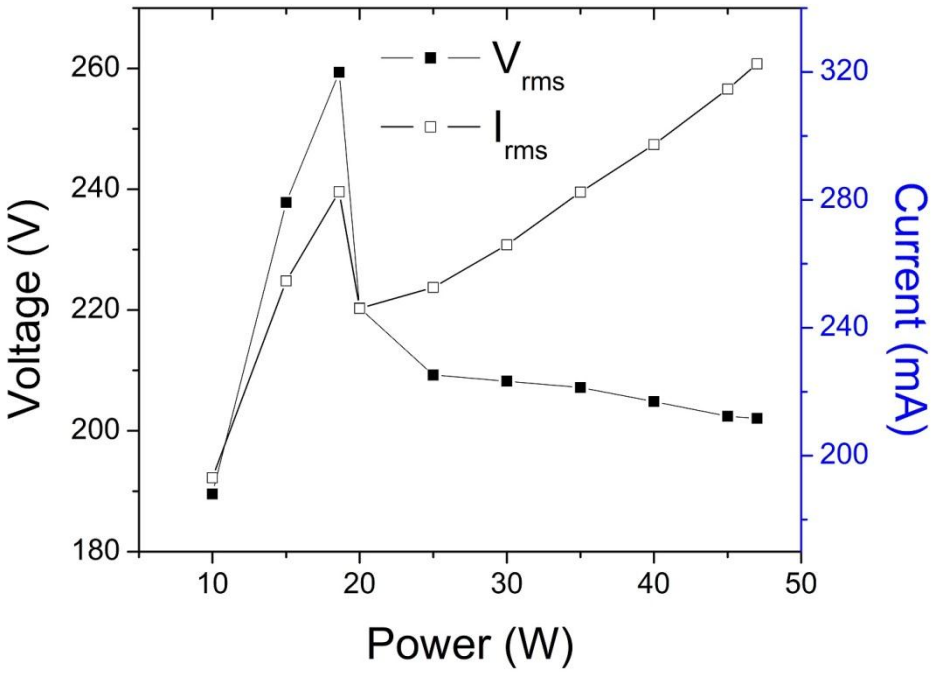

Figure 4-5 RF voltage and current measurements vs. applied RF power to a helium/H_2O_2 coaxial plasma (47 W, 1000 sccm helium, 16 µl · min^{-1} H_2O_2).

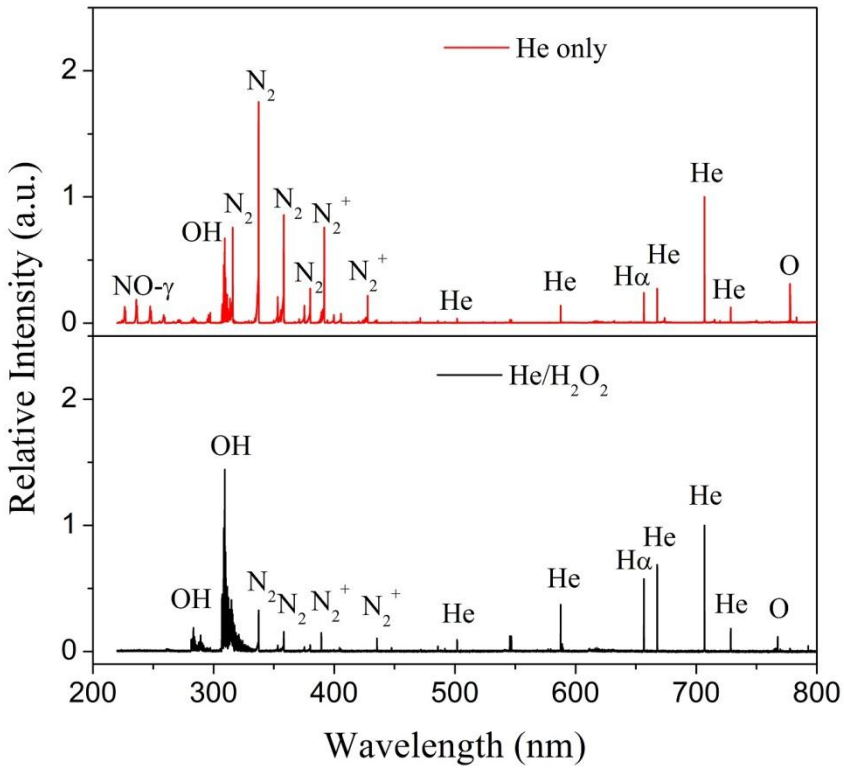

Figure 4-6 Typical optical emission spectra of open air pure helium feedstock flow and helium/H_2O_2 feedstock flow for exciting plasma discharges (47 W, 600 sccm helium, 7 µl · min^{-1} H_2O_2).

Figure 4-6 shows representative optical emission spectra from helium and helium/H_2O_2 plasmas. The intensity of the OH band between 306 and 310 nm was increased in the emission spectrum of helium/H_2O_2 plasma compared to helium plasma under identical power and helium flow. This clearly demonstrates that H_2O_2 addition enhances OH radical generation. Helium plasma temperature, both with and without H_2O_2 addition, analyzed from emission spectrum was approximately 500 ± 50 K (230 ± 50 ^{o}C). Plasma electrode temperature measured by thermal IR camera was 210 ^{o}C.

4.3.2. Tissue Removal by Coaxial Plasma

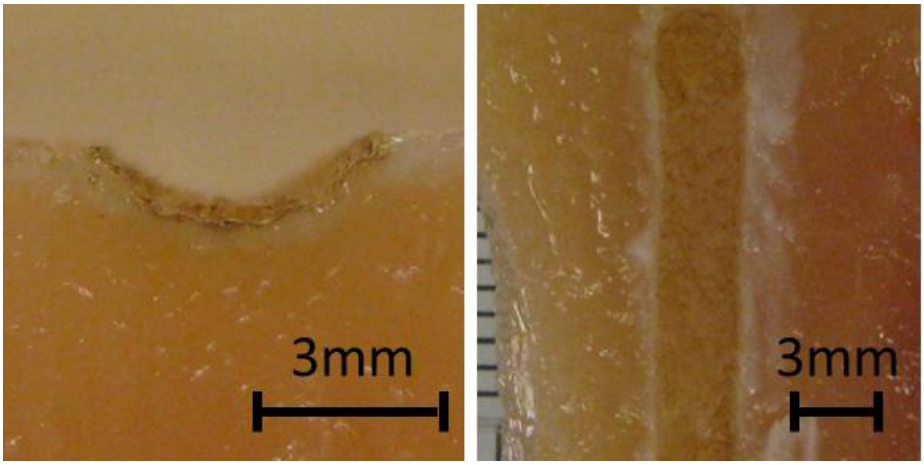

Figure 4-7 End and plane view of a chicken breast tissue sample treated by helium/H_2O_2 coaxial plasma (47 W, 1000 sccm helium, 16 µl · min^{-1} H_2O_2, 10 mm · sec^{-1} treatment speed).

When the powered electrode touched the tissue sample, the tissue acted as a ground path for electrical current, resulting in microdischarges between the electrode and the tissue surface. Hence in contact mode, this coaxial plasma combined plasma chemistry with RF voltage-driven discharges similar to the sparks observed in ES cutting. To better understand the effect of plasma chemistry in tissue ablation, helium plasma without H_2O_2 (47 W, 1000 sccm helium) was applied to the tissue sample. The powered electrode immediately adhered to the tissue on contact and tissue ablation could not be achieved by translation of the motorized stage. In contrast, when the helium plasma was applied to the tissue sample under the same conditions but with the addition of 16 µl · min^{-1} H_2O_2, there was minimal adhesion and the tissue sample was ablated linearly using the motorized stage as shown in Figure 4-7. Although the plasma and electrode temperatures did not differ between helium and helium/H_2O_2 plasmas

4.3.3. FTIR Analysis of Treated Tissue

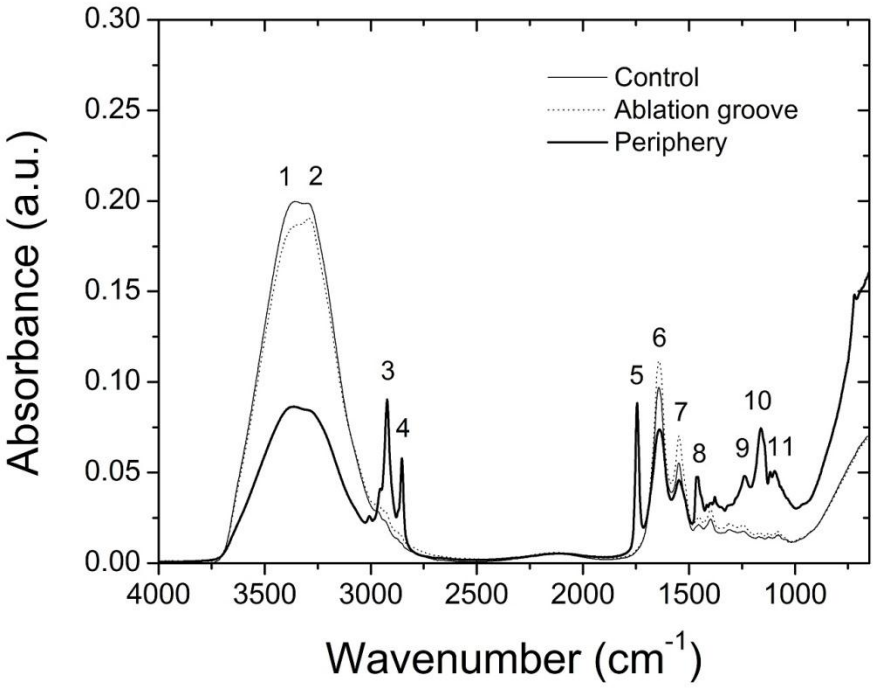

Figure 4-8 FTIR spectra of the surface bonds in tissue samples treated by helium/H_2O_2 coaxial plasma (47 W, 1000 sccm helium, 16 µl · min^{-1} H_2O_2, 10 mm · sec^{-1} treatment speed) taken from areas inside the ablation groove (green) and from the immediate periphery compared to untreated tissue sample.

Figure 4-8 shows representative FTIR spectra of control and helium/H_2O_2 plasma-treated tissues taken from areas inside the ablation groove and from the immediate periphery. A number of differences in the spectra are apparent in the periphery of the ablation groove as follows. Decreases in the relative intensities of bands assigned to amide A (3339 cm^{-1}), amide I (1658 cm^{-1}) and amide II (1540 cm^{-1}) indicate a loss of protein secondary structure [11, 12]. This protein denaturation was accompanied by considerable increases in the relative intensities of CH_2 (2923, 2853 and 1451 cm^{-1}) and C=O (1727-1720 cm^{-1}) stretch assigned, respectively, to methylene and ester functional groups in lipids [12, 13]. In addition, new peaks assigned to PO_2 (1236 and 1080 cm^{-1}) and C-O-C (1170 cm^{-1}) stretch appear in the spectrum, which can be attributed primarily to

nucleic acids and glycogen [14]. Interestingly, the spectrum of tissue inside the ablation groove did not differ markedly from control tissue. These results may be explained by the rupture of lipid membranes and forceful ejection of intracellular contents to the periphery as cells are vaporized during plasma treatment.

4.3.4. Comparison with Electrosurgery

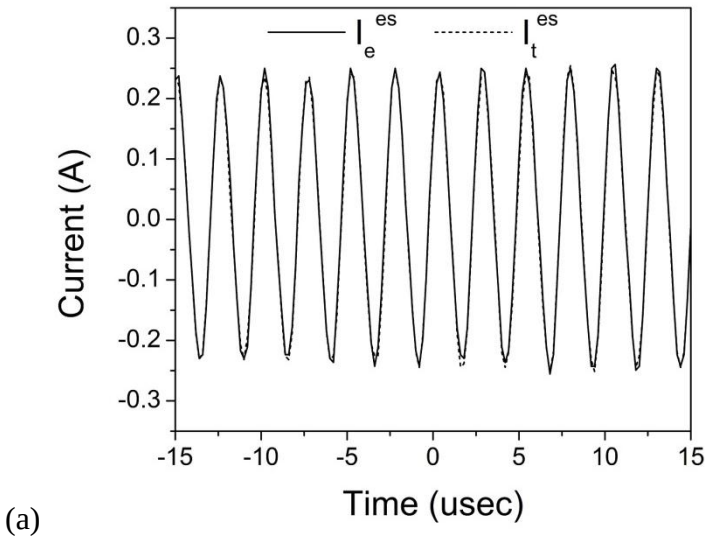

(a)

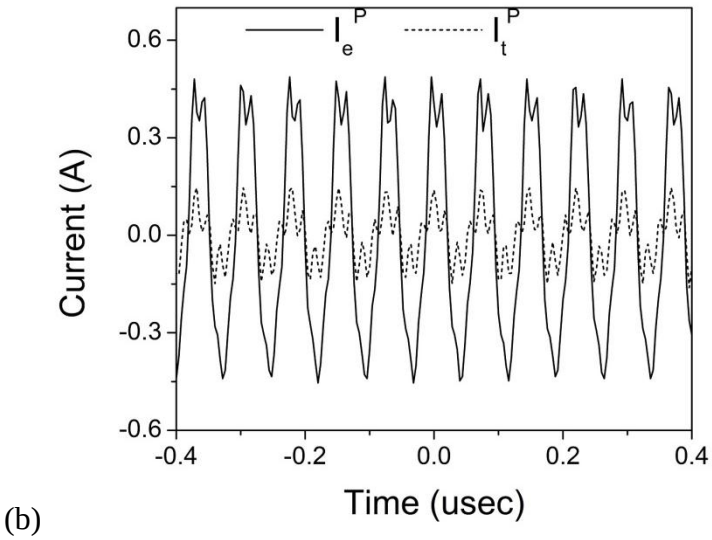

(b)

Figure 4-9 Electrical current flow through the active electrodes (Ie) and tissue samples (It) during (a) ES ablation and (b) plasma ablation.

To compare plasma ablation to ES ablation under similar conditions (47 W, 10 mm · sec^{-1} treatment speed), an ES generator was employed with output current set to "cut" mode. The electrical current flow through the active electrodes and tissue samples during electrode-tissue contact are shown in Figure 4-9. The current through the tissue sample during ES ablation (I_t^{es} = 167.2 mA) was nearly equal to the current through the electrode (I_e^{es} = 168.0 mA). During plasma ablation, the current flow through the tissue sample (I_t^{p} = 79.6 mA) was significantly lower than the current flow through the electrode (I_e^{p} = 322.8 mA). A large portion of the delivered power was apparently consumed in the process of plasma generation.

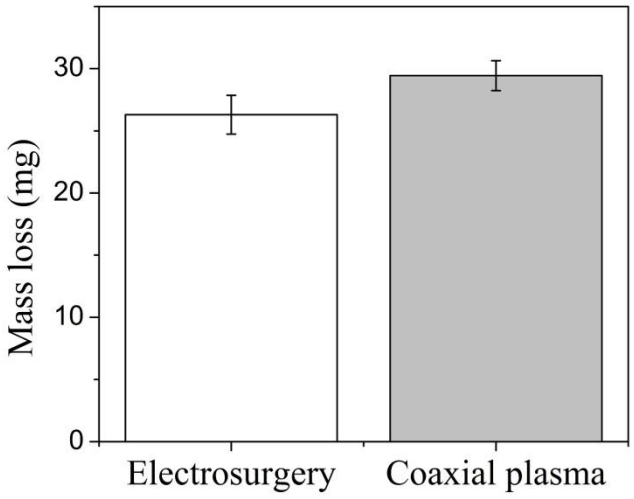

Figure 4-10 Tissue mass loss after 25 mm long ablation by ES (cut mode) and helium/H_2O_2 coaxial plasma (1000 sccm helium, 16 µl · min^{-1} H_2O_2), both at 47 W and 10 mm · sec^{-1} treatment speed.

Since the current flow through the tissue sample with ES was approximately twofold higher ($I_t^{es} \approx 2\ I_t^{p}$) than with plasma, the Joule heat generated in the tissue (P_t) was approximately fourfold greater ($P_t^{es} \approx 4\ P_t^{p}$). After accounting for tissue mass loss due to water evaporation induced by gas flow (5.16 ± 0.71 mg), the mass removed with plasma (29.44 ± 1.2 mg) and ES

(26.3 ± 1.56 mg) in a 25 mm scan of the tissue sample were comparable (Figure 4-10). This data suggest that in addition to ES thermal ablation mechanisms based on Joule heat, plasma may provide other pathways for tissue removal. Histological sections of hematoxylin and eosin-stained tissue samples after ES and helium/H_2O_2 plasma ablation showed that in both cases, the ablated surface is characterized by a layer of amorphous eosinophilic material with minimal carbonization or charring (Figure 4-11). However, histological sections of masson's trichrome-stained tissue samples showed heat damage (dark/brown color) under the necrotic layer after ES while there was no such a damage under the necrotic layer after helium/H_2O_2 plasma ablation.

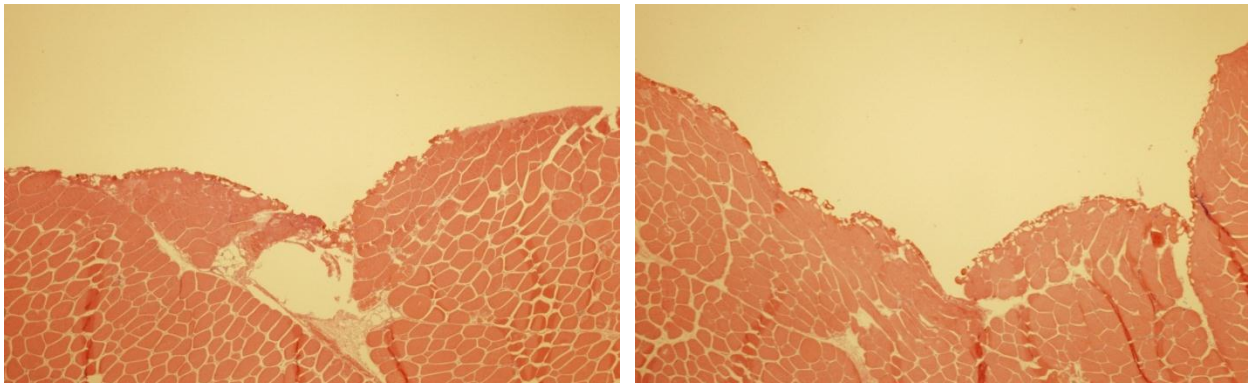

(a) (b)

Figure 4-11 Histological sections of hematoxylin and eosin-stained tissue samples after treatment by (a) ES (cut mode) and (b) helium/ H_2O_2 plasma (1000 sccm helium, 16 µl · min^{-1} H_2O_2), both at 47 W and 10 mm · sec^{-1} treatment speed.

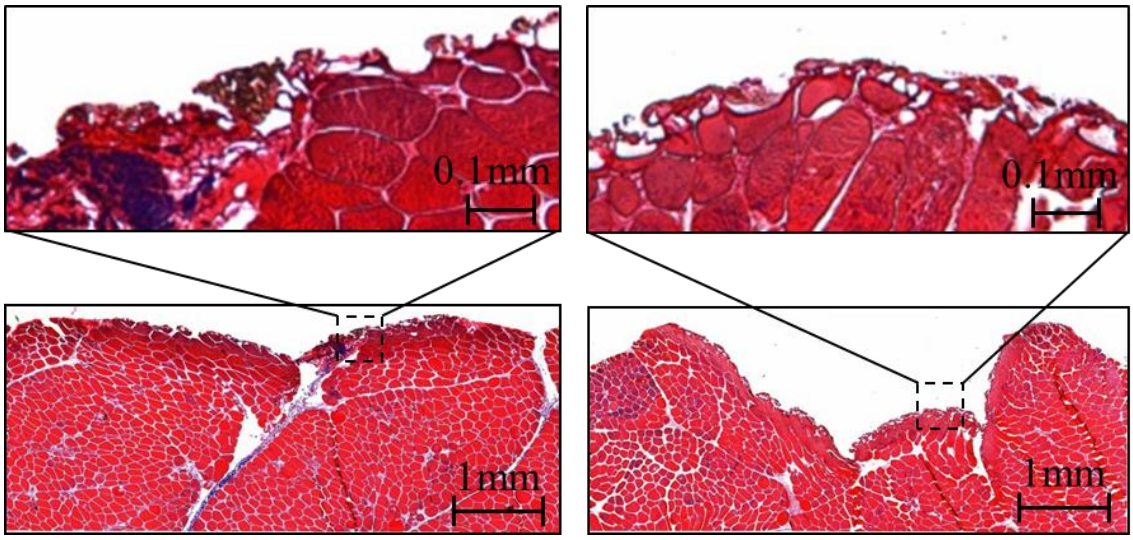

(a) (b)

Figure 4-12 Histological sections of masson's trichrome-stained tissue samples after treatment by (a) ES (cut mode) and (b) helium/H_2O_2 plasma (1000 sccm helium, 16 µl · min^{-1} H_2O_2), both at 47 W and 10 mm · sec^{-1} treatment speed.

4.4. Conclusions

In summary, γ mode discharge of RF plasma was employed as a monopolar contact electrode to enhance ES ablation. The addition of H_2O_2 into the helium plasma was found to increase the concentration of chemically reactive OH species (Figure 4-6). This eliminated tissue adhesion to the powered electrode through an as yet undetermined mechanism. Although the helium and helium/H_2O_2 plasma, and electrode temperatures did not differ, tissue ablation only occurred with the addition of H_2O_2 under our experimental conditions. At 47 W input power, helium/H_2O_2 plasma removed tissue at a rate comparable to ES, but with less electrical current flow through the tissue. Taken together, these results suggest a possible role of plasma chemistry in the ablation process that may allow for desired surgical effects at lower power and lead to decreased risk of thermal injury and other adverse effects of electrical current flow through a patient.

REFERENCES

[1] Myeong Yeol Choi, Il Gyo Koo, Paul Y. Kim, Sung Kil Kang, Yoon-Sun Kim, Jae-Chul Jung, George J. Collins, *Plasma Processes and Polymers*, **2012**, 9, 1015.
[2] M.-P. Wu, C.-S. Ou, S.-L. Chen, E.Y.T. Yen, R. Rowbotham, *Am. J. Surg.* **2000**, 179, 67.
[3] J. D. Polousky, T. P. Hedman, C. T. Vangsness, *Jr. Arthroscopy* **2000**, 16, 813.
[4] J. Woloszko, M. Kwende, K. R. Stalder, *Proc. SPIE* **2003**, 4949, 341.
[5] E. W. Elliott-Lewis, J. Jolette, J. Ramos, *Neurosurgery* **2010**, 67, 166.
[6] A. J. Burns, S. G. Holden, *Lasers Surg. Med.* **2006**, 38, 575.
[7] E. P. Tierney, C. W. Hanke, *Dermatol. Surg.* **2009**, 35, 1324.
[8] N. N. Massarweh, N. Cosgriff, D. P. Slakey, *J. Am. Coll. Surg.* **2006**, 202, 520.
[9] M. K. Flynn, A. C. Weidner, C. L. Amundsen, *Am. J. Obstet. Gynecol.* **2006**, 195, 1869.
[10] I. G. Koo, C. A. Moore, M. Y. Choi, G. J. Kim, P. Y. Kim, Y.S. Kim, Z. Yu, G. J. Collins, *Plasma Process. Polym.* **2011**, 8, 1103.
[11] S. Y. Moon, J. K. Rhee, D. B. Kim, and W. Choe, *Appl. Phys. Lett.* **2006**, 13, 033502.
[12] H. Susi, D. M. Byler, *Methods Enzymol.* **1986**, 130, 290.
[13] S. Krimm, J. Bandekar, *Adv. Protein Chem.* **1986**, 38, 181.
[14] O. Bozkurt, M. D. Bilgin, F. Severcan, *Spectroscopy* **2007**, 21, 151.

CHAPTER 5. HE-H_2O_2 PLASMA JET IRRADIATION OF TISSUE SURFACES: STUDY OF CHANGING SURFACE MOLECULAR BONDS, EFFLUENT CHEMISTRY, REACTIVE RADICALS AND INSIGHTS INTO DOMINANT PLASMA CHEMICAL TISSUE REMOVAL PATHWAYS

The major surface tissue removal mechanisms, resulting from atmospheric He-H_2O_2 plasma fluxes impinging on tissue surfaces, were investigated. We employed primarily optical emission for cataloging reactive plasma radicals and FTIR molecular spectroscopy to track molecular bond alterations at tissue surfaces. The volatilized tissue fragments, remaining solid phase tissue samples as well as non-processed contiguous tissue regions were all compared. The relative amounts of reactive plasma chemicals generated in the plasma were then correlated with measured tissue removal rates under varying experimental conditions. In addition plasma enhanced electrosurgery (ES) with additional reactive radical fluxes on tissue surfaces was compared to conventional electrosurgery (ES) with no added plasma irradiation. This study provides evidence that OH radicals drive the observed changes on tissue surfaces both within, and in bordering tissue regions. Moreover, plasma assisted ES as compared to pure ES reduces buildup of tissue char on ES electrodes. FTIR measurement of the surgical margins (surrounding the removed tissue) is possible in pure plasma tissue removal, via changes in amide A bonds, because plasma assisted ES does not destroy these indicators of reduced thermal damage, as does pure ES methods [1].

5.1. Introduction

Energy based tissue removal processes are possible replacements for cold steel scalpel tissue removal. Laser generated photon beams, supersonic beam flows of fine grits, and electrical

energy delivered by a sharp RF driven electrode (electrosurgery or ES) as well as ultrasonic energy delivery are the most common tissue removal techniques. All the energy based techniques vaporize water in the tissue cells, thereby removing unwanted tissue and offering faster dissection than cold steel scalpels. In addition the controlled high temperatures in the heated regions also provide coagulation conditions with minimal blood loss of surrounding tissue.

Commercial electrosurgical (ES) procedures employ AC currents from 500 to 3,000 kHz. This choice avoids neuromuscular stimulation, which occurs at electrical currents below 10,000 Hz [14]. Wave shape tailored ES current offers controlled relative levels of hemostasis and tissue removal.

High-intensity focused ultrasound (HIFU) [10] and associated viscous heating is also being used as an effective noninvasive procedure to remove undesired tissue such as ectopic foci alteration electrical pathways in the heart, or for achieving hemostasis in limb or organ traumas to reduce blood loss.[11-12] Focused phase array HIFU can be administered outside the body to reach spatially selected hemorrhagic areas inside the body in specific spatial locations.

Ohmic and ultra sound heating, while employing differing root heat mechanisms, both cause undesired lateral heat damage to contiguous tissue [2-9]. The heat generated in the incision site flows through contiguous tissue and denatures protein in the lateral tissue leading to undesired vascular constriction [13] If heat fluxes are not well controlled this can lead to thermal damage to nearby vital structures [15], delayed wound healing as a result of compromised blood circulation [16] as well as increased postoperative pain caused by sensory nerve injury during electrosurgery [17]. These disadvantages of heat driven surgical mean, lead us to consider employing low temperature atmospheric torches to deliver radical chemical energy to tissue to achieve tissue

removal, with reduced thermal damage, but still maintain practical tissue removal rates by gasifying tissue ingredients via plasma chemistry rather than by physical boiling.

Plasma has long been employed for surface modifications of polymers [18] and semiconductor etching of patterns on inorganic material surfaces [19]. Atmospheric plasma discharges, operating in open air are especially suitable to medical use, such as for achieving sterilization of bacteria and biofilms on tissue, without structural damage to underlying human skin [20, 21].

Our prior works have shown that one could generate controlled levels of reactive OH radicals to cause tissue (chicken breast) removal, by adding controlled hydrogen peroxide feedstock into an atmospheric pressure helium plasma jet surgical device driven by a 13.56 MHz radio frequency power supply [22]. The plasma jet dissociated H_2O_2 and emitted a spatially confined beam of OH radicals Tissue removal rates were comparable to conventional tissue removal by commercial ES devices. However plasma chemical pathways for tissue removal were left undetermined and are the object of this research.

Atomic and molecular spectroscopies are employed herein to unravel the relative contributions of OH species as compared to other possible mechanisms for driving tissue removal in plasma assisted surgery. Optical emission and absorption spectroscopy allow for monitoring of relative radical densities in the plasma plume impinging on tissue surfaces, under varying experimental conditions for both plasma-assisted ES and pure ES surgery. We show that the measured OH density tracks the measured tissue removal rate for plasma assisted ES but not for pure ES. We also determine herein, that the chemical bonds of both the plasma assisted ES irradiated tissue and the volatilized tissue gases emitted after He-H_2O_2 coaxial plasma tissue exposure are all distinct from each other. Tissue mass before and after coaxial plasma jet

irradiation of tissue samples was measured and we found that and tissue removal correlates with OH fluxes, as detailed in Results and Discussion sections below. Fourier Transformed Infra-Red (FT-IR) spectroscopy was employed to analyze both tissue particles collected from the particles entrained in gaseous effluent gases by means of micro filters. We also used FTIR analysis to examine remaining solid tissue surfaces in and around the tissue removal sites after plasma jet irradiation. That is small tissue particles entrained in gas effluent as well as remaining un-volatized under layers of tissue surfaces, following tissue gasification by plasma chemical reactions, were characterized by FTIR. As a baseline for comparison, we employed conventional electrosurgical tissue removal under similar total input energy conditions. Distinct and unique amide bonds of tissue proteins were observed on small tissue particles entrained in effluent as compared to remaining solid tissue surfaces by both ES and coaxial plasma jet irradiation.

5.2. Experimental Set up

5.2.1. Atmospheric Pressure Plasma Jet Generation and Associated Gas Phase Plasma Diagnosis

Figure 5-1 shows the coaxial plasma jet or torch surgical device. The inner electrode was made of an aluminum rod with a diameter of 3.1 mm and round shaped end. The outer coaxial hollow electrode is also made of aluminum with the inner diameter of 5.6 mm and the outer diameter of 6.4 mm. The inner electrode and inside wall of the outer electrode were coated with 16 and 40 μm thick nanoporous Al_2O_3 respectively by a conventional electrochemical process. This porous alumina coating, we judge, increases secondary electron emission fluxes into the plasma, to achieve both more OH rich and spatially homogeneous plasma. This was observed both inside the coaxial electrodes of the plasma torch and in the emerging plasma jet [23]. RF

electrical energy efficiently activated the inner annulus shaped plasma when a proper matching network was employed for maximum power delivery between power 25 to 55 watts under the entire range of atmospheric plasma conditions investigated. The matching network was monitored via a Z-scan (Advanced Energy) impedance measurement system to better tune the matching network, as well as to provide electrical data such as harmonic content of the delivered power.

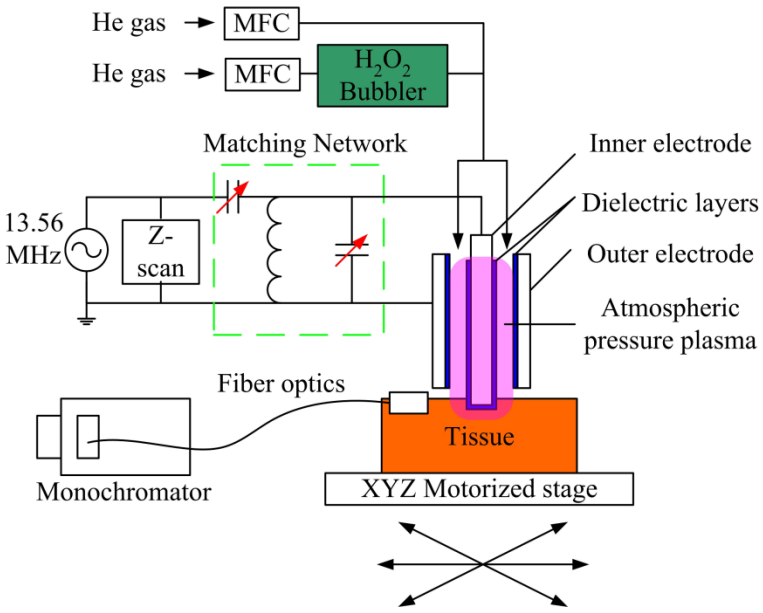

Figure 5-1 Schematic of CSU designed He-H_2O_2 coaxial plasma experimental setup for studying the plasma assisted ES removal of tissue surfaces as compared to pure ES tissue removal

The optical image of coaxial plasma and ES during tissue removal is shown in Figure 5-2. In this coaxial configuration, plasma is generated in the annulus between the cylindrical shaped electrodes. The outer electrode was connected to ground and the inner electrode to RF power source. The inner electrode can protrude 3 mm out from the end of outer electrode so that the electrode could be inserted into the tissue to achieve ES conditions. When the inner electrode is

retracted and the outer annulus positioned over the tissue area to be removed, we do not touch the tissue surface and the plasma jet created only plasma chemical tissue removal reactions.

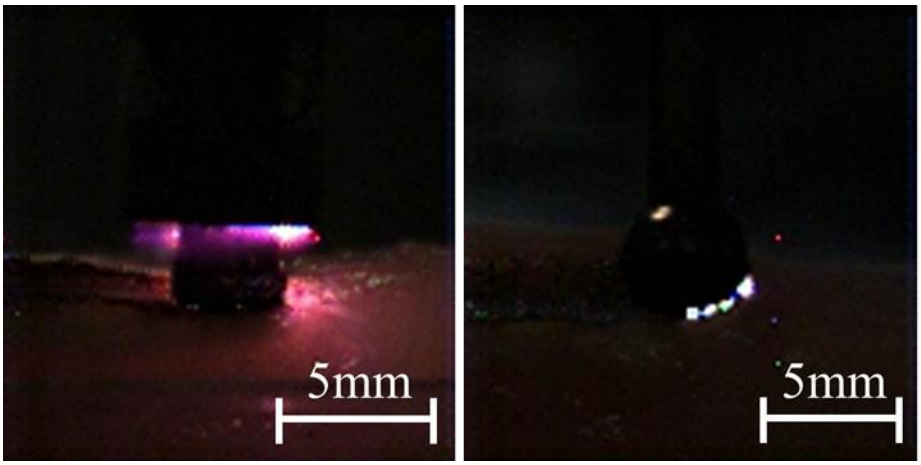

Figure 5-2 Photographic images of CSU coaxial plasma jet (left) and electrosurgery (right) employed for tissue removal

Helium was used as carrier gas with/without 30 wt % hydrogen peroxide (Sigma-Aldrich) to enhance the tissue removal. The chemical additive, H_2O_2, was chosen because it is a feedstock providing a high OH flux, when plasma dissociated. The concentration of H_2O_2 in the downstream plasma volume was controlled by the carrier gas flow through the liquid hydrogen peroxide bubbler, following conventional methodology, and was calibrated to control the chemical feed rate with 600 sccm of helium flow.

5.2.2. FTIR Analysis of Irradiated Tissue Surfaces, Effluent Particulates, and Effluent Exhaust Gases

Figure 5-3 shows the data acquisition system for the FT-IR spectroscopy experiments. A Nicolet 6700 FT-IR system was used for analyzing feedstock and plasma produced chemicals with two accessories. Smart ITR for ATR was employed for analyzing tissue removal exhaust

with entrained tissue particles. The effluent particles in the exhaust gas from the tissue during plasma treatment were trapped on a filter paper (Anodisc, Whatman, 20 nm pore size AAO) and then post irradiation analyzed separately. We also characterized both pre and post plasma jet irradiation tissue surfaces. A separate gas analysis cell with integrated CaF_2 lenses was employed for analyzing exhaust effluent gas, with tissue particles removed, during the plasma assisted ES tissue removal procedure.

The various solid phase tissue samples, both within the removed tissue volume and in the margins, were scanned 32 times with a 4 cm^{-1} resolution. For a baseline comparison tissue samples were treated with both coaxial plasma jet and electrosurgery without plasma at the same total electrical energy delivery, for all FT-IR spectra studies.

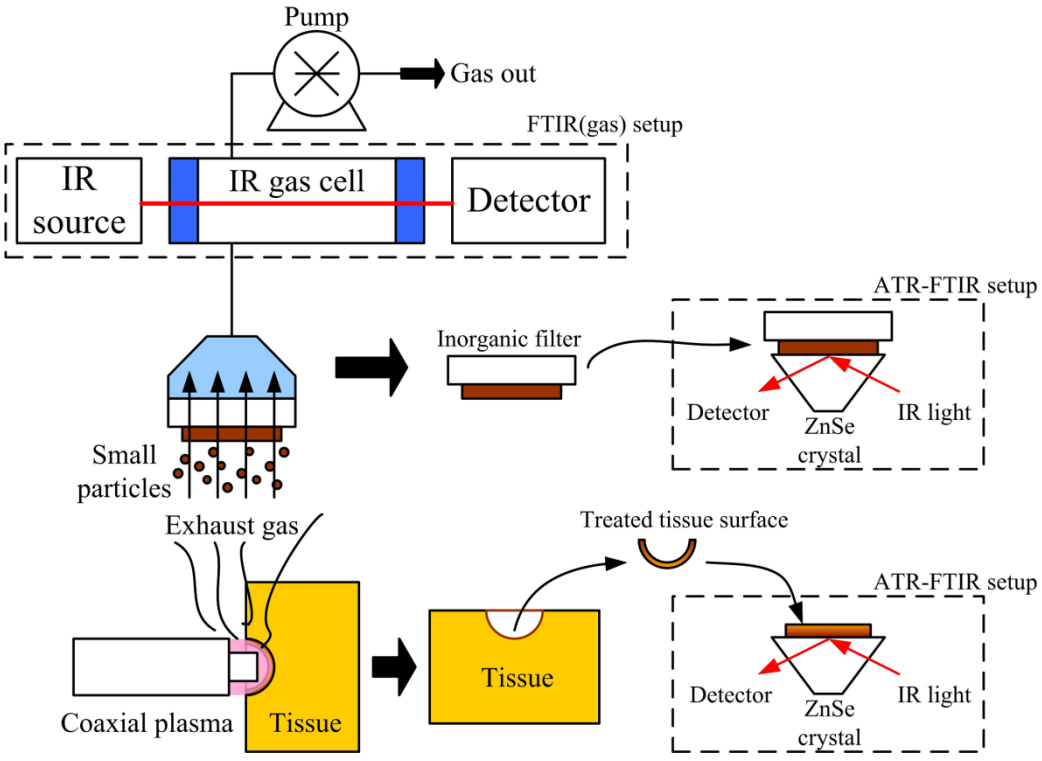

Figure 5-3 Experimental setup for analyzing effluent gas constituents during tissue removal as well as entrained tissue particles. The later was separately removed by filter paper for FT-IR analysis.

5.2.3. Optical Spectroscopic Diagnosis of Active and Afterglow Plasma Jet

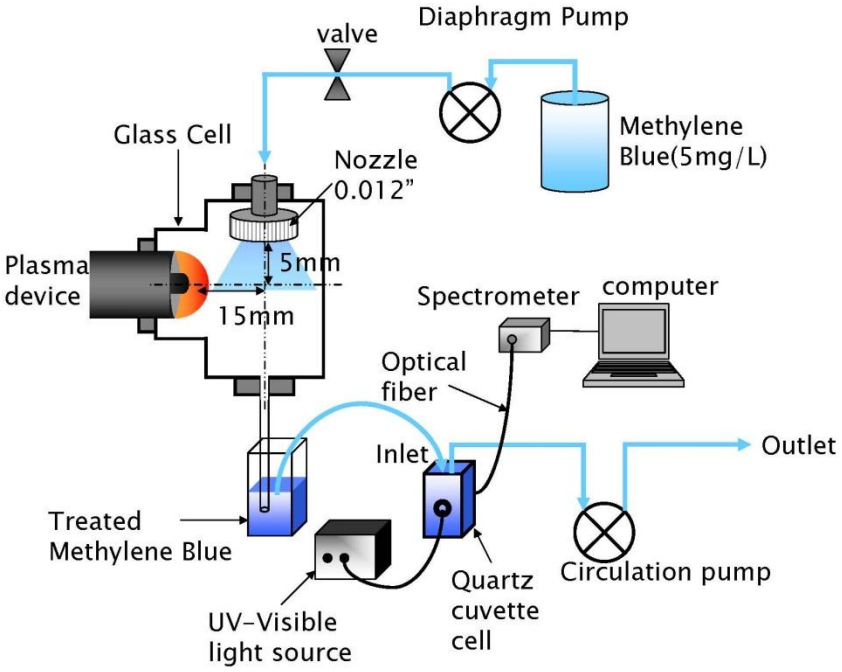

Figure 5-4 Schematic diagram of the CSU experimental setup for the optical absorption of methylene blue solution.

High-speed photography visualized the time based tissue removal process during both plasma jet irradiation and conventional ES. We compared plasma assisted sequenced images to the conventional electrosurgical process as a baseline. The light emitted from the discharge region was delivered to a monochromator (Princeton Instrument, SpectroPro-2750) coupled to a CCD camera (Princeton Instrument, PIXIS-2K) with the help of a focusing lens and an optical fiber. Absolute calibrations of the emitted optical spectra were made using radiance standards including a calibrated mercury-argon lamp (Ocean Optics, HG-1). OH absorption spectrum was also measured independently from emission measurements, using the absorbance of a methylene blue solution (5 mg/L), a compound that selectively but destructively interacts with OH radical emissions. The schematic of the OH absorption measurement is shown in figure 5-4. The

detailed experimental setup is explained in our prior published paper [22]. Gas temperature of the atmospheric He-H_2O_2 plasma that impinges on tissue surfaces were measured by the rotational temperature of OH [24]. Plasma jet gas temperature was also analyzed by curve fitting of N_2 2nd positive spectra to be 600 ± 100 K.

5.2.4. Tissue Preparation, Tissue Ablation, and Tissue Characterization

Fresh chicken breast tissue samples were employed for both the baseline electrosurgery (ES) treatment and the plasma assisted ES treatment. Sample size was approximately 2.5 x 2.5 cm^2 in area, and 1 cm thickness, weighing 5 ± 1 g. The surfaces of tissue samples were freshly cut to minimize non-uniform contact of the powered inner electrode of the coaxial design. Samples were placed on a stage at a fixed distance to form a 1 mm gap between the tissue and the grounded electrode when the protruding powered electrode was pressed into the tissue. The moisture of the tissue samples was kept uniform by placing samples in a sealed petri dish before the plasma treatment. Samples were scanned 25 mm in length with the plasma flame at 47 W RF power using a motorized linear stage at a rate of 10 mm $\cdot$ sec^{-1}. The samples were weighed immediately before and after treatment using an analytical balance to determine the mass of removed tissue and we accounted for lost tissue water by separate flow of non-reactive gas on the tissue surface without plasma. Data are expressed as the mean ± SEM of 10 samples. Statistical analysis was performed using Student's t-test.

5.2.5. Baseline Electrosurgery Study Conditions

Monopolar electrosurgical instrument (Force FX, Valleylab) was employed. The monopolar needle electrode (E1550, Valleylab) was selected to better spatially match the shape and the size

of the plasma electrode geometry. The ES tool was operated only in the "cut" mode for comparison with the coaxial plasma. Neither the coagulation nor the mixed (cut plus coagulation) mode was employed.

5.3. Results and Discussion

5.3.1. Plasma Characterization by Emission and Absorption Spectroscopy

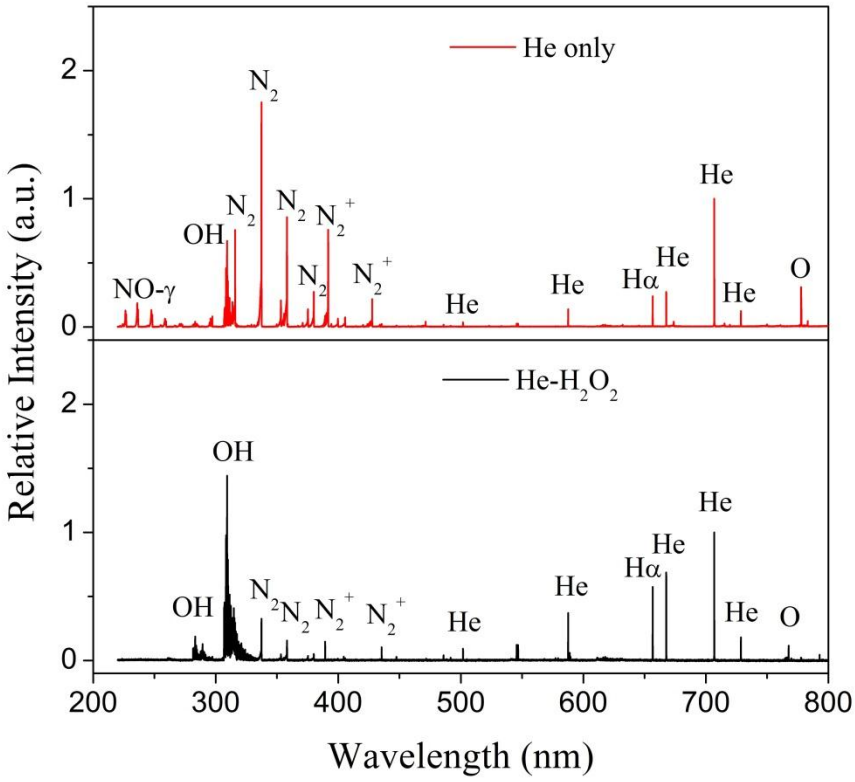

Figure 5-5 Measured optical emission spectra (200 – 800 nm) of both pure helium and mixed He-H_2O_2 coaxial plasma under open air operation conditions (47 W rf power, 600 sccm helium, 16 µl · min^{-1} H_2O_2) [22]

The relation between the measured tissue removal rate and measured OH density of coaxial plasma was of interest as well as exhaust gas species, filtered tissue particles in the effluent and the remaining tissue surfaces after undergoing either ES or plasma assisted ES removal processes.

All were quantified by FT-IR analysis. The emission line intensities were normalized for the hydrogen α line at 656 nm. Optical emission lines, measured in our previous studies [22] are shown in Figure 5-5 and illustrate the strong the OH radical creation that was also confirmed by OH absorption studies. Figure 5-6 shows both the experimental data and the simulated emission band of OH (A,0-X,0) spectrum employed to determine plasma gas temperature. The rotational temperature was determined by fitting the experimental spectrum with a simulation based on the SPECAIR program. Gas temperature of the atmospheric pressure plasma can be approximated by the rotational temperature of OH [24]. The rotational temperatures at 47 W input RF power were determined to be 500 ± 100 K. (Figure 5-6) Plasma jet gas temperature was also analyzed by curve fitting of N_2 2nd positive spectra to be 600 ± 100 K.

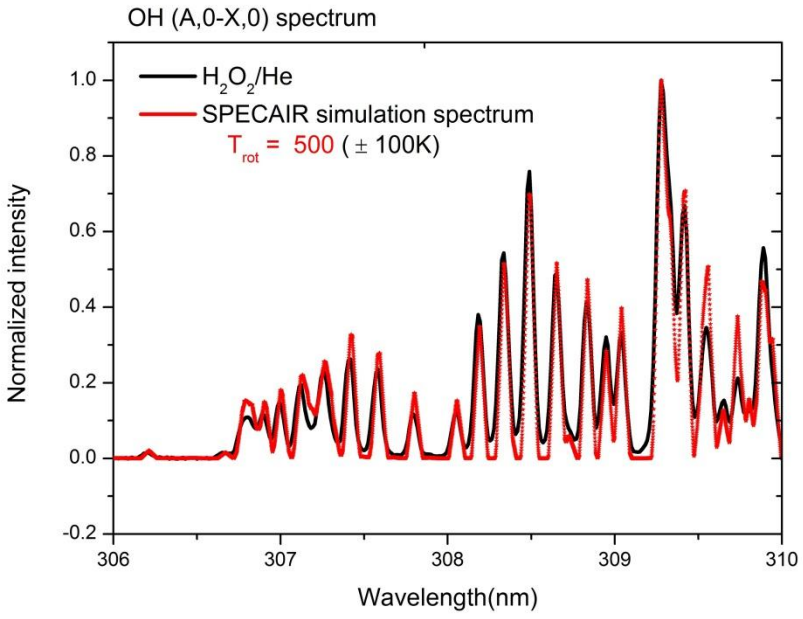

Figure 5-6 Gas temperature measurement of the He-H_2O_2 plasma by comparing the measured and simulated emission band of OH (A,0-X,0) emission line of He-H_2O_2 coaxial plasma jet under fixed conditions (47 W rf power, 600 sccm helium, 7 µl · min^{-1} H_2O_2)

OH densities were measured by both absorption and emission spectroscopy and agreed with each other over the range of experimental conditions. A comparison of the absorbance of methylene blue peak at 664 nm and OH emission intensity at 309 nm as a function of the input RF power is shown in Figure 5-7. Maximum OH production at 47W was observed at around 6 ~ 10 µl min^{-1} flow rate, as depicted in Figure 5-8. Both OH (ground state) radicals measured by absorption and emission spectroscopies followed the same trends with experimental conditions. OH density correlations to tissue removal tracked each other at various H_2O_2 flow rates and the applied RF power. Figure 5-7 and Figure 5-8 both display the strong correlation between the tissue mass loss and the OH radical density fluxes impinging on tissue surfaces.

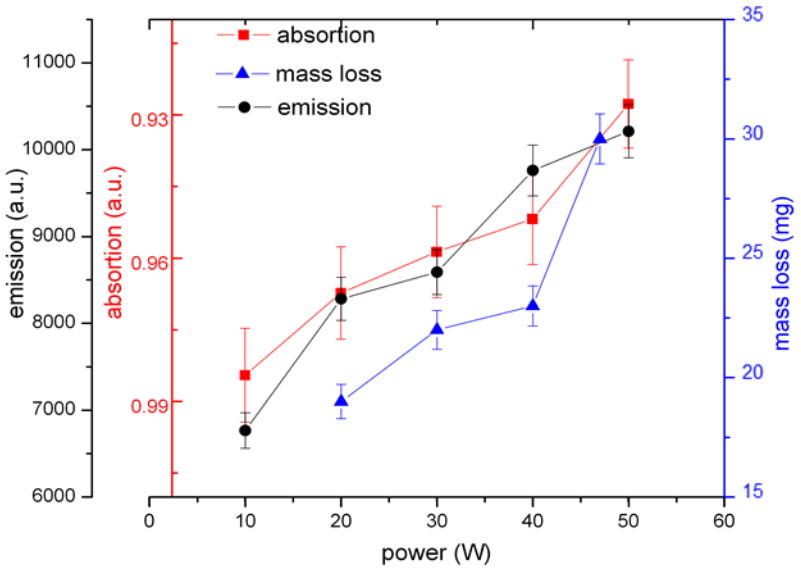

Figure 5-7 Measured correlation of both absorption and emission data for OH radicals along with the corresponding tracking of tissue mass removal loss observed in plasma assisted ES tissue removal as a function of RF input power. (600 sccm helium, 7 µl · min^{-1} H_2O_2, 10 mm · sec^{-1} treatment speed)

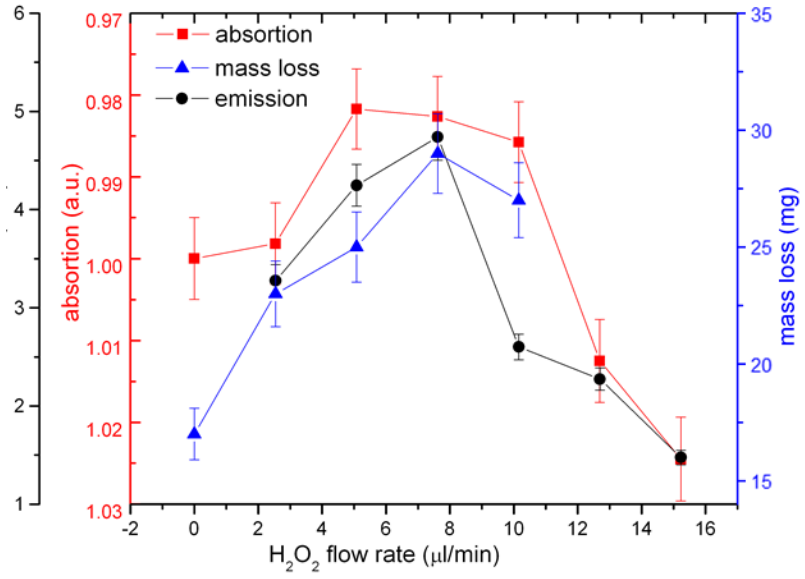

Figure 5-8 Observed correlation of both absorption and emission for OH radicals with corresponding tissue mass losses in plasma assisted ES tissues removal as a function of H_2O_2 flow rate. (47 W, 600 sccm helium, 10 mm · sec^{-1} treatment speed)

5.3.2. FTIR Analysis of the Tissue Removal Process by Plasma Jet Irradiation in Both the cut and Contiguous Regions

Exhaust gas from coaxial plasma jet treatment of tissue samples was compared with pure ES treated samples as described in Figure 5-9. Combustion reactions with organic compounds of tissue and oxygen in the ambient air at high temperature typically produce CO_2 [25] and thermal energy since combustion reaction is exothermic. FT-IR spectra clearly identified CO_2 in the exhaust gas from the pure ES (electrosurgery) tissue removal, whereas the coaxial H_2O_2 plasma torch tissue removal did not show any measurable CO_2 effluent. Gas spectra data from ES effluent indicate a thermally driven tissue combustion reactions and it involved secondary heat generation of the exothermic reaction, whereas the data from H_2O_2 plasma torch tissue treatment has reduced combustion reactions and is in contrast dominated by plasma chemistry gasification reactions.

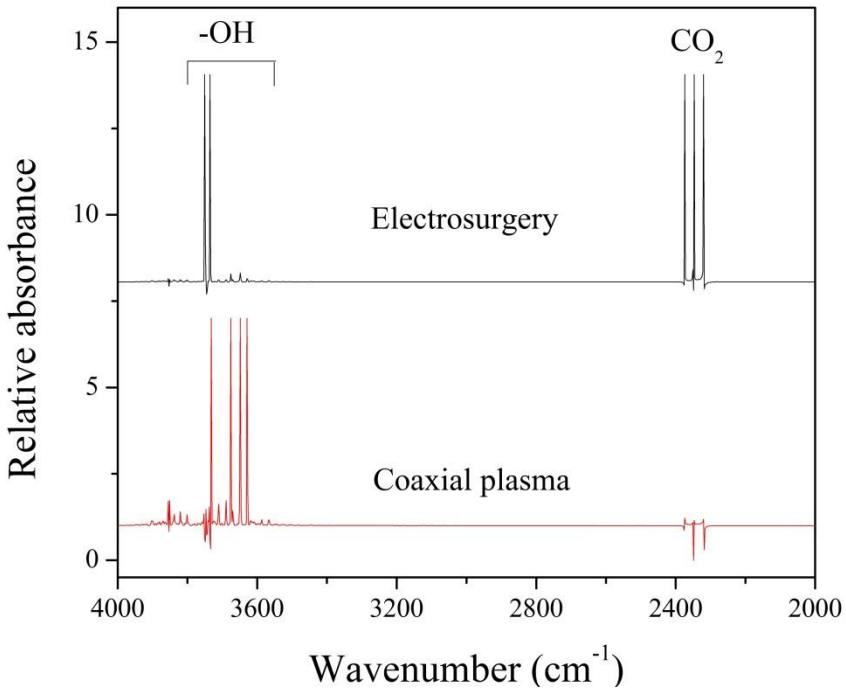

Figure 5-9 FT-IR spectra of the exhaust gas alone (with tissue particles removed) during pure ES and plasma assisted ES tissue removal. (47 W, 600 sccm helium, 7 µl · min^{-1} H_2O_2, 10 mm · sec^{-1} treatment speed)

Filter paper collected tissue particles (smoke) in the effluent of removed tissue from both pure ES and plasma assisted ES tissue removal methods were analyzed and compared. Figure 5-10 shows the FT-IR spectrum of the untreated control sample (fresh chicken breast), tissue particles treated by pure ES sample and those irradiated by the H_2O_2 plasma torch. Although both effluent streams stained the filter paper dark brown color the chemistry of tissue smoke particles was very different as detailed below by FTIR analysis. Chicken breast tissue sample has protein containing amide A, amide I, and amide II bonds as seen in the control (Figure 5-10). Amide A band located at 3300-3400 cm^{-1} is mainly due to N-H stretching vibration and O-H stretching. Amide I at 1633 cm^{-1} is due to carbonyl (C=O) stretching vibrations while the Amide II at 1540 cm^{-1} is due primarily to N-H bending vibrations [26-28].

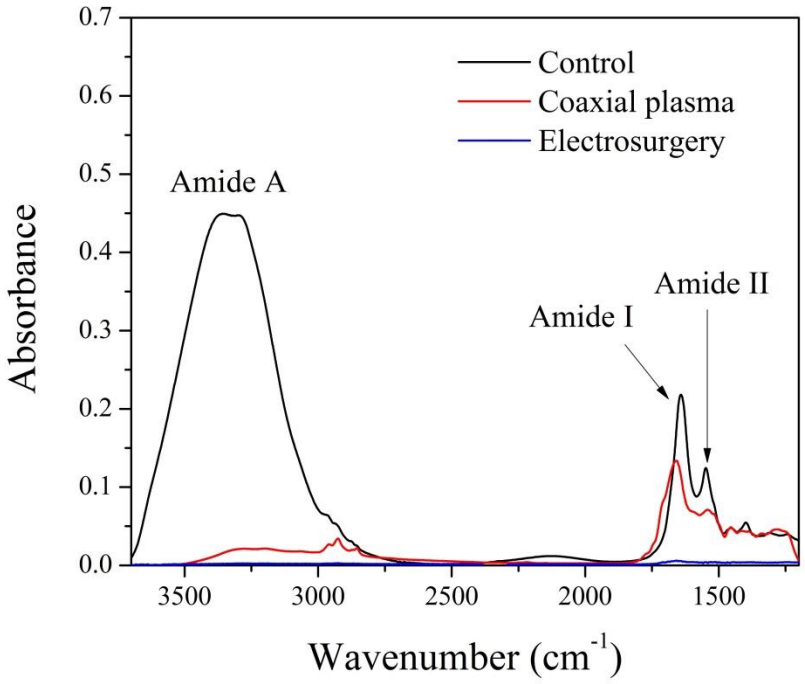

Figure 5-10 Comparison of the FT-IR spectra of the filtered tissue particles filtered out of the effluent gas of both pure ES and plasma assisted ES (47 W RF power, 600 sccm helium, 7 µl · min^{-1} H_2O_2, 10 mm · sec^{-1} treatment speed) and electrosurgery (47W)

The protein peaks of amide A, amide I, and amide II were present in the coaxial H_2O_2 plasma torch driven smoke particles but absent from pure electrosurgical device effluent smoke particles spectra. This indicates no protein segments were evolved in the effluent from ES tissue processing, while protein segments were observed following by coaxial plasma treatment that relies on plasma chemical reactions. The filtered particles from ES processing seems a carbon resulted from carbonization during combustion process. Since FTIR does not detect symmetric chemical bonds such as carbon, absorption spectrum did not show any chemical bonds. ES tissue removal accompanied carbonization, outcome of incomplete combustion process that breaks all of the chemical bonds of protein with excessive heat energy. Amide A, amide I and amide II represents protein secondary and tertiary structures [29]. Reduced amide peaks of the tissue particles from coaxial plasma processing indicates tissue denaturation that protein lose its

secondary and tertiary structures but keep its primary structure, long chain of amino acids. Protein secondary and tertiary structures are based on hydrogen bonds that are relatively weak chemical bonds (typical hydrogen bond energy ≈ 4 – 8 kJ/mol) [30] than those covalent bonds of protein primary structure (typical covalent bond energy of protein primary structure ≈ 300 – 800 kJ/mol) [31]. It is considered that protein primary structures are still remained since its covalent bonding energy is much higher than hydrogen bonding energy. Therefore, coaxial plasma mainly broke the weak hydrogen bonds between long chains of protein.

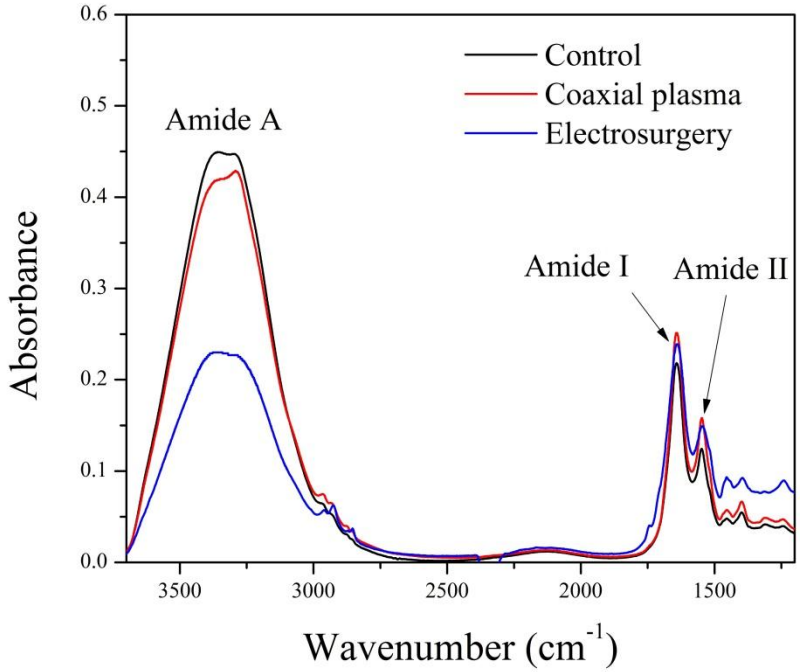

Figure 5-11 Comparison of FT-IR spectra of tissue samples taken from area inside the remaining tissue removal ablation groove, as compared to the contiguous region. We compare samples treated by plasma assisted ES (47 W, 600 sccm helium, 7 µl · min^{-1} H_2O_2, 10 mm · sec^{-1} treatment speed) and samples treated by pure ES (47W)

In Figure 5-11 amide A, amide I, and amide II bonds observed in the remaining irradiated tissue surfaces did not change after coaxial plasma tissue removal, whereas in contrast pure ES exposure reduced the Amide A bond in the remained tissue. During ES tissue removal process,

proteins were gasified by I^2R ohmic heating and produced CO_2 and CO by combustion of organic materials. The amide A bond in the remaining tissue after pure ES treatment was affected by the heat. During coaxial plasma tissue removal process, all of amide A, amide I, and amide II bonds in the filtered particles remained even after plasma chemical removal of the bulk tissue.

In our previous FTIR study [22], periphery part of tissue after coaxial plasma removal showed reduced amide peaks, and newly generated lipid peaks and nucleic acid (DNA and RNA) peaks while the ablation groove showed no difference with control tissue. It indicates that remained tissue on ablation groove was intact. Tissue on periphery was denatured by plasma heat and/or chemicals.

Muscle fiber (muscle cell) is multinucleated. Nuclei are just underneath the sarcolemma, a membrane of muscle fiber and lipid bilayers (also dominant in cell membranes). Both can be damaged by lipid peroxidation with ROS (reactive oxygen species) such as OH, HO_2, O_2^-, and H_2O_2. Since OH is far more reactive than HO_2, O_2^-, and H_2O_2, [32, 33] lipid bilayer membranes can be easily damaged by OH radical flux from the plasma jet. Then plasma-assisted ES ruptures the damaged membranes and breaks the protein secondary and tertiary structures. The nucleic acids in the nuclei and ruptured membranes (lipids) are spread over the periphery of the surgical cut. It is judged therefore that the coaxial H_2O_2 plasma torch driven tissue removal is primarily chemical because it required less heat to remove equal amounts of tissue as compared to pure ES tissue removal. Moreover, we judge that the primary removal mechanism is plasma chemical driven tissue surface reactions driven by OH reactions. It has been reported previously that other plasma generated radical chemical reactions also improve tissue removal rates in plasma chemical tissue gasification. In that earlier work the addition of a feedstock of CCl_4 and other

chlorine bearing feedstock's into an argon plasma jet achieved selective tissue removal by chlorine chemistry and also evidenced unique tissue cut spatial profiles [34]. We conclude that at least two distinct chemical driven plasma assisted radical reaction can enhance conventional ES (electrosurgical) processes resulting in more tissue removal in less time with less associated heat damage on remaining nearby tissue by employing low temperature plasma chemistry [22]. Finally we observed in both cases, less residual tissue sticks to the ES electrodes with the addition of plasma radicals, allowing for longer use of ES electrodes, between electrode cleanings by the surgery team to remove build-up of tissue char deposits that impede ES rates.

In summary optical emission and adsorption both indicate that a low flux of H_2O_2 feedstock into a plasma torch ES surgery tool, increased OH production in the helium dominated coaxial plasma. The emission spectra normalized to the hydrogen α line (656 nm) showed an optimum H_2O_2 concentration exists (Figure 5-5). Under these conditions the OH concentrations tracked tissue removal rates, as experimental conditions were varied by independent absorption and emission spectroscopy. The corresponding tissue mass losses and OH densities also tracked both varying RF power delivered to the plasma jet and the H_2O_2 flow rate as shown in in Figure 5-7 and Figure 5-8. We judge therefore that OH is major factor in the tissue removal chemistry and also plays a role in reducing the temperature of electrosurgical processes as well as reducing the undesired build-up of tissue char on ES electrodes over time.

Coaxial H_2O_2 plasma torch driven treatment of tissue emitted little CO_2 effluent, an indication of reduced thermally driven combustion processes and increased chemical gasification processes for tissue removal (Figure 5-9). Filtered tissue particles found in the effluent exhaust gas from the coaxial plasma jet treatment of tissue kept amide bonds intact as compared to baseline pure ES tissue processes, which destroyed them as shown in Figure 5-10 following pure

ES treatment. These results explain that lipid bilayer of muscle fiber membrane and nuclear membranes were damaged by OH in the plasma jet and ruptured by plasma-assisted ES. Our previous FTIR study [22] that lipid and nucleic acids found on periphery of removed tissue supports this conclusion. And the proteins segments found in the filtered tissue particles explain that the hydrogen bonds building protein secondary and tertiary structures were broken by plasma-assisted ES while ES destroyed all of the amide I and II bonds in the treated tissue by excessive heat energy.

The tissue treated by coaxial plasma contained slightly less amide A bond than the untreated control sample but much more than electrosurgery treated tissues (Figure 5-11). In short the remaining tissue after coaxial plasma treatment has more residual amide A whereas the electrosurgery treated tissue has less amide A intact and more combustion products. This data suggests the potential use of FTIR analysis in plasma assisted ES to in-situ study tissue margins and better track tissue conditions during surgery. Finally FT-IR analysis tracks the role in tissue removal of OH plasma chemistry.

5.4. Conclusions

We studied the coaxial H_2O_2 plasma-assisted ES and found that the OH radical flux impinging on tissue surfaces increased the tissue removal rate at lower tissue process temperatures, as compared to pure ES tissue removal, which required higher tissue temperatures for similar removal rates. Plasma-assisted ES also reduced the contiguous tissue temperature for comparable tissue removal rates, and left amide A bonds intact in the surgical margins. FTIR data elucidate this difference in tissue removal between plasma-assisted ES and pure ES (electro surgery) thereby allowing monitoring of the tissue margins, to avoid inadvertent contiguous

tissue damage and possibly during surgery. The role of OH radicals in plasma-assisted ES was illustrated by analyzing the FTIR spectra of both effluent exhaust gas particulates and the remaining tissue in both the cut site as well as contiguous remaining tissue after treatment.

OH lines in the plasma emission spectrum tracked tissue removal rate (mass loss/cut) as a function of RF input power and H_2O_2 flow rate. Pure ES tissue removal processes involved thermal combustion of tissue as compared to plasma-assisted ES methods, which showed little combustion products. This was determined by analyzing the exhaust CO_2 gas in the two cases and by analyzing the filtered tissue particle in the effluent stream as well as by tracking the residual solid tissue surface bonds after treatment by both methods. Pure ES tissue treatment exhaust gas had dominant CO_2 effluent indicating combustion processes, whereas no CO_2 was observed in plasma assisted ES. Filtered particles in the pure ES tissue removal process exhaust gas did not have any residual chemical bonds such as proteins with amide A, amide I and II bonds. In contrast, filtered tissue particles in the exhaust gas from the coaxial H_2O_2 plasma torch driven tissue removal retained residual amide A, amide I and amide II bonds. The remaining amide bonds indicate less residual damage on proteins in the treated tissue and in its margins.

In conclusion, OH radicals play a major in our tissue removal conditions by volatilizing both lipid bilayers of sarcolemma and nuclear membranes. Adding plasma chemistry to ES conditions, in short, allowed ES surgery to use less heat for comparable tissue removal rates in agreement with our previous study [22].

REFERENCES

[1] Myeong Yeol Choi, Il Gyo Koo, Sung Kil Kang, Paul Y. Kim, Jin Hoon Cho, Jae-Chul Jung, and George J. Collins, *IEEE Transactions on Plasma Science*, submitted (under review)
[2] Janda P, Sroka R, Baumgartner R, Grevers G, Leunig A, *Lasers Surg. Med.* **2001**, 28, 404.
[3] Guo J, Freidberg SR, Thomas CB, Pankratov MM, Even M, Shapshay SM, *Chin. Med. J.* **1998**, 111, 928.
[4] Sicklinger A, Lenz H, Eichler J, *Laryngorhinootologie* **2000**, 79, 536.
[5] Janda P, Sroka R, Betz CS, Baumgartner R, Leunig A, *Lasers Surg. Med.* **2002**, 30, 31.
[6] Lippert BM, Werner JA, *Laryngorhinootologie* **1996**, 75, 523.
[7] Werner JA, Rudert H, *HNO* **1992**, 40, 248.
[8] Janda P, Tauber S, Sroka R, Baumgartner R, Grevers G, Leunig A, *Lasers Surg. Med.* **2000**, 27, 129.
[9] Roggan A, Mesecke-von Rheinbaben I, Knappe V, Vogl T, Mack MG, Germer C, Albrecht D, Muller G, *Biomedizinische Technik* **1997**, 42, 332.
[10] Caballero JM, Borrat P, Paraira M, Martí L, Ristol J, *Actas Urol Esp.* **2010**, 34, 403.
[11] Ter Haar G, Roberston D, *Eur Urol.* **1993**, 23, 8.
[12] Sibille A, Prat F, Chapelon JY, Abou el Fadil F, Henri L, Theillère Y, Ponchon T, et al. *Oncology* **1993**, 50, 375.
[13] Massarweh NN, Cosgriff N, Slakey D. *Am. Coll. Surg.* **2006**, 202, 520.
[14] Tucker RD, Schmitt OH, Sievert CE, Silvis SE, *Surg Gynecol Obstet* **1984**, 159, 39.
[15] Jones CM, Pierre KB, Nicoud IB, Stain SC, Melvin WV. *Curr. Surg.* **2006**, 63, 458.
[16] Dubiel B, Shires PK, Korvick D, *Veterinary Surgery* **2010**, 39, 909.
[17] Michael K. Flynn, Alison C. Weidner, Cindy L. Amundsen, *American Journal of Obstetrics and Gynecology* **2006**, 195, 1869.
[18] J. H. Kim, J. Sohn, J. H. Cho, M. Y. Choi, I. G. Koo, W. M. Lee, *Plasma Process. Polym.* **2008**, 5, 377.
[19] A. Hammad, E. Amanatides, D. Mataras, D. Rapakoulias, *Thin Solid Films* **2004**, 255, 451.
[20] Hiroshi Ohkawa, Kinpei Fukushima, *Surface & Coatings Technology* **2006**, 200, 5829.
[21] Ashish Sharma, Amy Pruden, Ovidiu Stan, George J. Collins, *IEEE Trans. Plasma Sci.* **2006**, 34, 1290.
[22] Myeong Yeol Choi, Il Gyo Koo, Paul Y. Kim, Sung Kil Kang, Yoon-Sun Kim, Jae-Chul Jung and George Collins, *Plasma Processes and Polymers*, **2012**, DOI: 10.1002/ppap.201200003
[23] I. G. Koo, J. H. Cho, M. Y. Choi, and W. M. Lee, *Appl. Phys. Lett*. **2007**, 91, 041502.
[24] J Raud, M Laan and I Jogi, *J. Phys. D: Appl. Phys.* **2011**, 44, 345201.
[25] Thomas Fleckl, Helmut Jager, Ingwald Obernberger, *Proceedings of the 5th European Conference on Industrial Furnaces and Boilers* **2000**, ISBN-972-8034-04-0.
[26] A. Melin, A. Perromat and G. Deleris, *Biopolymers (Biospectroscopy)* **2000**, 57, 160.
[27] S. Raudenkolb, W. Hubner, W. Rettig, S. Wartewig and R.H.H. Neubert, *Chem. Phys. Lipids* **2003**, 123, 9.
[28] A. Nilsson, A. Holmgren and G. Lindblom, *Biochemistry* **1991**, 30, 2126.
[29] Tanford C. *Adv. Prot. Chem.* **1968**, 23, 121.
[30] Lodish H, Berk A, Zipursky SL, et al. *Molecular Cell Biology.* 4th edition. New York, **2000**.
[31] Raymond Chang, *General Chemistry*, 4th ed. McGraw-Hill **2005**.
[32] Halliwell B. Gutteridge JMC. *Free radicals in biology and medicine*, 2nd ed. Oxford: Clarendon Press, **1989**.

[33] Sies H, ed. *Oxidative stress, oxidants and antioxidants*, New York: Academic Press, **1991**.
[34] Il Gyo Koo, Cameron A. Moore, Myeong Yeol Choi, Gon Jun Kim, Paul Y. Kim, Yoon-Sun Kim, Zengqi Yu, George J. Collins, *Plasma Processes and Polymers* **2011**, 8, 1103.

CHAPTER 6. REACTIVE HYDROXYL RADICAL-DRIVEN ORAL BACTERIAL INACTIVATION BY RF ATMOSPHERIC PLASMA

We demonstrated OH rich plasma generated in RF driven argon plasma jet with H_2O_2 entrained in the feedstock gas. The plasma jet was applied on the dental pathogen Streptococcus mutans. 5-log10 reduction was achieved by exposure on RF plasma jet for 3 min. Optical emission spectroscopy identified substantial excited state OH generation inside the plasma and relative OH formation was verified by optical absorption. Integration of O emissions was inversely proportional to the H_2O_2 concentration and did not track the bacterial inactivation rate. The bacterial inactivation rate increased with increasing OH generation and reached a maximum 5-log10 reduction with 0.6% H_2O_2 vapor. Concentration of toxic ozone, drawback of plasma bacterial inactivation, was kept lower than the maximum allowable ozone concentration in industrial working areas (0.1 ppm) with addition of H_2O_2 vapor to the plasma [1].

6.1. Introduction

Non-thermal atmospheric pressure plasmas have been investigated as possible alternative tools for dental applications such as bacterial inactivation [2], tooth whitening [3, 4], and sterilization of dental materials and instruments [5]. Conventional bacterial inactivation in clinical practice is widely carried out using chlorhexidine (CHX), a chemical antiseptic with well-known antimicrobial efficacy. However, irritation of oral mucosa and staining of teeth have been reported with the use of CHX [6].

Many research groups have reported bacterial inactivation for dental application by atmospheric pressure plasma [7, 8]. The inactivation mechanisms may be based on plasma-generated UV radiation, heat, charged particles, and reactive species, depending on the plasma

conditions, but ozone is thought to play an important role in plasma sterilization at atmospheric pressure. Breathing ozone is known to cause chest pain, aggravate asthma, impair respiratory function, and damage lung tissue [9]. Our work was motivated by a search for a hydroxyl radical (OH)-driven bacterial inactivation method using low temperature atmospheric pressure plasma with low-level ozone generation. In this chapter we present the outline of our approach and evidence of bacterial inactivation.

6.2. Experimental Setup

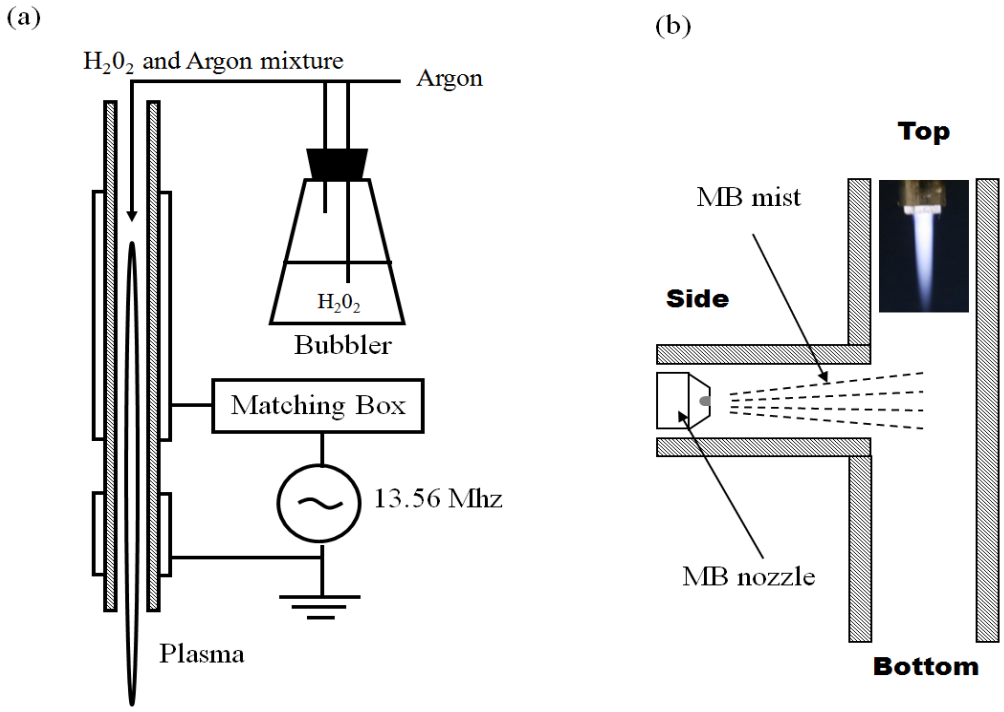

Figure 6-1 Schematic diagrams of (a) CSU designed RF-driven atmospheric plasma jet with H_2O_2 bubbler (b) experimental setup for measuring OH using methylene blue (MB) dye degradation method.

The plasma jet consists of a ceramic tube surrounded by two metal electrodes; one powered by a 13.56 MHz power (Cesar-133, Advanced Energy) and the other grounded (Figure 6-1(a)). Argon carrier gas, regulated by a mass flow controller, flows into two lines; one directly through the ceramic tube and the other through a bubbler containing 30 % hydrogen peroxide (H_2O_2) with water to form a gas mixture of Ar, H_2O, and 0 – 1 % final concentration (v/v) of H_2O_2. A 10W effective power was sufficient to sustain a cold plasma jet with up to 1% entrained H_2O_2 vapor. The presence of OH was verified using an aerated aqueous methylene blue (MB) solution [10] (0.3 mM, 0.8 ml/s) as depicted in Figure 6-1(b). Photos of the plasma jet operating with 0 – 1 % H_2O_2 vapor concentrations are presented in Figure 6-2(a). The plasma jet is ~10 mm in length without H_2O_2 vapor and gradually shortens to ~3 mm as H_2O_2 vapor concentration reaches 1 %. Above 1 % H_2O_2 vapor, plasma is only sustained inside the ceramic tube.

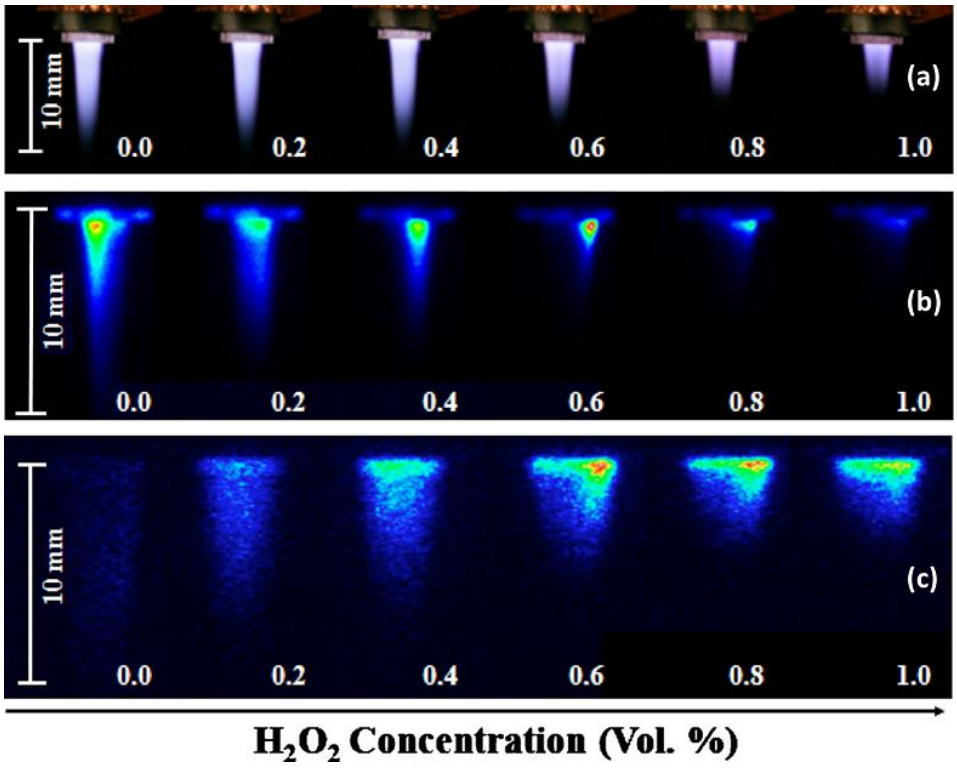

Figure 6-2 (a) Photos, (b) ICCD images (308 nm filter) and (c) ICCD images (777.1 nm) of the CSU plasma jet plume with entrained H_2O_2 vapor concentration ranging from 0 to 1 %.

6.2.1. Temperature and Ozone Concentration Measurement

Average plasma gas temperature were measured by thermosensor (Fluke 54 II) as 41.3 ± 2 ℃ and 34.9 ± 2 ℃ at the end of the plasma plume and 3 mm below the end, respectively. In comparison, sterilization by dry heat is typically carried out at 160 – 170 ℃ for up to 1 h. There was no significant change in gas temperature with addition of H_2O_2 vapor. The amount of plasma-generated ozone, measured 5 cm below the plume termination (Eco Sensors A-22), decreased with the concentration of H_2O_2 vapor as depicted in Figure 6-4. Addition of 0.4% H_2O_2 vapor reduced the ozone concentration to less than 0.1 ppm, the exposure limit recommended by occupational safety and health organizations (OSHA). At 1 % H_2O_2 vapor concentration, the level of ozone decreased by > 83 % compared to pure Ar plasma.

6.2.2. ROS and OH Measurement with ICCD

The spatial distribution of hydroxyl radical (OH) was determined by means of optical emission spectroscopy with an intensified charge coupled device (ICCD) camera (Princeton Instruments PI-MAX) and 308 nm bandpass filter for selective OH observation. Atomic O radical distribution is also determined with 777.1 nm bandpass filter. ICCD images presented in Figure 6-2 were acquired with a fixed integration time of 20 ms and gain of 150.

6.2.3. Sterilization

We conducted a sterilization experiment with the dental pathogen Streptococcus mutans (S. mutans, strain: KCTC 3065/ATCC 25175). A disk confined within the plasma treatment area was spot inoculated with a 2 μl suspension (~8×10^9 CFU/ml) of S. mutans and dried for 10 min. After 3 min plasma treatment at a distance of 3 mm from the end of the plasma jet, each disk was

vortexed in 1 ml of phosphate buffered saline and serial dilutions were spread on brain heart infusion (BHI) agar plates. The plates were incubated at 37 ℃ for 24 h to determine bacterial colony counts. Inactivation was evaluated by determining the ratio of colony counts after treatment (N) to control ($N_0 \approx 8 \times 10^9$ CFU/ml). All data presented are mean ± standard error of measurement of three independent experiments.

6.3. Result and Discussion

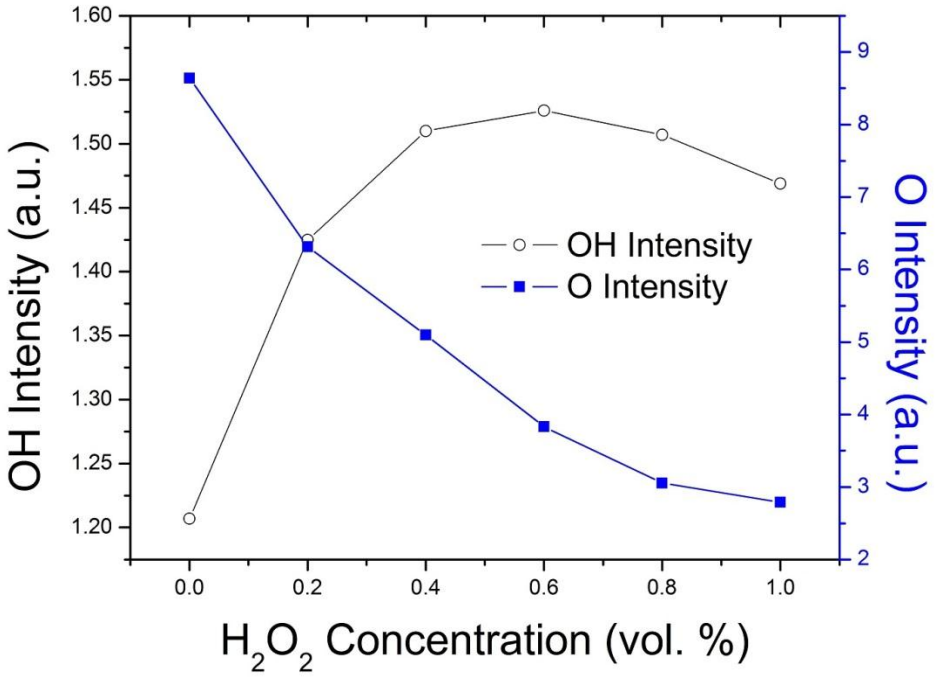

Figure 6-3 Relative intensities of OH and O emission from the plasma jet plume with entrained H_2O_2 vapor concentration ranging from 0 to 1 vol. %.

The concentration of O and OH was measured by integrating the emission intensities of each species as shown in Figure 6-3. The highest concentration of excited state of OH is observed at 0.6 % H_2O_2 vapor concentration and most abundant at the end of jet nozzle, it appears to travel

over a millimeter range during its lifetime. ROS is monotonically decreased as increasing concentration of H_2O_2 vapor because of high reactivity of ROS with H_2O_2 and H_2O vapor [10].

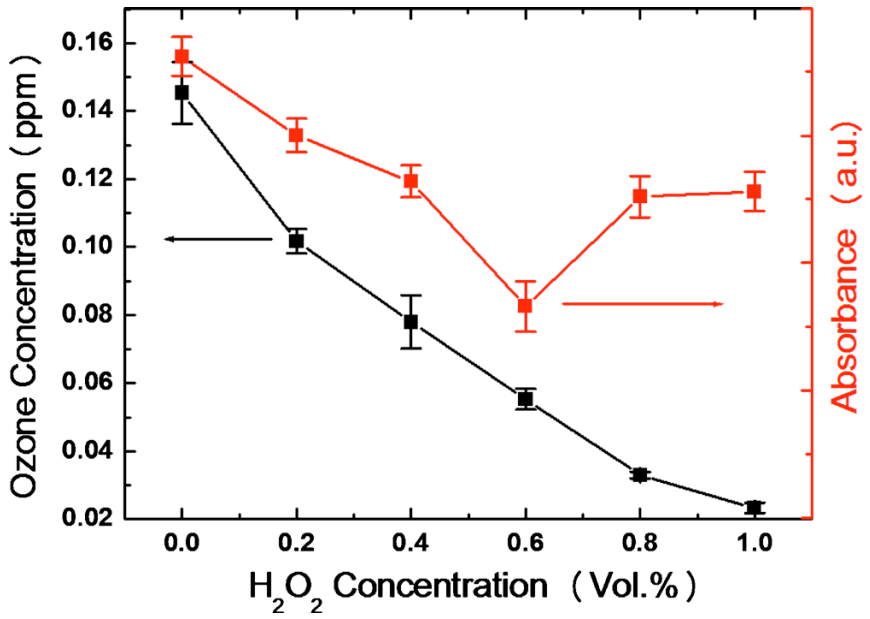

Figure 6-4 Saturated ozone concentration (black squares) measured 5 cm below the end of plasma plume and absorbance of MB at 655 nm (red squares) after plasma treatment with entrained H_2O_2 vapor concentration ranging from 0 to 1 %.

Ozone concentration measured with the ozone sensor (Eco Sensors A-22) decreased with H_2O_2 concentration. It agrees with the O emission intensity degradation with H_2O_2 addition in Figure 6-3. The absorbance at 665 nm of MB decreased as a function of H_2O_2 vapor concentration up to 0.6% (Figure 6-4). The absorbance of MB is inversely proportional to OH concentration. This absorption data agrees qualitatively with optical emission spectra measurements with ICCD in Figure 6-3 and also confirms that the plasma-generated OH can travel over a millimeter to the target.

It has been reported that RF plasma produces enough high energy electrons to break both the HO-OH bond (2.2 eV) in H_2O_2 and the O_2-H bond (3.8 eV) in H_2O [12] to generate OH [10]. In

these reactions, OH production increases linearly with the concentrations of H_2O_2 and H_2O. On the other hand, total plasma emission is observed to weaken with H_2O_2 concentration, signifying decreased electron density [Figure 6-2(a)]. Therefore, OH production reaches a maximum value at a specific H_2O_2 concentration, which our measurements indicate occurs near 0.6% H_2O_2. Ozone can be dissociated by H_2O in the feedstock and OH and H reaction products (from H_2O_2 and H_2O dissociation) by the following secondary reactions [10].

$$\bullet OH + O_3 \rightarrow HO_2\bullet + O_2, \text{ Rate: } 7.55 \times 10^{-14} \text{ cm}^3 \text{ s}^{-1} \quad (1)$$

$$\bullet H + O_3 \rightarrow \bullet OH + O_2, \text{ Rate: } 1.4 \times 10^{-10} \text{ cm}^3 \text{ s}^{-1} \quad (2)$$

$$HO_2\bullet + O_3 \rightarrow \bullet OH + 2O_2, \text{ Rate: } 1.1 \times 10^{-14} \text{ cm}^3 \text{ s}^{-1} \quad (3)$$

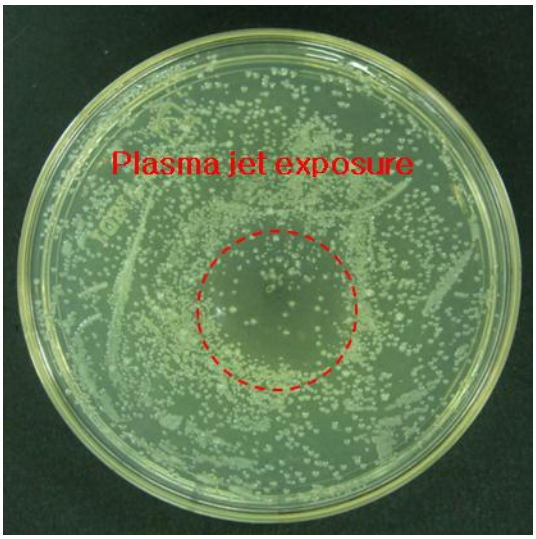

Figure 6-5 Sterilization of Streptococcus mutans by RF driven argon plasma jet with H_2O_2 entrained in the feedstock gas.

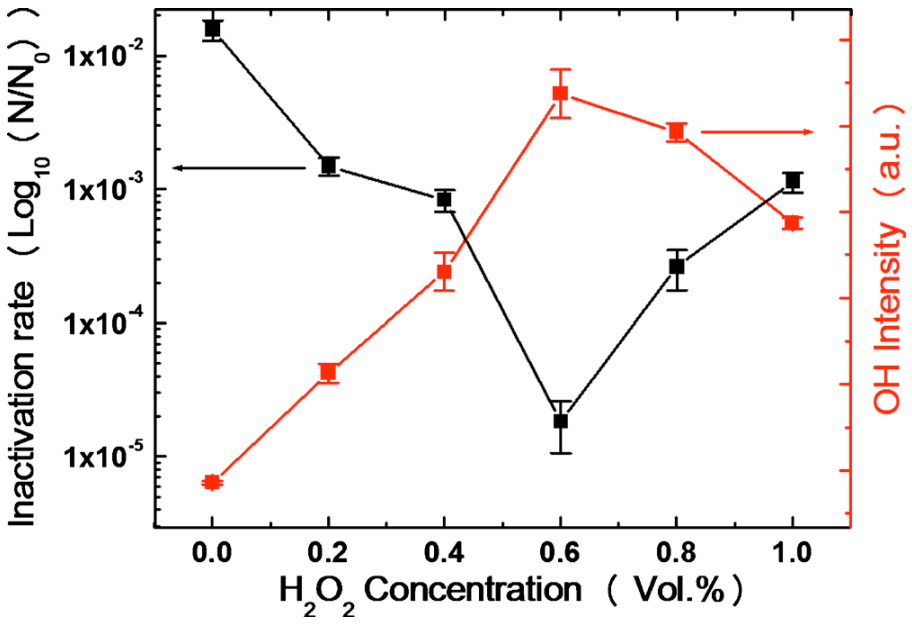

Figure 6-6 (Color online) Inactivation rate [log10(N/N_0)] of S. mutans (black squres) and integrated OH intensity (red squares) as a function of H_2O_2 vapor concentration. $N_0 \approx 8 \times 10^9$ CFU/ml, treatment time: 3 min.

Figure 6-5 shows the agar plate after H_2O_2 plasma treatment. As shown in the left axis of Figure 6-6, the bacterial inactivation rate increased with H_2O_2 vapor up to 0.6 % but decreased at higher concentrations. Inactivation efficacy was highly dependent on the OH concentration (determined by optical emission spectroscopy) as plotted on the right axis.

For direct treatment of dental germs in the oral cavity, a plasma jet must be small and obviously non-thermal. In this study, we achieved a 5-log10 reduction in S. mutans using a 1 mm diameter RF plasma jet operating below 43 ℃. While ozone, often generated by atmospheric pressure plasmas, is highly effective in killing bacteria, its toxicity presents a disadvantage for use in the clinical setting. By adding H_2O_2 vapor to the plasma feedstock gas, we reduced ozone formation yet still inactivate bacteria through short-lived OH.

6.4. Conclusions

OH rich plasma was generated with H_2O_2 addition into Ar plasma jet driven by 13.56 MHz power. Concentration of reactive species such as OH, O, O_3 in the plasma was controlled with amount of H_2O_2 addition into the plasma jet. The plasma density weakened as increasing the H_2O_2 concentration in the plasma. O (777.1 nm filtered in ICCD image) and Ozone (measured with Eco Sensor) concentration decreased as concentration of H_2O_2 increase. OH concentration measured with both ICCD (308 nm filter) and MB absorbance (665 nm) increased from 0 to 0.6 % of H_2O_2 and decreased from 0.6 to 1.0 %. The bacterial inactivation rate tracked the OH concentration in the plasma. It was achieved 5-log10 reduction in S. mutans using RF plasma jet with 0.6 % of H_2O_2 for 3 min treatment. With 0.6 % of H_2O_2, OH concentration was at its highest, and Ozone concentration was kept lower than the exposure limit recommended by OSHA. Therefore, RF plasma can be tailored for bacterial inactivation with desired species (OH) and without undesired species (O_3) in the plasma.

REFERENCES

[1] Sung Kil Kang, Myeong Yeol Choi, Il Gyo Koo, Paul Y. Kim, Yoon sun Kim, Gon Jun Kim, Abdel-Aleam H Mohamed, George J. Collins and Jae Koo Lee, *Applied Physics Letters*, **2011**, 98, 143702.
[2] Ozlem Yardimci and Peter Setlow, *IEEE Trans. Plasma Sci.* **2010**, 38, 937.
[3] H. W. Lee, G.J. Kim, J. M. Kim, J. K. Park, J. K. Lee, and G. C. Kim, *J. Endod.* **2009**, 35, 587.
[4] Hyun Woo Lee, Seoul Hee Nam, Abdel-Aleam H. Mohamed, Gyoo Cheon Kim, and Jae Koo Lee, *Plasma Process. Polym.* **2010**, 7, 274.
[5] A. G. Whittaker, E. M. Graham, R.L. Baxter, A. C. Jones, P. R. Richardson, G. Meek, G. A. Campbell, A. Aitken, H. C. Baxter, *Journal of Hospital Infection* **2004**, 56, 37.
[6] C. A. Gürgan, E. Zaim, I. Bakirsoy, and E. Sykan, *J. Periodontol.* **2006**, 77, 370.
[7] Chunqi Jiang, Meng-Tse Chen, Christoph Schaudinn, Amita Gorur, P. Thomas Vernier, J. William Costerton, David E. Jaramillo,Parish P. Sedghizadeh, and Martin A. Gundersen, *IEEE Trans. Plasma Sci.* **2009**, 37, 1190
[8] Xinpei Lu, Yinguang Cao, Ping Yang, Qing Xiong, Zilan Xiong, Yubin Xian, and Yuan Pan, *IEEE Trans. Plasma Sci.* **2009**, 37, 668.
[9] A. Mahfoudh, M. Moisana, J. Seguinb, J. Barbeaub, Y. Kabouzia, and D. Keroacka, *Ozone Sci. Eng.* **2010**, 32, 180.
[10] I. A. Soloshenko, V. V. Tsiolko, V. A. Khomich, V. Yu. Bazhenov, A. V. Ryabtsev, A. I. Schedrin, and I. L. Mikhno, *IEEE Trans. Plasma Sci.* **2002**, 30, 1440.
[11] N. Shimizu, C. Ogino, M. F. Dadjour, and T. Murata, *Ultrason. Sonochem.* **2007**, 14, 184.
[12] S. M. Lee, Y. J. Hong, Y. S. Seo, F. Iza, G. C. Kim, and J. K. Lee, *Comput. Phys. Commun.* **2009**, 180, 636.

CHAPTER 7. CORRELATED ELECTRICAL AND OPTICAL STUDIES OF HYBRID ARGON GAS-WATER PLASMAS AND THEIR APPLICATION TO TOOTH WHITENING

OH rich plasma was generated in RF driven hybrid gas-water plasma. The chemical product in the plasma was applied on porcine tooth samples for tooth whitening without thermally or chemically damaging the surrounding soft tissue. The entire tooth stain was removed within 10 min without defects on the tooth enamel. The dominant chemical product, OH, was measured by Methylene Blue absorption, and proved by pH and electrical conductivity of the solution. Toxic chemical, H_2O_2 concentration was kept lower than 2 μM (< 30 μM, minimum level for soft tissue cell death) to prevent over-bleaching by hydrogen peroxide. The water temperature was kept less than 40 ^oC up to 1 hour plasma operation to prevent thermal damage on the surrounding soft tissue [1].

7.1. Introduction

Cold atmospheric plasma has been employed for dental applications [2, 3], sterilization [4, 5], cancer treatment [6, 7], tissue removal [8-10] and a means of changing chemical composition of feedstock gases [11]. The UV and ion fluxes generated by atmospheric plasma as well as OH, O, H, NO and O_3 reactive species drive these applications [12]. Tooth whitening by plasma treatment is one of such applications that require high rates of chemical reaction and low gas temperature since the gum tissue surrounding tooth is not as robust as the teeth at over 60 ^oC. For example, Lee el al. achieved tooth whitening primarily by employing the OH radicals from either pure water or a H_2O_2 containing solution, which was poured on the tooth surface, while simultaneously excited by helium gas plasma [2]. There are prior studies of the plasma

characteristics and its effect on the liquid conductivity and pH [13~16] as well as the antibacterial effect of this plasma [17].

We show herein that the hybrid gas-water plasma can achieve both high rate of chemistry on tooth surfaces and maintain low ambient temperature on nearby soft tissue. Hybrid gas-water plasmas can balance desired large fluxes of photons and radicals with low ambient temperatures. The surface of treated tissue was not directly affected by hybrid gas-water plasma (no direct contact of the plasma to the tooth samples) but affected by the chemical product. We present major chemical reaction pathways between water lying mm to cm away from the plasma jet injection location. These pathways analysis are based on both measurements of optical emission from the plasma jet and simultaneously measured chemical changes in the liquid environment. The chemical reaction rate was measured by monitoring the change of the concentrations of DI water electrical conductivity and pH. Subsequent reactions changed the concentration of OH and H_2O_2 reactive species in the water solution.

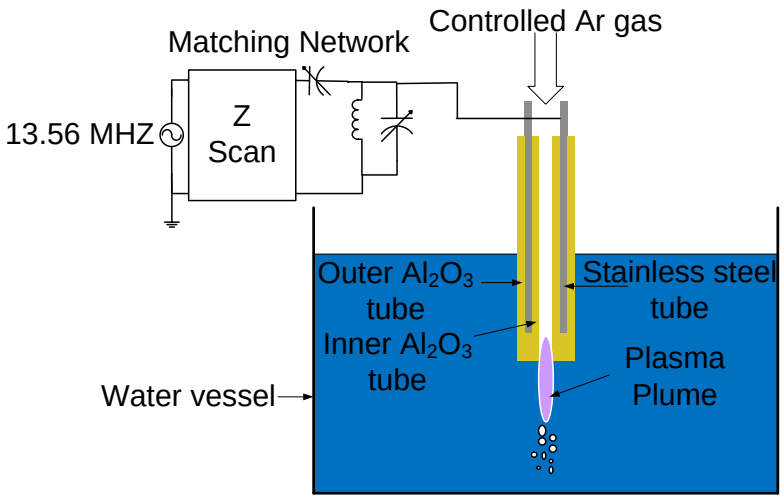

Figure 7-1 Schematic of the CSU designed experimental setup and electrode configuration for creating hybrid gas/liquid plasma

Finally we present data obtained from both optical and scanning electron microscope (SEM) measurements regarding optimized plasma plume length versus injected gas flow rate and applied power. These observations were used to determine the optimum placement of tooth/tissue samples to be irradiated. The range of optimal electrode locations was found to be 3 - 15 mm away from the water surface, which allows a tradeoff between ambient temperature at the surface of teeth and total flux of radicals impinging on the tooth surface.

7.2. Experimental Section

7.2.1. Plasma Electrode and Experiment Conditions

A 13.56 MHz power supply (Advanced Energy, CESAR RF power generator) was connected to the hybrid gas-water plasma system through a matching box. The coaxial plasma electrode consisted of an external insulating ceramic tube and the inner metallic electrode covered by ceramic tube as shown in Figure 7-1. The argon gas was injected through the stainless steel tube into DI water. The argon gas flow rate was controlled by a mass flow controller (Aera, TC FC-PA780c) and a digital flow controller (Advanced Energy, ROD-4). The initial electrical conductivity of DI water was less than 0.5 μS/cm. The electrode tip was soaked 1.5 cm deep from the surface of the DI water.

7.2.2. Plasma Characteristics Measurements

The optical spectroscopy was employed to monitor plasma characteristics. Plasma length in the water was measured with CCD camera (Princeton instruments, 7467-0028). We measured independent plume length of argon plasma jet based on total optical emission three times, at each plasma condition and averaged them. The spectrally resolved emission from the gas-liquid

hybrid plasma was measured with a spectrometer (Princeton instrument/ACTON, spectropro2750). The spectral data was employed to estimate OH and H_2O_2 concentration as a function of the treatment time. The plasma gas temperature in the water was estimated by comparing the OH spectrum with simulation result of LIFbase simulation program.

7.2.3. Measurement of DI Water Changes versus Plasma Jet Conditions

To analyze the effect of plasma on DI water, we measured the changes of the electrical conductivity, the pH, the temperature, concentration of the hydrogen peroxide (H_2O_2), and hydroxyl (OH) densities. Two or more 100 mL DI water samples were prepared for every single characteristic measurement of plasma treated DI water. The baseline conditions in DI water were measured for one of the samples without any plasma treatment and the other was measured after plasma treatment. The experiments were conducted four times and were averaged for each of the six plasma exposure times.

The conductivity, pH and temperature measurements were measured with three separate sensors: Thermo fisher scientific 013605MD, 8102BNUWP, 927006MD, respectively at 5, 10, 15, 20, 30, and 60 min of plasma treatment time. The H_2O_2 concentration in DI water was measured with a chemical assay kit (Cayman chemical company, Hydrogen peroxide assay kit, Catalog No. 706001). The absorbance of 666.02 nm light of methylene blue (MB) solution was recorded to measure the change in OH radical concentration after plasma treatment. We prepared five standard concentration of MB solution from 25.4 to 1.27 μM and made a calibration curve using UV absorption spectroscopy. The concentration of OH radicals was measured by comparing the absorbance of plasma treated DI water with an untreated reference solution absorbance. In our results and discussion analysis given below, we choose only the saturated

value of all measurements taken and the effect of DI water temperature on these values was compensated.

7.2.4. Teeth Sample Preparation and Analysis

Naturally stained porcine tooth were supplied from the Colorado State University Veterinary School. The tooth were placed 3 - 15 mm down from the electrode and exposed to the argon plasma in DI water. This allows for the plasma plume to spread out over the entire tooth surface and to provide a low ambient surface temperature. The surface color changes were characterized using CCD camera system. Plasma treated tooth surface topography was quantified by SEM (Scanning Electron Microscope) image, after 10 min exposure.

7.3. Result and Discussion

7.3.1. Plasma Conditions

The plasma length in DI water has a limited range of penetration and limited geometric stability. The Stability depends primarily on two experimental parameters: level of applied RF power and argon gas flow rate. The plume lengths of the plasma versus applied RF power and gas flow rate were given in Figure 7-2 and 7-3, respectively. No penetration of the jet into DI water occurred with less than 50 sccm argon gas flow rate. The plasma expanded into the water at 100 ~ 500 sccm. Therefore, the stable argon gas flow rate into DI water for repeatable experiment was between 50 and500 sccm. This limited flow rate window was chosen for all experimental conditions. Plasma length measurements were repeated three times to determine the average plasma plume length under each experimental condition. Fortunately under these

hydrodynamic conditions the plume length increases monotonically with the applied RF power to reach an optimal point indicated in Figure 7-2.

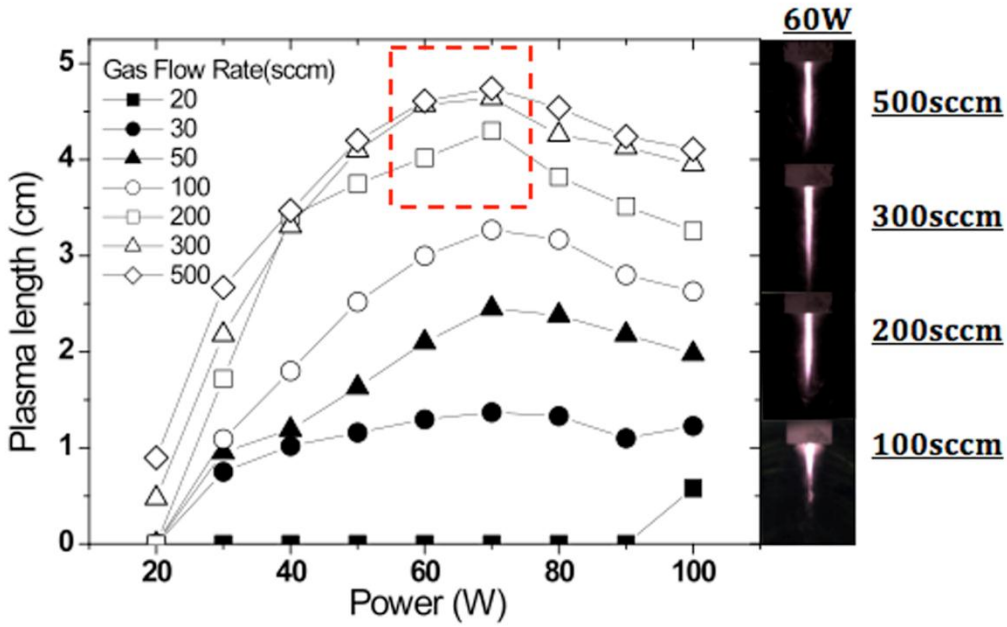

Figure 7-2 Plasma plume length injected into water ambient, as measured by total optical emission until plasma extinction as a function of the applied RF power. Each line corresponds to one gas flow rate. The red box is optimal points according to the plum length saturation. The side pictures are comparing the plume lengths measured at 60W. The gas flow is 100, 200, 300 and 500sccm from bottom to the top.

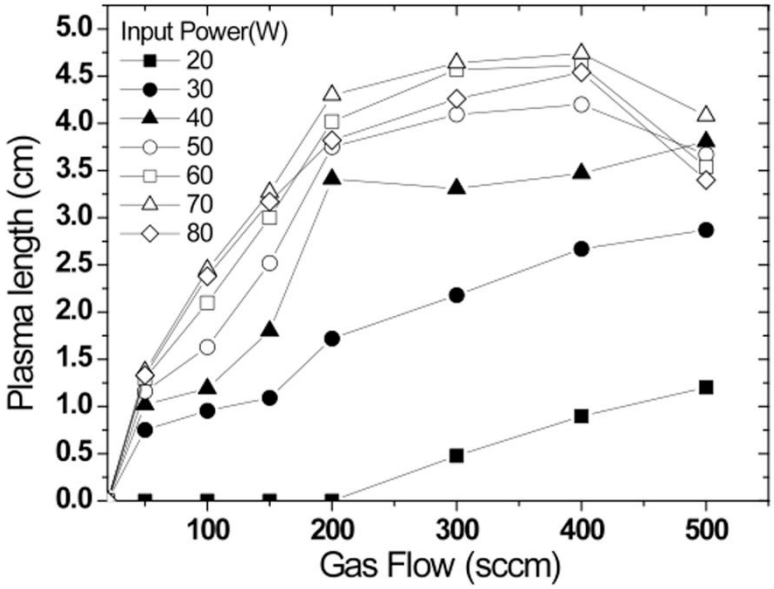

Figure 7-3 Plasma plume length injected into water, as measured by total optical emission until plasma extinction as a function of argon gas flow rate

7.3.2. Plasma Temperature Measurements

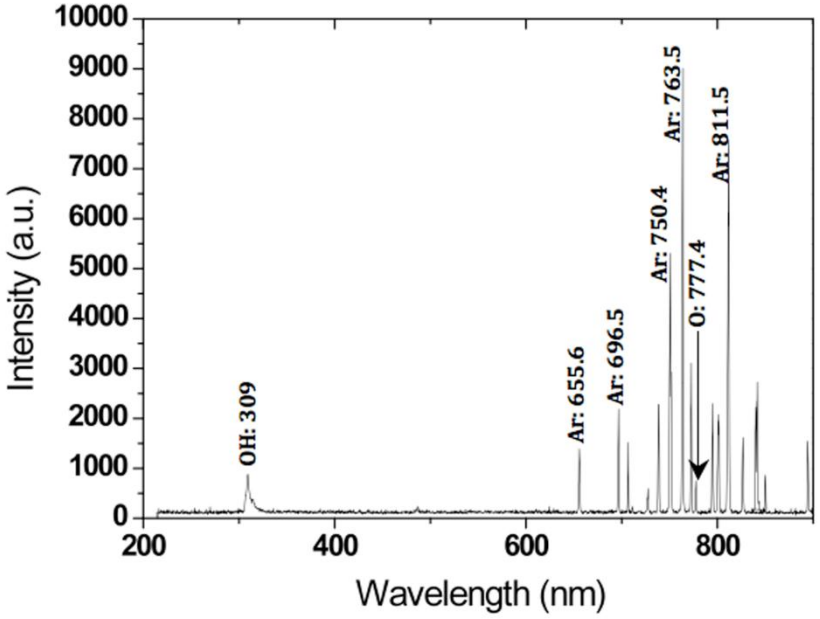

Figure 7-4 Typical optical emission spectrum emitted from a glow discharge in CSU designed hybrid gas/liquid plasma.

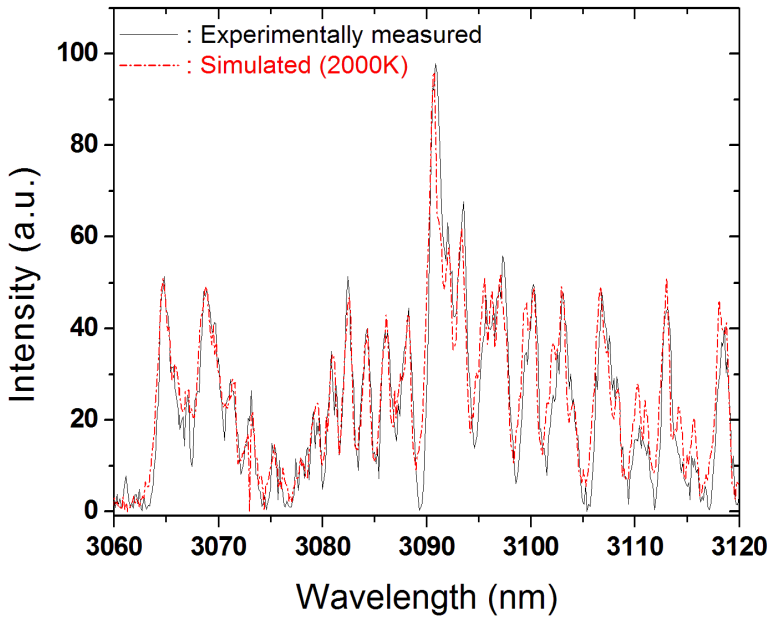

Figure 7-5 Comparison of both CSU measured OH band spectra and CSU simulated spectra (LIFbase) for the determination of the rotational temperature of hybrid plasma at 60W RF input power.

Figure 7-4 shows the Ar, H, O, and OH emission lines of the plasma between 200 to 850 nm [13]. The discharge emission did not show any characteristic lines of nitrogen atoms or molecules by contrast with strong O emission lines. The experimental OH spectrum was observed and compared with the simulated band of OH as shown in figure 7-5. The rotational temperature from OH spectrum was estimated by fitting the experimentally taken spectrum to simulated spectrum by LIFbase [18]. The temperature of the plasma gas can be approximated by rotational temperature at high pressure. The estimated rotational temperature was about 2000 K in the core of the plasma jet at 60 W applied RF power and 250 sccm gas flow rate. The gas temperature of argon gas plasma jet varies sharply with spatial position as it is rapidly cooled down by surrounding DI water. Water temperature at about 3 mm below the plasma termination position was 35 ± 5 °C, measured by an optical thermal probe.

7.3.3. Plasma Chemical Reaction Analysis in DI Water

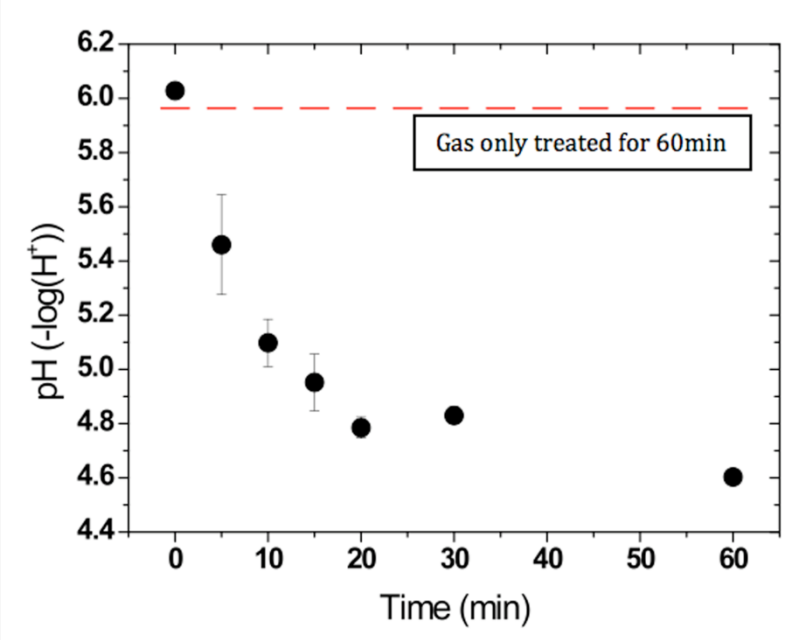

Figure 7-6 The pH change of plasma treated DI water versus plasma treatment time. The dashed line is for unexcited neutral argon gas bubbling.

We observed and correlated the changes of the DI water properties such as: pH, electrical conductivity, dissolved OH radical, and hydrogen peroxide densities. The test condition for these observations was kept constant as 250 sccm of argon and 60 Watts of input power since the pH of DI water changes with conditions of injection of argon plasma. Figure7-6 shows the pH of DI water with the argon plasma jet versus plasma treatment time. The pH value of DI water decreased with increasing time and finally saturated at 4.6. Figure 7-6 also shows pH of DI water with the argon gas flow only versus treatment time. The effect of argon gas flow only was measured for 60 minutes. When compared with gas only treated results, it is clear that the change in pH is not attributed to the argon gas but the plasma.

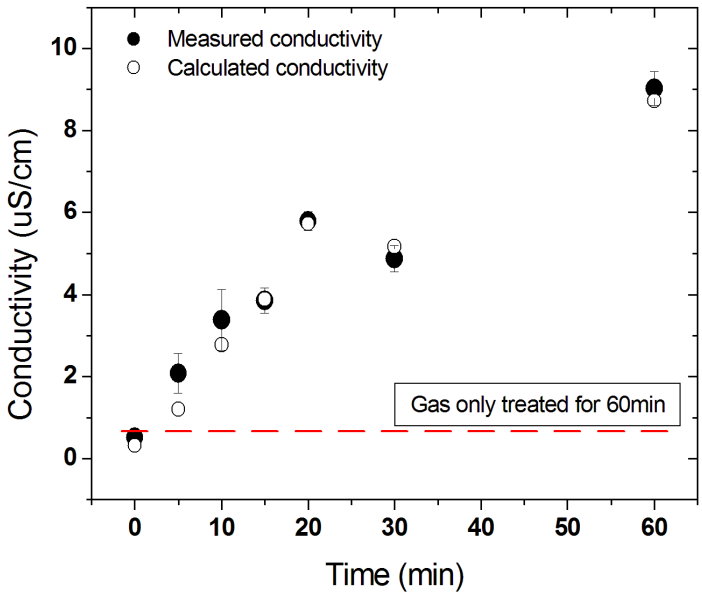

Figure 7-7 Comparison of measured conductivity (solid dot) and calculated conductivity (open dot) versus plasma treatment time.

As seen in Figure 7-7, electrical conductivity of DI water increased linearly with increasing the argon plasma exposure time. The conductivity of DI water exposed to argon gas without plasma was also included in Figure 7-7. The conductivity change of DI water has possible contributions from the ions originated from H_2O molecule, such as: H_3O^+, H^+, OH^-, and O_2^- [19]. Electrical conductivity can be obtained from the pH in Figure 7-6 by assuming that the positive ions are hydrogen ions, H^+, and that the negative ions are electrons.

Electrical conductivity can be calculated using:

$$\sigma = -\rho_e\mu_e + \rho_h\mu_h \qquad (1)$$

In Equation (1), the charge density and mobility are expressed by $\rho_e(\rho_h)$ and $\mu_e(\mu_h)$ respectively with notation for electron and hole. The charge density of hydrogen is equal to its

mol concentration × Avogadro's number × Coulomb number / 100 mL [Q/m^3]. The mol concentration of hydrogen ion was taken from the measured pH value. The conductivity change due to H^+ ions is calculated by multiplying the mobility of hydrogen ion 36.23×10^{-8} ($m^2 \cdot s^{-1} \cdot V^{-1}$) with the charge density [20]. The calculated conductivity from the hydrogen concentration is compared with measured conductivity in Figure 7-7. Note that every calculated conductivity well comply with those measured electrical conductivities. The small difference observed between measured and calculated conductivities is, we judge, due to other ions generated in the solution from secondary reactions. For example the negative OH ions could be generated from the gas phase OH molecules and subsequently dissolved into DI water as OH^-.

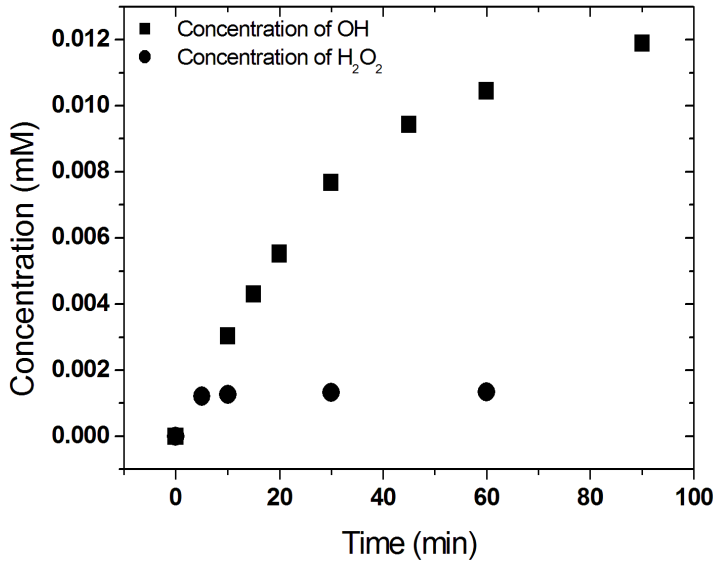

Figure 7-8 The concentrations of both OH (rectangle dots) and H_2O_2 (circled dots) versus plasma treatment time.

Next, we looked at the major chemical reaction pathways in the hybrid gas-water plasma and the justifications for these choices. The OH radical and H_2O_2 in DI water are the two major reactive chemical species created by the plasma jets. The measured concentrations of OH and

H_2O_2 molecules are shown in Figure 7-8. The OH concentration is measured to be of order of 10^{-5} mole and increases with time while the concentration of H_2O_2 remains at order of 10^{-6} mole. Therefore OH generation in the gas phase contributes to the liquid phase concentration change via the following reaction sequences:

$$e + H_2O \rightarrow H^+ + OH^- + e \quad (2)$$

$$e + H_2O \rightarrow O + H_2^+ + 2e \quad (3)$$

$$2OH \rightarrow H_2O_2 \quad (4)$$

$$OH^- + O \rightarrow HO_2 + e \quad (5)$$

The OH^- ions are generated primary with plenty H_2O source. H_2O_2 and HO_2 are generated consequent reaction of OH^- generation. Below there is a list of well-known rate constants based on references [9, 21].

HO_2 Generation reaction	Rate Coefficient ($cm^3 \cdot s^{-1}$)	
$e + H_2O_2 \rightarrow H + HO_2 + e$	3.1E-11	(6)
$OH^- + O \rightarrow HO_2 + e$	2.0E-10	(7)
H_2O_2 Generation		
$2\ HO_2 \rightarrow H_2O_2 + O_2$	1.15E-11	(8)
$2OH \rightarrow H_2O_2$	1.13E-12	(9)
OH Generation		
$e + HO_2 \rightarrow OH + O + e$	1.67E-09	(10)
$e + H_2O_2 \rightarrow 2OH + e$	2.36E-09	(11)

From the published rate coefficients, simple equilibrium kinetics indicates that the conversion of other species to the OH is higher than the opposite reactions by factors of 10 - 100. This corresponds to the saturated regions of our data and is consistent with Figure 7-8. For H_2O_2, the generation rate (Reaction 8 and 9) is much less than the conversion rate for H_2O_2 (Reaction 11). This species should remain at very low concentrations as supported by the result at Figure 7-8. The exchange between H_2O_2 and HO_2 is described in Equation (2 and 4). The rate coefficients of them are in the same order of magnitude. Therefore, we think that the OH molecules are the dominant species in the hybrid argon gas-liquid plasma producing either OH radicals in the gas phase or OH^- ions in DI solutions. The actual reactions in plasma-liquid interface are expected to be more complicated than those described in this chapter. Further research needs to be done for a more reliable reaction analysis.

7.3.4. Tooth Whitening Using RF Argon-DI Water Hybrid Plasmas

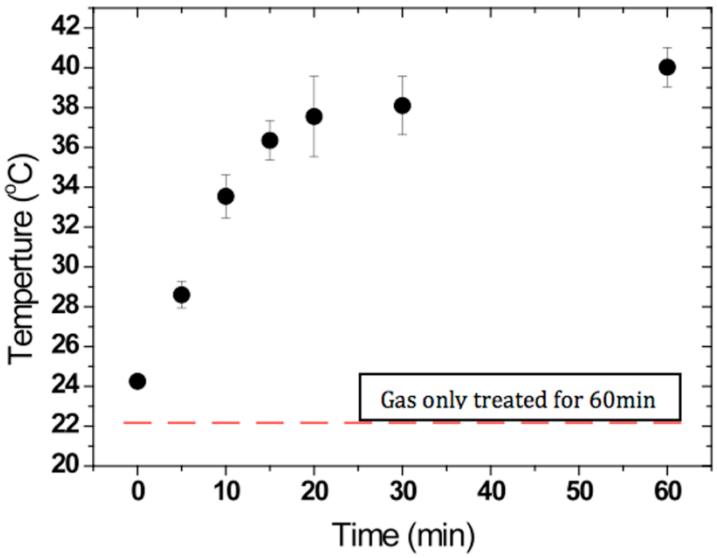

Figure 7-9 The temperature of DI water that was plasma treated by an injected plasma jet versus plasma treatment time. The temperature did not exceed 40 ^{o}C even after 60 minutes of plasma treatment.

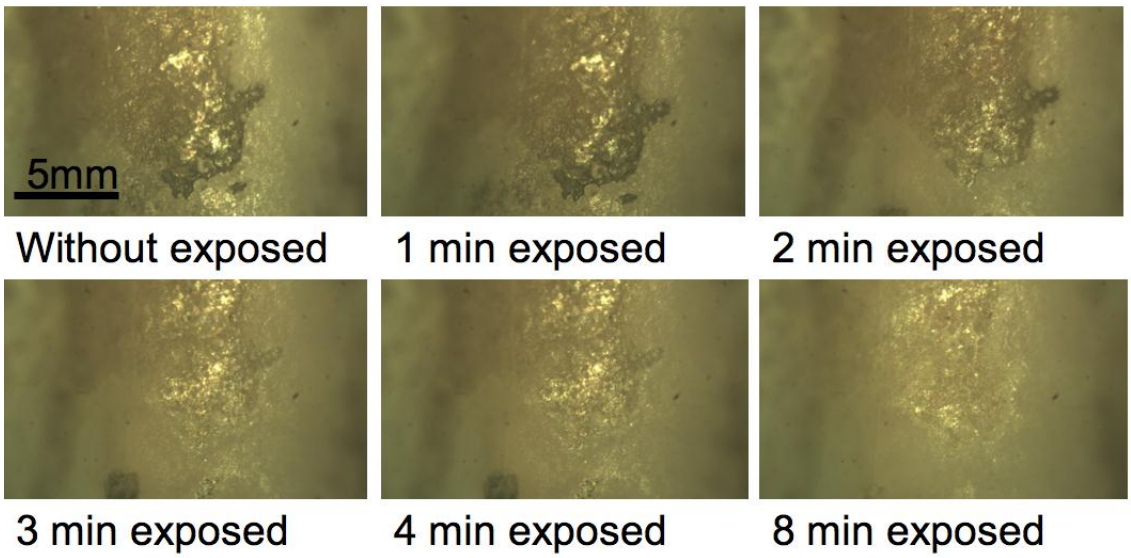

Figure 7-10 The surface color change of the tooth versus hybrid gas/liquid plasma treatment time.

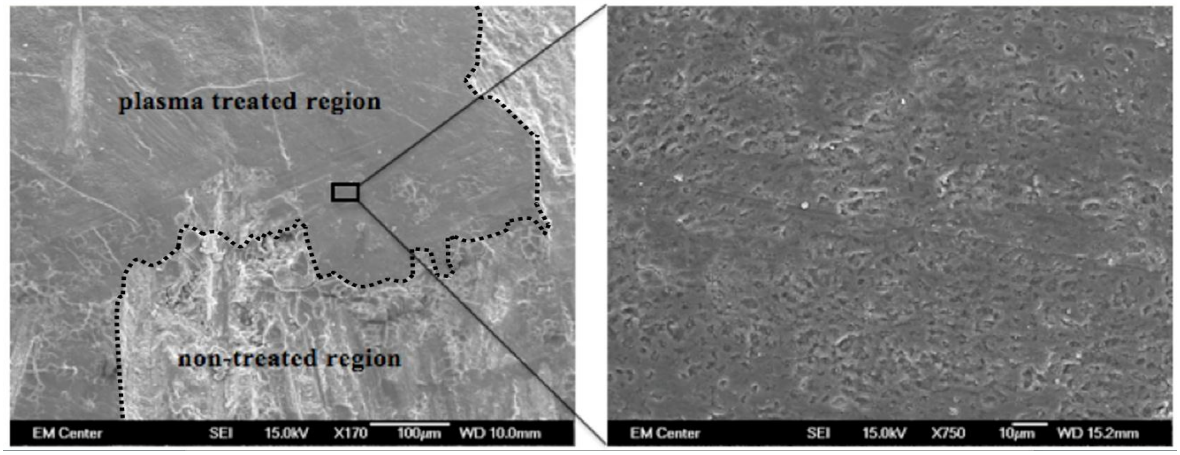

Figure 7-11 The SEM images of the tooth surface to examine any surface damage by hybrid plasma exposure after 10min treatment duration: low magnification (× 170) on the left and high magnification (× 750) on the treatment side

From our studies above, the hybrid plasma generates primarily OH radicals and H_2O_2 molecules. It is believed that OH species drives chemical pathways for tooth whitening.

Therefore the hybrid argon gas-liquid plasma can be a candidate for the tooth whitening application. We also measured very low concentration (< 0.03 wt%) of H_2O_2 in DI water. Maximum H_2O_2 concentration measured in DI water with plasma jet was about 1.5 μM, which is less than that the minimum H_2O_2 concentration to induce cell death to the surrounding soft tissue. as detailed in ref [22]. Thermal damage of soft tissue was ignorable when treated further than 3mm from the end of the plasma plum. Even though the rotational temperature of the plasma indicating the plasma gas temperature was about 2,000 K, the temperature below 3 mm of the plasma plume was near room temperature (< 40 ^{o}C) as shown in Figure 7-9. The temperature of the DI water with plasma generation was kept at such a low level, since the plasma bubble was cooled by water and the water was cooled by bubbling with plasma gas. Therefore, the undesired high temperature was prevented by water cooling while keep generating the reactive species with thermal plasma at the interface of plasma and water. The effect of the hybrid plasma on the irradiated tooth surface versus exposure time is shown in Figure 7-10. The entire tooth stain was removed within 10 min by hybrid plasma treatment. To confirm low damage levels on the enamel, the SEM picture in the Figure 7-11 indicated that the plasma removed stain material from the enamel, without inducing surface defects on the enamel [23].

7.4. Conclusion

The RF driven argon gas-DI water hybrid plasma was investigated by optical, electrical and chemical means versus duration of plasma treatment. We found that the measured electrical conductivity increased by plasma treatment and was correlated with the measured decreasing pH value. It supports that both the hydrogen peroxide and hydroxyl radicals are generated from the collision of energetic electrons with water molecules. The primary and secondary reaction

pathways underlying these observations agreed with the measurements of high OH densities and low H_2O_2 densities. Hence it was confirmed by both optical and SEM studies that tooth whitening by the hybrid gas-liquid plasma was driven primarily by OH radicals. We speculate that RF driven gas-liquid plasma configuration and choices of feedstock liquids and gases can be tailored for specific chemistries for other biomedical applications.

REFERENCES

[1] Myoung Soo Kim, Il Gyo Koo, Myeong Yeol Choi, Jae-Chul Jung, Fathala Eldali, Jae Koo Lee and George J. Collins, *Plasma Processes and Polymers*, **2012**, 9, 339.
[2] H.W. Lee, G. J. Kim, J. M. Kim, J. K. Park, J. K. Lee, G. C. Kim, *J. Endod.* **2009**, 35, 587.
[3] X. Lu, Y. Cao, P. Yang, Q. Xiong, Z. Xiong, Y. Xian, Y. Pan, *IEEE Trans. Plasma Sci.* **2009**, 37, 5.
[4] C. Jiang, M. T. Chen, C. Schaudinn, A. Gorur, P.T. Vernier, J. W. Costerton, D.E. Jaramillo, P. P. Sedghizadeh, M. A. Gundersen, *IEEE Trans. Plasma Sci.* **2009**, 37, 7.
[5] M. Laroussi, *Plasma Process. Polym.* **2005**, 5, 391.
[6] G. C. Kim, G. J. Kim, S. R. Park, S.M. Jeon, H. J. Seo, F. Iza, J. K. Lee, *J. Phys. D: Appl. Phys.* **2009**, 42, 032005.
[7] G. Fridman, A. Schereshevsky, M. M. Jost, A. D. Brooks, A. Fridman, A. Gutsol, V. Vasilets, G. Fridman, *Plasma Chem. Plasma Process* **2007**, 27, 163.
[8] K. R. Stalder, J. Woloszko, I. G. Brown, C. D. Smith, *Appl. Phys. Lett.* **2011**, 79, 27.
[9] D. V. Palanker, A. Vankov, P. Huie, *IEEE Trans. Bio. Eng.* **2009**, 55, 2.
[10] I. G. Koo, C. A. Moore, M. Y. Choi, G. J. Kim, P. Y. Kim, Y. S. Kim, Z. Yu, G.J. Collins, *Plasma. Process. Polym.* **2011**, 8, 1103.
[11] I. G. Koo, M. S. Lee, J. H. Shim, J. H. Ahn, W. M. Lee, *J. Mater. Chem.* **2005**, 15, 4125.
[12] A. Rahman, A. P. Yalin, V. Surla, O. Stan, K. Hoshimiya, Z. Yu, E. Littlefield, G. J. Collins, *Plasma Sources Sci. Technol.* **2004**, 13, 537.
[13] H. Aoki, K. Kitano, S. Hamaguchi, *Plasma Sources Sci. Technol.* **2008**, 17, 025006.
[14] T. Maehara, S. Honda, C. Inokuchi, M. Kuramoto, S. Mukasa, H. Toyota, S. Nomura, A. Kawashima, *Plasma Sources Sci. Technol.* **2011**, 29, 034016.
[15] M. Sato, T. Ohgiyama, J. S. Clements, *IEEE Trans. Indust. Appl.* **1996**, 32 106.
[16] T. Kaneko, K. Baba, T. Harada, R. Hatakeyama, *Plasma Process. Polym.* **2009**, 6, 713.
[17] F. Liu, P. Sun, N. Bai, Y. Tian, H. Zhou, S. Wei, Y. Zhou, J. Zhang, W. Zhu, K. Becker, J. Fang, *Plasma Process. Polym.* **2010**, 7, 231.
[18] J. Luque and D. R. Crosley, LIFBASE: *Database and Spectral Simulation Program version 2.0.64*, SRI international report MP 99-009, http://www.sri.com/cem/lifbase **1999**.
[19] I. G. Koo, W. M. Lee, *Jpn. J. Appl. Phys.* **2006**, 45, 10A.
[20] Peter Atkins, Julio De Paula, *Physical chemistry ATKINS*, 6th edition **1997**.
[21] D. X. Liu, P. Bruggeman, F. Iza, M. Z. Rong, M. G. Kong, *Plasma Sources Sci. Technol.* **2010**, 19, 025018.
[22] E. R. Whittemore, D. T. Loo, J. A. Watts, C. W. Cotman, *Neuroscirnce.* **1995**, 61, 4. .
[23] Y. C. Chiang, B. S. Lee, Y. L. Wang, Y. A. Cheng, Y. L. Chen, J. S. Shiau, D. M. Wang, C. P. Lin, *Lasers. Med. Sci.* **2008**, 23, 41.